

The Chemical Abundances of Stars in the Halo (CASH) Project.

III. A New Classification Scheme for Carbon-Enhanced Metal-poor Stars with S-process Element Enhancement^{1,2}

Julie K. Hollek³, Anna Frebel⁴, Vinicius M. Placco⁵, Amanda I. Karakas⁶, Matthew Shetrone^{3,7}, Christopher Sneden³, and Norbert Christlieb⁸

ABSTRACT

We present a detailed abundance analysis of 23 elements for a newly discovered carbon-enhanced metal-poor (CEMP) star, HE 0414–0343, from the Chemical Abundances of Stars in the Halo (CASH) Project. Its spectroscopic stellar parameters are $T_{eff} = 4863$ K, $\log g = 1.25$, $\xi = 2.20$ km s^{−1}, and $[Fe/H] = -2.24$. Radial velocity measurements covering seven years indicate HE 0414–0343 to be a binary. HE 0414–0343 has $[C/Fe] = 1.44$ and is strongly enhanced in neutron-capture elements but its abundances cannot be reproduced by a solar-type s-process pattern alone. Traditionally, it could be classified as “CEMP-r/s” star. Based on abundance comparisons with AGB star nucleosynthesis models, we suggest a new physically-motivated origin and classification scheme for CEMP-s stars

¹Based on observations gathered with the 6.5 meter Magellan Telescopes located at Las Campanas Observatory, Chile.

²Based on observations obtained with the Hobby-Eberly Telescope, which is a joint project of the University of Texas at Austin, the Pennsylvania State University, Stanford University, Ludwig-Maximilians-Universität München, and Georg-August-Universität Göttingen.

³Department of Astronomy, University of Texas, Austin, TX 78712-0259, USA; julie@astro.as.utexas.edu, chris@verdi.as.utexas.edu

⁴Department of Physics & Kavli Institute for Astrophysics and Space Research, Massachusetts Institute of Technology, Cambridge, MA 02139, USA; afrebel@mit.edu

⁵Department of Physics and JINA Center for the Evolution of the Elements, University of Notre Dame, Notre Dame, IN 46556, USA; vplacco@nd.edu

⁶Research School of Astronomy & Astrophysics, Australian National University, Canberra, Australia; amanda.karakas@anu.edu.au

⁷McDonald Observatory, University of Texas, Fort Davis, TX 79734, USA; shetrone@astro.as.utexas.edu

⁸Zentrum für Astronomie der Universität Heidelberg, Landessternwarte, Königstuhl 12, 69117 Heidelberg, Germany; N.Christlieb@lsw.uni-heidelberg.de

and the still poorly-understood CEMP-r/s. The new scheme describes a continuous transition between these two so-far distinctly treated subgroups: CEMP-sA, CEMP-sB, and CEMP-sC. Possible causes for a continuous transition include the number of thermal pulses the AGB companion underwent, the effect of different AGB star masses on their nucleosynthetic yields, and physics that is not well approximated in 1-D stellar models such as proton ingestion episodes and rotation. Based on a set of detailed AGB models, we suggest the abundance signature of HE 0414–0343 to have arisen from a $> 1.3 M_{\odot}$ mass AGB star and a late-time mass transfer, that transformed HE 0414–0343 into a CEMP-sC star. We also find the $[Y/Ba]$ ratio well parametrizes the classification and can thus be used to easily classify any future such stars.

Subject headings: Galaxy: halo – methods: spectroscopy – stars: abundances – stars: atmospheres – stars: Population II

1. Introduction

Metal-poor Population II (Pop II) stars were formed from gas that contained the nucleosynthetic signatures of the first chemical enrichment events in the Universe. Metal-poor stars preserve this information in their atmospheres, which we observe today. By understanding the chemical abundance patterns of metal-poor stars, we can probe the formation, initial mass function, and fates of the first stars. Altogether, metal-poor stars allow for a detailed reconstruction of the chemical enrichment sources and processes operating in the early universe and leading to the chemical evolution of the Milky Way: from core collapse supernovae of the earliest, massive stars, to the later contributions from the nucleosynthesis of lower-mass, evolved asymptotic giant branch (AGB) stars, and even the Type Ia supernovae.

Many metal-poor stars have prominent molecular carbon features in their spectra. The G-band feature near 4290 Å, the bandhead at 4313 Å, and the smaller band near 4323 Å are all CH molecular features. These all become strong to the point of saturation in the presence of large amounts of C. There are CN features across the spectrum, including a prominent feature near 8005 Å. The C₂ molecule is not often detected in metal-poor stars with $[C/Fe]$ ¹ ratios near the solar ratio; however, in stars with large C abundances, the bandheads near 4735, 5165, and 5635 often become strong enough from which to derive a $[C/Fe]$ ratio.

¹ $[A/B] = \log(N_A/N_B) - \log(N_A/N_B)_{\odot}$ for N atoms of elements A, B, e.g., $[Fe/H] = -2.0$ is 1/100 of solar Fe abundance.

Beers & Christlieb (2005) define a carbon-enhanced metal-poor (CEMP) star to be any metal-poor star with $[C/Fe] \geq 1$. Aoki et al. (2007) presented a revised CEMP definition of $[C/Fe] > 0.7$ for stars with $\log(L/L_{\odot}) \leq 2.3$ and $[C/Fe] > 3 - \log(L/L_{\odot})$ for stars with $\log(L/L_{\odot}) \geq 2.3$. The CN cycle greatly reduces the amount of C in the surface composition of a star over the course of the later stages of stellar evolution on the giant branch. Hence this definition allows for more evolved stars with lower C abundances to be considered in the study of C in the early universe.

CEMP stars can be subdivided into distinct chemical subgroups. Masseron et al. (2010) provides a comprehensive description and study of the different types of CEMP stars, which we will briefly outline here. CEMP-no stars are CEMP stars with normal neutron-capture abundances (indicated by $[Ba/Fe] \leq 0$) and otherwise typical abundances for metal-poor stars. The three most iron-poor stars discovered are CEMP-no stars (Christlieb et al. 2002; Frebel et al. 2005; Keller et al. 2014). The majority of CEMP stars have neutron-capture abundance enhancements. Among these, CS 22892–052 is the only one discovered to date with a pure rapid neutron-capture (r-) process abundance pattern (Snedden et al. 2000). The largest subgroup of CEMP stars is the CEMP-s stars (Masseron et al. 2010), which contain enhancements in the slow neutron-capture (s-) process elements. Finally, so-called CEMP-r/s stars are another CEMP group with neutron-capture overabundances but their abundance distributions do not display either a pure r- or pure s-process pattern (Bisterzo et al. 2009); both processes have been suspected to have contributed.

The designation of the CEMP-“r/s” stars has undergone much evolution. The term was introduced in Beers & Christlieb (2005) as “CEMP-r/s”. This term referred to stars with $[C/Fe] > 1.0$ and $0 < [Ba/Eu] < 0.5$. Jonsell et al. (2006) used the term “r+s” to refer to stars with $[Ba/Fe] > 1.0$ and $[Ba/Eu] > 0$ or $[Eu/Fe] > 1$ omitting the Ba criteria altogether, making no mention of the C abundance in the definition criteria, but noting that all of these r+s stars had significant C enhancement. Masseron et al. (2010) essentially combined the two previous definitions into the “CEMP-rs” designation for stars with $[C/Fe] > 0.9$ and $[Eu/Fe] > 1$ and $[Ba/Eu] < 0$, or $[C/Fe] > 0.9$ and $[Ba/Fe] > 2.1$. The $[Ba/Fe]$ criterion allowed for stars with no Eu abundance to also be classified. Bisterzo et al. (2012) even present additional subgroups. The Jonsell et al. (2006) designation was presented along with abundances for HE 0338–3945, an r+s star near the main sequence turn-off with $[Fe/H] = -2.42$. They presented nine possible scenarios for its formation, including the suggestion that these stars themselves formed from an r-enhanced gas cloud, although this scenario would be difficult to confirm observationally. Masseron et al. (2010) aimed to disentangle the contributions of AGB nucleosynthesis to the abundance patterns in CEMP stars by investigating processes that occur during the mass transfer from an AGB binary companion onto the observed CEMP star. No satisfactory solution to explain the abundance patterns of CEMP-r/s stars

has been presented so far (see also discussion in [Lugaro et al. 2012](#)).

The s-process occurs in the He-rich layers of evolved, low-mass AGB stars (e.g., [Gallino et al. 1998](#); [Karakas & Lattanzio 2014](#)), and operates on timescales of tens of thousands of years. Seed nuclei acquire neutrons one at a time and then β -decay as they climb the valley of stability on the chart of the nuclides. Bismuth is the termination point of the s-process. There are three stable peaks in the s-process pattern. They are centered around Sr, Ba, and Pb and these elements are particularly enhanced in s-process enriched metal-poor stars. This enrichment occurs when a low-mass star receives s-process enhanced material from a binary companion that underwent its AGB phase; observed today is the low-mass recipient of the AGB material. Many of these stars, including CEMP-s and CEMP-r/s stars, have been monitored for radial velocity variations and been shown to be binary stars ([Lucatello et al. 2005](#); [Starkenburg et al. 2014](#)). This principally confirms the mass-transfer scenario for these stars.

The Chemical Abundances of Stars in the Halo (CASH) project is a study that aims to understand the chemical abundance trends and frequencies of metal-poor halo stars as well as discover individual astrophysically interesting stars, based on the chemical abundances for ~ 500 stars from “snapshot” spectra observed using the Hobby-Eberly Telescope (HET) at McDonald Observatory. The spectra have moderate signal-to-noise ratios (~ 65) and resolution ($R \sim 15,000$). CEMP and s-process stars make up perhaps $\sim 20\%$ of the population of metal-poor stars. The first result from this project, [Roederer et al. \(2008\)](#), was the discovery of a CEMP-r/s giant star, HK II 17435-00532, with an enhanced Li abundance. The second paper, [Hollek et al. \(2011\)](#), presented the calibration of the automated stellar parameter and abundance pipeline, Cashcode, using both the HET snapshot spectra and higher-resolution, higher-S/N Magellan/MIKE spectra of 16 new extremely metal-poor stars to test it, along with the resultant comprehensive abundance analysis of the sample.

In this paper, we discuss HE 0414–0343, a CEMP star initially identified in the Bright Metal-Poor Star (BMPS) sample of [Frebel et al. \(2006\)](#) and included in the CASH project for further follow-up observations. This star was initially slated to be part of the sample from [Hollek et al. \(2011\)](#), but was singled out for special attention in order to obtain an even higher-resolution spectrum to better study this unique star. We discuss the observations and binary status for HE 0414–0343 in Section 2. We present our analysis methods used to determine the stellar parameters and abundances in Section 3 and the results in Section 4. In Section 5 we analyze neutron-capture abundance ratios. We compare the abundances of HE 0414–0343, as well as those of a literature sample to abundance yields of AGB star models in Section 6 and propose a new classification scheme based on our analysis of this star. In Section 7, we use the classification to gain insight into the origin of CEMP stars

with neutron-capture element enhancement associated with the s-process. We discuss the limitations of our analysis in Section 8, and summarize our results in Section 9.

2. Observations

HE 0414–0343 has an R.A. of 04 h 17 m 16.4 s and declination of $-03^{\circ} 36' 31''.0$. Thus, it is accessible from both the northern and southern hemispheres. Four separate spectra were obtained for HE 0414–0343 between 2004 and 2011. A medium-resolution spectrum was observed in September 2004 as part of the the Hamburg/ESO Bright Metal-Poor Star Sample [Frebel et al. \(2006\)](#). A high-resolution spectrum was obtained with MIKE instrument ([Bernstein et al. 2003](#)) at the Magellan-Clay Telescope at Las Campanas Observator in September 2006. Using a $0''.7$ slit with 2×2 on-chip binning yielded a resolution of $R \sim 35,000$ in the blue and 28,000 in the red. MIKE spectra have nearly full optical wavelength coverage from $\sim 3500 - 9000 \text{ \AA}$. In October 2008, HE 0414–0343 was observed as part of the CASH project with the fiber-fed High Resolution Spectrograph ([Tull 1998](#)) on the HET at McDonald Observatory. All CASH spectra were obtained with a $2''.0$ fiber yielding $R \sim 15,000$. The 2×5 on-chip CCD binning leads to 3.2 pixels per resolution element. Two CCDs were used to record the red and blue portions of the spectrum, spanning a wavelength range from 4200 - 7800 \AA .

The highest resolution spectrum, taken in March 2011, was used for the stellar parameter and chemical abundance determinations. This spectrum was also obtained using MIKE on the Magellan-Clay Telescope, but taken with a $0''.5$ slit. The spectral resolution is $R \sim 56,000$ at 4900 \AA and $\sim 37,000$ at 5900 \AA as measured from the ThAr frames. Table 1 lists the details of the observations for HE 0414–0343. The high resolution spectra for HE 0414–0343 were reduced using an echelle data reduction pipeline made for MIKE², initially described by [Kelson \(2003\)](#). We then utilized standard IRAF³ routines to co-add and continuum normalize the individual orders into a one-dimensional spectrum.

²Available at <http://obs.carnegiescience.edu/Code/python>.

³IRAF is distributed by the National Optical Astronomy Observatories, which is operated by the Association of Universities for Research in Astronomy, Inc., under cooperative agreement with the National Science Foundation

2.1. Binary Status

Heliocentric radial velocities of HE 0414–0343 were measured based on four independent observations taken over the course of seven years. The results are given in Table 1. We note that Robospect (Waters & Hollek 2013), an automated equivalent width measurement code that can calculate radial velocity shifts through cross-correlation was used for the $R \sim 35,000$ MIKE spectrum from 2006. A cross-correlation technique using the Mg b triplet was employed for the radial velocity determination of the HET snapshot spectrum Hollek et al. (2011). The radial velocity for the $R \sim 56,000$ MIKE spectrum was determined by measuring the average velocity offset for a set of 15 unblended lines in the red portion of the spectrum.

Typical radial velocity uncertainties for medium resolution spectra are $\sim 10 \text{ km s}^{-1}$, for snapshot spectra are $\sim 3 \text{ km s}^{-1}$, and for high-resolution spectra are $\sim 1\text{-}2 \text{ km s}^{-1}$. The radial velocity does vary significantly over these seven years, indicating that the star has an unseen binary companion. Establishing the binary status of HE 0414–0343 aids in understanding the nature and mechanism of the star’s carbon-enhancement and the overabundances in neutron-capture elements.

3. Spectral Analysis

3.1. Line Measurements

The equivalent widths were measured with a customized ESO/Midas program that automatically fits Gaussian profiles to each line. The user can adjust the fit to the continuum level by selecting line-free continuum regions, if necessary. The linelist for these stars is the

Table 1. Observations

R	UT Date	UT Time	t_{exp} s	S/N at 5180 Å	Telescope	v_{rad} km s^{-1}
2000	2004 September 20	18:13	120	50	SSO2.3m/DBS	–36
35,000	2006 September 27	9:30	450	65	Magellan-Clay/MIKE	–83.8
15,000	2008 October 10	9:19	239	85	Hobby-Eberly/HRS	4.0
56,000	2011 March 11	00:12	3000	120	Magellan-Clay/MIKE	11.3

same that was used in [Hollek et al. \(2011\)](#) for the MIKE spectra; however, we rejected all Fe I and Fe II lines with wavelengths shorter than 4450 Å due to severe blending with molecular C features. We also omitted any strongly blended lines for the other elements whose abundances were determined via equivalent width measurements. Table 2 lists the equivalent widths and corresponding line abundances that are partially obtained through spectrum synthesis (see also Section 4).

Table 2. Equivalent Widths and Abundances

Species	λ [Å]	χ [eV]	log gf	W mÅ	log $\epsilon(X)$
C ₂	5165	Synth	7.63
C ¹² /C ¹³	Synth	5 ^a
Mg I	4571.09	0.00	−5.69	98.7	5.94
Mg I	4702.99	4.33	−0.38	111.1	5.81
Mg I	5172.68	2.71	−0.45	240.5	5.75
Mg I	5528.40	4.34	−0.50	107.2	5.84
Mg I	5711.09	4.34	−1.72	24.7	5.76
Ca I	4455.89	1.90	−0.53	88.6	4.76
Ca I	5581.97	2.52	−0.56	34.0	4.51
Ca I	5588.76	2.52	0.21	80.2	4.49
Ca I	5590.12	2.52	−0.57	25.5	4.35
Ca I	5594.46	2.52	0.10	85.8	4.70
Ca I	5598.48	2.52	−0.09	68.6	4.60
Ca I	5601.28	2.53	−0.52	40.4	4.60
Ca I	5857.45	2.93	0.23	55.7	4.54
Ca I	6102.72	1.88	−0.79	63.5	4.46
Ca I	6122.22	1.89	−0.32	97.4	4.53
Ca I	6162.17	1.90	−0.09	102.1	4.39
Ca I	6439.07	2.52	0.47	102.0	4.55
Ca I	6449.81	2.52	−0.50	54.4	4.76
Ca I	6499.64	2.52	−0.82	35.2	4.76
Sc II	4415.54	0.59	−0.67	109.5	1.14
Sc II	5031.01	1.36	−0.40	71.9	1.02
Sc II	5031.01	1.36	−0.40	79.9	1.14
Sc II	5239.81	1.46	−0.77	68.0	1.43
Sc II	5526.78	1.77	0.02	70.0	1.01
Sc II	5641.00	1.50	−1.13	24.7	1.11
Sc II	5657.90	1.51	−0.60	51.2	1.04
Sc II	5658.36	1.50	−1.21	24.2	1.18
Sc II	5667.16	1.50	−1.31	28.5	1.37

Table 2—Continued

Species	λ [Å]	χ [eV]	log gf	W mÅ	log $\epsilon(X)$
Sc II	5684.21	1.51	−1.07	18.2	0.90
Ti I	3998.64	0.05	0.01	83.3	2.63
Ti I	4518.02	0.83	−0.27	42.6	3.06
Ti I	4533.24	0.85	0.53	67.0	2.66
Ti I	4534.78	0.84	0.34	58.0	2.70
Ti I	4535.56	0.83	0.12	55.8	2.87
Ti I	4548.76	0.83	−0.30	35.1	2.95
Ti I	4555.49	0.85	−0.43	35.2	3.11
Ti I	4656.47	0.00	−1.29	31.9	2.91
Ti I	4681.91	0.05	−1.01	63.8	3.20
Ti I	4840.87	0.90	−0.45	22.5	2.91
Ti I	4840.87	0.90	−0.45	25.1	2.97
Ti I	4981.73	0.84	0.56	85.7	2.88
Ti I	4981.73	0.84	0.56	90.8	2.98
Ti I	4991.07	0.84	0.44	87.1	3.02
Ti I	4991.07	0.84	0.44	96.5	3.20
Ti I	5007.20	0.82	0.17	85.6	3.25
Ti I	5007.20	0.82	0.17	88.2	3.29
Ti I	5016.16	0.85	−0.52	26.8	3.00
Ti I	5016.16	0.85	−0.52	28.5	3.04
Ti I	5020.02	0.84	−0.36	28.0	2.86
Ti I	5024.84	0.82	−0.55	26.8	3.00
Ti I	5024.84	0.82	−0.55	28.8	3.04
Ti I	5035.90	1.46	0.26	28.1	2.95
Ti I	5035.90	1.46	0.26	35.9	3.10
Ti I	5036.46	1.44	0.19	19.0	2.79
Ti I	5036.46	1.44	0.19	23.5	2.90
Ti I	5039.96	0.02	−1.13	55.6	3.12
Ti I	5039.96	0.02	−1.13	57.3	3.15
Ti I	5064.65	0.05	−0.94	71.1	3.20

Table 2—Continued

Species	λ [Å]	χ [eV]	log gf	W mÅ	log $\epsilon(X)$
Ti I	5210.39	0.05	−0.83	65.3	2.99
Ti II	4418.33	1.24	−1.97	84.1	3.12
Ti II	4441.73	1.18	−2.41	85.3	3.51
Ti II	4464.44	1.16	−1.81	97.1	3.10
Ti II	4470.85	1.17	−2.02	105.6	3.49
Ti II	4488.34	3.12	−0.82	21.2	3.03
Ti II	4529.48	1.57	−2.03	77.7	3.43
Ti II	4563.77	1.22	−0.96	138.8	3.17
Ti II	4583.40	1.16	−2.92	27.2	3.01
Ti II	4589.91	1.24	−1.79	90.0	3.01
Ti II	4636.32	1.16	−3.02	29.5	3.16
Ti II	4657.20	1.24	−2.24	58.6	2.94
Ti II	4708.66	1.24	−2.34	67.8	3.17
Ti II	4779.97	2.05	−1.37	62.7	3.07
Ti II	4798.53	1.08	−2.68	61.0	3.21
Ti II	4805.08	2.06	−1.10	84.7	3.17
Ti II	4805.08	2.06	−1.10	89.8	3.25
Ti II	4865.61	1.12	−2.81	29.8	2.89
Ti II	4865.61	1.12	−2.81	45.7	3.15
Ti II	4911.17	3.12	−0.34	43.8	2.97
Ti II	5185.90	1.89	−1.49	62.7	2.97
Ti II	5226.53	1.57	−1.26	124.2	3.41
Ti II	5336.78	1.58	−1.59	96.0	3.21
Ti II	5381.02	1.57	−1.92	64.3	3.03
Ti II	5418.76	1.58	−2.00	46.7	2.86
Cr I	4545.95	0.94	−1.37	31.4	3.27
Cr I	4600.75	1.00	−1.26	40.1	3.38
Cr I	4626.18	0.97	−1.32	32.6	3.27
Cr I	4646.15	1.03	−0.74	69.1	3.36
Cr I	4652.15	1.00	−1.03	48.3	3.28

Table 2—Continued

Species	λ [Å]	χ [eV]	log gf	W mÅ	log $\epsilon(X)$
Cr I	5206.04	0.94	0.02	113.1	3.24
Cr I	5247.56	0.96	−1.64	18.8	3.24
Cr I	5296.69	0.98	−1.36	27.5	3.18
Cr I	5348.31	1.00	−1.21	35.9	3.21
Cr I	5409.77	1.03	−0.67	68.9	3.22
Mn I	4754.04	2.28	−0.09	Synth	2.71
Mn I	4783.52	2.32	0.14	Synth	2.79
Fe I	4443.19	2.86	−1.04	71.1	5.32
Fe I	4466.55	2.83	−0.60	99.2	5.40
Fe I	4476.01	2.85	−0.82	88.6	5.42
Fe I	4484.22	3.60	−0.86	36.1	5.40
Fe I	4592.65	1.56	−2.46	79.8	5.37
Fe I	4632.91	1.61	−2.91	51.8	5.41
Fe I	4643.46	3.64	−1.15	21.1	5.41
Fe I	4678.84	3.60	−0.83	39.3	5.41
Fe I	4859.74	2.88	−0.76	92.7	5.41
Fe I	4859.74	2.88	−0.76	92.7	5.41
Fe I	4903.31	2.88	−0.93	60.4	5.01
Fe I	4903.31	2.88	−0.93	67.9	5.13
Fe I	4918.99	2.85	−0.34	99.3	5.08
Fe I	4918.99	2.85	−0.34	99.3	5.08
Fe I	4924.77	2.28	−2.11	39.9	5.17
Fe I	4924.77	2.28	−2.11	47.1	5.29
Fe I	4938.81	2.88	−1.08	58.5	5.13
Fe I	4938.81	2.88	−1.08	63.6	5.21
Fe I	4966.08	3.33	−0.87	41.0	5.15
Fe I	4966.08	3.33	−0.87	46.7	5.25
Fe I	4973.10	3.96	−0.95	17.6	5.45
Fe I	4994.13	0.92	−2.97	97.9	5.39
Fe I	4994.13	0.92	−2.97	98.8	5.42

Table 2—Continued

Species	λ [Å]	χ [eV]	log gf	W mÅ	log $\epsilon(X)$
Fe I	5006.11	2.83	−0.61	87.1	5.07
Fe I	5006.11	2.83	−0.61	88.7	5.11
Fe I	5014.94	3.94	−0.30	44.1	5.33
Fe I	5014.94	3.94	−0.30	44.9	5.34
Fe I	5041.07	0.96	−3.09	96.9	5.54
Fe I	5041.75	1.49	−2.20	98.4	5.30
Fe I	5049.82	2.28	−1.35	89.4	5.22
Fe I	5049.82	2.28	−1.35	93.6	5.30
Fe I	5051.63	0.92	−2.76	99.8	5.21
Fe I	5051.63	0.92	−2.76	99.8	5.21
Fe I	5068.76	2.94	−1.04	77.0	5.45
Fe I	5074.74	4.22	−0.20	35.2	5.39
Fe I	5079.22	2.20	−2.10	52.2	5.25
Fe I	5127.36	0.92	−3.25	83.4	5.39
Fe I	5141.73	2.42	−2.24	30.2	5.27
Fe I	5142.92	0.96	−3.08	99.2	5.55
Fe I	5192.34	3.00	−0.42	95.5	5.22
Fe I	5198.71	2.22	−2.09	50.8	5.24
Fe I	5202.33	2.18	−1.87	72.5	5.31
Fe I	5216.27	1.61	−2.08	85.9	5.07
Fe I	5217.39	3.21	−1.16	37.0	5.22
Fe I	5242.49	3.63	−0.97	20.4	5.17
Fe I	5263.30	3.27	−0.88	49.4	5.21
Fe I	5266.55	3.00	−0.39	87.5	5.04
Fe I	5281.79	3.04	−0.83	62.6	5.11
Fe I	5283.62	3.24	−0.52	77.3	5.27
Fe I	5302.30	3.28	−0.72	64.1	5.30
Fe I	5307.36	1.61	−2.91	46.1	5.26
Fe I	5324.17	3.21	−0.10	93.5	5.09
Fe I	5332.90	1.55	−2.78	56.4	5.22

Table 2—Continued

Species	λ [Å]	χ [eV]	log gf	W mÅ	log $\epsilon(X)$
Fe I	5339.93	3.27	−0.72	59.0	5.20
Fe I	5364.87	4.45	0.23	34.6	5.20
Fe I	5365.40	3.56	−1.02	19.7	5.11
Fe I	5367.46	4.42	0.44	39.2	5.04
Fe I	5369.96	4.37	0.54	53.0	5.11
Fe I	5389.47	4.42	−0.41	13.1	5.27
Fe I	5410.91	4.47	0.40	36.5	5.08
Fe I	5415.19	4.39	0.64	52.6	5.02
Fe I	5424.06	4.32	0.52	74.7	5.43
Fe I	5569.61	3.42	−0.54	66.3	5.29
Fe I	5572.84	3.40	−0.28	71.7	5.10
Fe I	5576.08	3.43	−1.00	44.6	5.43
Fe I	5586.75	3.37	−0.14	78.4	5.03
Fe I	5615.64	3.33	0.05	98.5	5.15
Fe I	5624.54	3.42	−0.76	51.4	5.28
Fe I	5658.81	3.40	−0.79	46.7	5.21
Fe I	5662.51	4.18	−0.57	15.4	5.23
Fe I	5701.54	2.56	−2.14	26.1	5.22
Fe I	6065.48	2.61	−1.41	71.0	5.26
Fe I	6136.61	2.45	−1.41	82.8	5.26
Fe I	6137.69	2.59	−1.35	74.8	5.24
Fe I	6191.55	2.43	−1.42	84.4	5.27
Fe I	6200.31	2.61	−2.44	20.2	5.41
Fe I	6213.42	2.22	−2.48	44.6	5.46
Fe I	6230.72	2.56	−1.28	84.0	5.28
Fe I	6252.55	2.40	−1.69	68.5	5.25
Fe I	6254.25	2.28	−2.44	47.3	5.53
Fe I	6322.68	2.59	−2.47	20.7	5.43
Fe I	6335.33	2.20	−2.18	48.1	5.19
Fe I	6393.60	2.43	−1.58	84.4	5.42

Table 2—Continued

Species	λ [Å]	χ [eV]	log gf	W mÅ	log $\epsilon(X)$
Fe I	6400.00	3.60	−0.29	65.5	5.20
Fe I	6411.64	3.65	−0.59	47.9	5.28
Fe I	6421.35	2.28	−2.01	64.1	5.35
Fe I	6430.84	2.18	−1.95	87.8	5.54
Fe I	6592.91	2.73	−1.47	52.2	5.15
Fe II	4489.18	2.83	−2.97	47.7	5.28
Fe II	4508.28	2.86	−2.58	68.5	5.26
Fe II	4515.34	2.84	−2.60	75.8	5.38
Fe II	4520.22	2.81	−2.60	64.1	5.15
Fe II	4583.84	2.81	−1.93	95.3	5.05
Fe II	4620.52	2.83	−3.21	36.3	5.32
Fe II	4731.43	2.89	−3.36	29.4	5.40
Fe II	4993.35	2.81	−3.67	13.6	5.19
Fe II	4993.35	2.81	−3.67	17.9	5.33
Fe II	5197.58	3.23	−2.22	62.7	5.18
Fe II	5234.63	3.22	−2.18	61.9	5.11
Fe II	5276.00	3.20	−2.01	70.7	5.06
Fe II	5284.08	2.89	−3.19	30.2	5.21
Fe II	5325.55	3.22	−3.16	16.1	5.22
Fe II	5534.83	3.25	−2.93	27.1	5.29
Fe II	6247.54	3.89	−2.51	20.5	5.42
Fe II	6432.68	2.89	−3.71	22.2	5.51
Fe II	6456.38	3.90	−2.08	37.2	5.34
Ni I	4605.00	3.48	−0.29	22.5	4.10
Ni I	4648.65	3.42	−0.16	23.7	3.92
Ni I	4855.41	3.54	0.00	20.7	3.81
Ni I	4904.41	3.54	−0.17	12.2	3.71
Ni I	4904.41	3.54	−0.17	20.3	3.97
Ni I	4980.16	3.61	−0.11	22.6	4.05
Ni I	4980.16	3.61	−0.11	25.0	4.10

Table 2—Continued

Species	λ [Å]	χ [eV]	log gf	W mÅ	log $\epsilon(X)$
Ni I	5035.37	3.63	0.29	22.7	3.67
Ni I	5035.37	3.63	0.29	34.7	3.92
Ni I	5080.52	3.65	0.13	34.2	4.09
Ni I	5081.11	3.85	0.30	15.6	3.71
Ni I	5084.08	3.68	0.03	16.1	3.80
Ni I	5754.67	1.94	−2.33	25.2	4.37
Ni I	6643.64	1.68	−2.30	33.4	4.14
Ni I	6767.77	1.83	−2.17	34.6	4.20
Zn I	4810.52	4.08	−0.13	Synth	2.38
Sr II	3464.45	3.04	0.49	Synth	1.11
Y II	4883.68	1.08	0.07	Synth	0.13
Y II	5087.42	1.08	−0.17	Synth	0.21
Zr II	4208.99	0.71	−0.46	Synth	0.71
Zr II	4613.95	0.97	−1.54	Synth	0.87
Zr II	5112.28	1.66	−0.59	Synth	0.99
Ba II	5853.69	0.60	−0.91	Synth	1.80
Ba II	6141.73	0.70	−0.08	Synth	1.77
Ba II	6496.91	0.60	−0.38	Synth	1.87
La II	4740.28	0.13	−0.94	Synth	0.45
La II	4748.73	0.93	−0.54	Synth	0.42
La II	4824.05	0.65	−1.19	Synth	0.64
La II	6262.29	0.40	−1.24	Synth	0.40
La II	6390.48	0.32	−1.45	Synth	0.41
Ce II	4739.51	1.25	−0.53	Synth	0.67
Ce II	4739.52	0.53	−1.02	Synth	0.69
Ce II	4747.26	0.90	−1.79	Synth	0.89
Ce II	4882.46	1.53	0.19	Synth	0.70
Pr II	4744.91	0.20	−1.14	Synth	−0.17
Nd II	5310.04	1.14	−0.98	Synth	0.83
Nd II	5311.45	0.98	−0.42	Synth	0.87

3.2. Stellar Parameters

Stellar parameters and elemental abundances derived from equivalent widths were determined using the spectroscopic stellar parameter and abundance analysis pipeline, Cashcode. Cashcode is written around the LTE line analysis and spectral synthesis code, MOOG (Snedden 1973). It employs the latest version of MOOG (Sobeck et al. 2011), which properly treats Rayleigh scattering, an opacity source that is important in cool giants like HE 0414–0343. We used a Kurucz stellar atmosphere with α -enhancement (Castelli & Kurucz 2004). Cashcode iterates to determine the set of stellar parameters which yield a flat relation between the line abundances and excitation potential, a flat relation between the line abundances and reduced equivalent width values, and to ensure that the Fe I and Fe II abundance values are consistent with each other. See Hollek et al. (2011) for a detailed description of the stellar parameter determination technique.

We determined the spectroscopic stellar parameters using equivalent width measurements of 88 Fe I and 18 Fe II lines resulting in $T_{eff} = 4660$ K, $\log g = 0.75$, $\xi = 2.05$ km s^{−1} and $[\text{Fe}/\text{H}] = -2.38$. The resonance lines of Fe I were excluded in this analysis, as they are strong enough that they are often near the flat portion of the curve of growth. It should be noted that photometric temperatures are difficult to determine in CEMP stars because the molecular carbon bands interfere with the different photometric band passes in varying degree, thus making the photometric temperatures unreliable. Spectroscopic temperatures are often several hundred degrees cooler than photometrically-derived values. We thus adjusted the stellar parameters to make them more closely reflect photometric stellar parameters, following the procedure outlined in Frebel et al. (2013). These values are $T_{eff} = 4863$ K, $\log g = 1.25$, $\xi = 2.20$ km s^{−1} and $[\text{Fe}/\text{H}] = -2.24$, which we adopt. In Figure 1, we show the derived effective temperature and surface gravity for HE 0414–0343 plotted together with 12 Gyr Yale-Yonsei isochrones (Kim et al. 2002; Green et al. 1984) for $[\text{Fe}/\text{H}] = -2.0$, -2.5 , and -3.0 as well as a Cassisi et al. (2004) horizontal branch track.

We determined the random uncertainty in the surface gravity by allowing the Fe I and Fe II values to vary until they no longer agree within the uncertainty of Fe I, which is 0.12 dex. Since HE 0414–0343 is on the giant branch, uncertainties in effective temperature at the ~ 150 K level lead to changes in the surface gravity of ~ 0.5 dex. We conservatively adopt this as our σ_{logg} uncertainty. We determined the standard error of the mean Fe I abundance to be ~ 0.01 dex; however, we adopt the scatter of the individual Fe line abundances as our final $[\text{Fe}/\text{H}]$ uncertainty (~ 0.12 dex) as the standard error is quite low and does not account for uncertainties in the continuum placement for each measured line, which is especially difficult in a CEMP star.

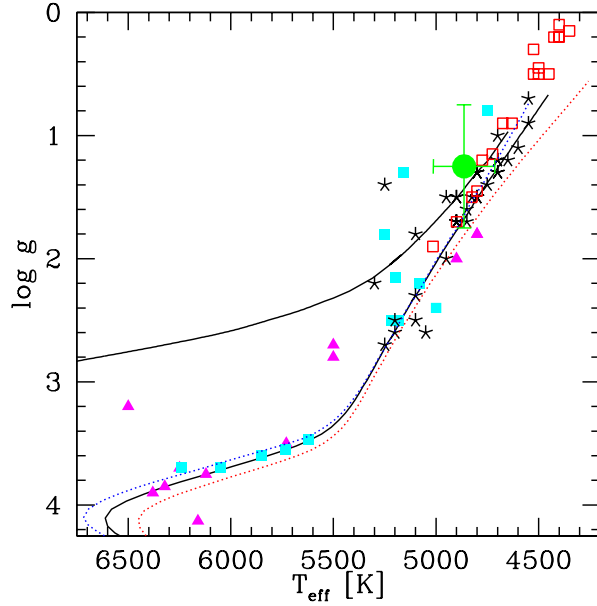


Fig. 1.— HR diagram with HE 0414–0343 (green filled circle) plotted against the Hollek et al. (2011) sample (red open squares), the Cayrel et al. (2004) sample (black stars), and selected s-process (cyan filled squares) and r/s-process (magenta filled triangles) enhanced stars as collated by Placco et al. (2013). Overplotted are the Yale-Yonsei isochrones (Kim et al. 2002; Green et al. 1984) for 12 Gyr, at $[\text{Fe}/\text{H}] = -2.0$ (red line), -2.5 (black line), and -3.0 (blue line), as well as a horizontal-branch mass track from Cassisi et al. (2004).

4. Chemical Abundance Analysis

The equivalent widths were used to determine abundances for seven different elements as well as the stellar parameters. Spectral syntheses of blended lines or lines with hyperfine structure were performed manually, given the often severe blending due to the C-enhancement in the star. Table 3 lists the abundances. Solar abundances of Asplund et al. (2009) were used to calculate $[\text{X}/\text{H}]$ and $[\text{X}/\text{Fe}]$ values. Further details on the elemental abundances are given below.

Table 4 lists our abundance uncertainties. We determined the systematic uncertainties by varying the stellar parameters of effective temperature, $\log g$, and microturbulence in the model atmosphere used in proportion to the uncertainty of each parameter. The abundances were then recalculated with the new model atmospheres either by averaging the individual line abundances determined from equivalent width or by re-fitting a synthetic spectrum. The random uncertainty for each abundance determined via equivalent width was taken as

the standard deviation of the individual line abundances. We use the standard deviation rather than the standard error because it better reflects that our abundances are hampered by the presence of molecular C. For the abundances derived via spectral synthesis, we used the original model atmosphere and varied the abundance of the synthetic spectrum until the fit no longer matched the input spectrum. In the cases where there were fewer than 5 measurements, we used a special treatment for low number statistics. We adopt a minimum standard error of 0.12 dex and use this for all measurements with formally calculated smaller values. For elements with just one available line, we conservatively assigned an 0.3 dex uncertainty. The systematic uncertainties based on the stellar parameters and the random uncertainties were then added in quadrature to determine the total error value.

4.1. Carbon, Nitrogen, and Oxygen

There are several strong molecular C features in the spectrum of HE 0414–0343, as seen in Figure 2. In fact, the CH features at 4313 Å (the G-band) and another smaller feature at 4323 Å are essentially saturated. The bandhead of the λ 5165 C₂ feature is not saturated and thus was used to determine the C abundance via spectral synthesis. We find $[C/Fe] = 1.44$. However, attempting to measure the G-band and λ 4323 features yield $[C/Fe] = 1.39$ and 1.44, respectively. These are consistent with the adopted abundance ratio. The CH and CN linelists (B. Plez 2006, private communication) are described in Frebel et al. (2007), with further description of the CN linelist available in Hill et al. (2002). The linelist used to determine the adopted C abundance from the C₂ feature is based on the Kurucz (1998) linelist. In Figure 2 we show the best fit abundances derived from the λ 5165 C₂ feature, as well as those from the CH G-band and the 4323 Å features. The large $[C/Fe]$ ratio of HE 0414–0343 categorizes it as a CEMP star using both the Beers & Christlieb (2005) and Aoki et al. (2007) definitions, as demonstrated in both panels of Figure 3.

In order to obtain an accurate C abundance, we determined the $^{12}\text{C}/^{13}\text{C}$ ratio from the ^{12}CN and ^{13}CN features near λ 8005 seen in Figure 2. For analysis of the CN features, the N abundance was used as a free parameter. HE 0414–0343 is an evolved red giant star so the $^{12}\text{C}/^{13}\text{C}$ ratio should be low due to the mixing of CN-cycled material into its atmosphere with much of the ^{12}C converted to ^{13}C . Indeed, we find $^{12}\text{C}/^{13}\text{C} = 5$, which was adopted uniformly throughout subsequent spectrum syntheses that required the C abundance.

We also measured the CN bandhead near 4215 Å and the CH feature near 4237 Å, to confirm our $^{12}\text{C}/^{13}\text{C}$ result. From both features, we derive a ratio of ~ 5 –10. Using a new C₂ linelist from Brooke et al. (2013) and Ram et al. (2013), we determined a $[C/Fe]$ ratio of ~ 1.4 using several features across the spectrum, including one near the λ 4736 C₂ bandhead,

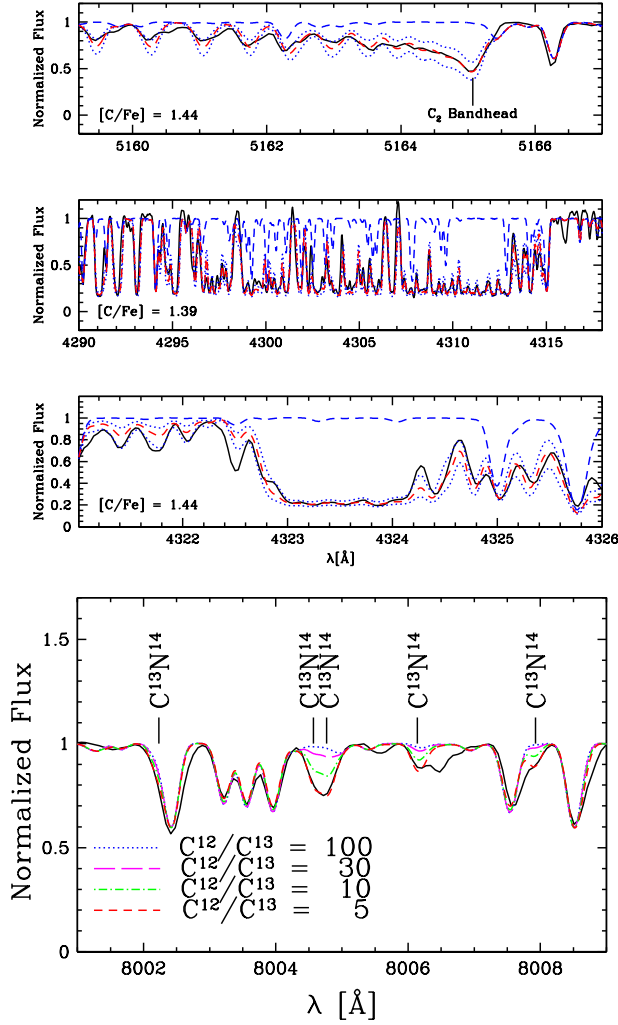


Fig. 2.— Top: $\lambda 5165$ C_2 feature (solid black line), along with the best fit synthetic abundance (red dashed line) with $[\text{C}/\text{Fe}] = 1.44$, C abundances changed a factor of two above and below the best fit abundance (blue dotted line), and a synthetic spectrum for which no C is present (blue dashed line). Two middle panels: CH G-band and the 4323 \AA CH feature, yielding $[\text{C}/\text{Fe}] = 1.39$ and 1.44 , respectively, confirming the $[\text{C}/\text{Fe}] = 1.44$ abundance ratio adopted from the $\lambda 5165$ C_2 feature. Bottom: $\lambda 8005$ CN feature in HE 0414–0343 (solid black line) from which the $^{12}\text{C}/^{13}\text{C}$ ratio was derived, along with synthetic spectra of varying $^{12}\text{C}/^{13}\text{C}$ ratios where $^{12}\text{C}/^{13}\text{C} = 5$ (red dashed line), $^{12}\text{C}/^{13}\text{C} = 10$ (green dotted-dashed line), $^{12}\text{C}/^{13}\text{C} = 30$ (magenta long dashed line), and $^{12}\text{C}/^{13}\text{C} = 100$ (blue dotted line).

which confirms our C abundance.

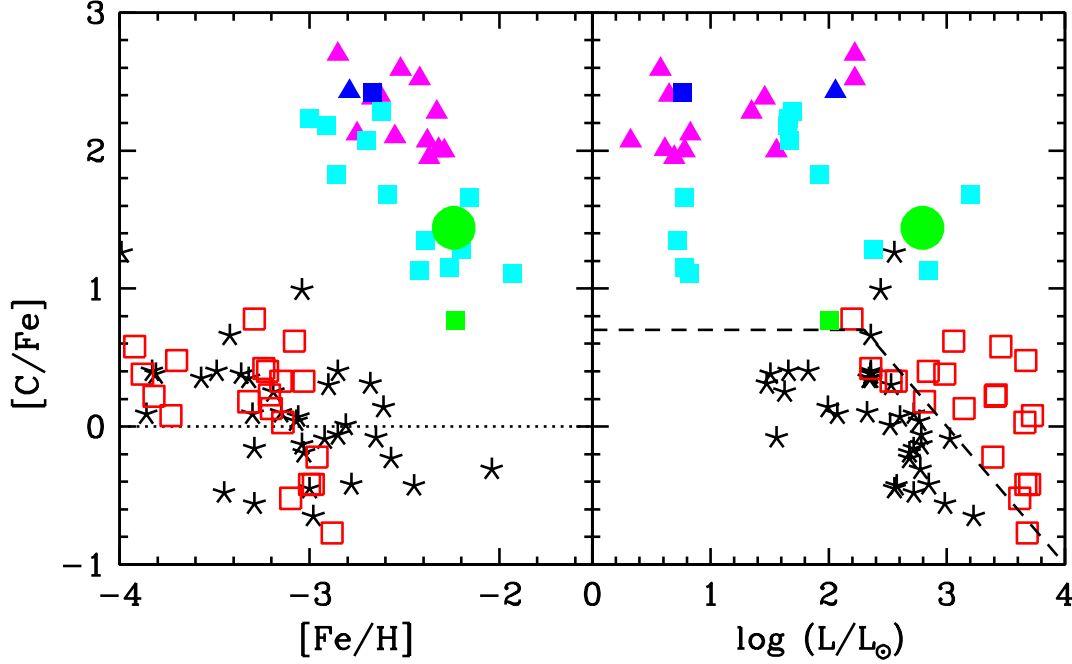


Fig. 3.— Left: $[C/Fe]$ plotted against $[Fe/H]$, where the green filled circle represents HE 0414–0343, the red open squares are stars from Hollek et al. (2011), and the black stars represent Cayrel et al. (2004) data. The magenta triangles correspond to CEMP-r/s stars, the cyan squares represent CEMP-s stars, and the blue stars are those from Placco et al. (2013) with the triangle and the square representing the CEMP-r/s and CEMP-s stars respectively. Right: $[C/Fe]$ abundance against luminosity, with the black dashed line representing the CEMP cut-off as prescribed by Aoki et al. (2007).

The N abundance can be determined from diatomic CN and monatomic NH. While it is desirable to determine the N abundance independently, we were unable to derive an abundance from the $\lambda 3360$ NH molecular feature given its blue wavelength and the corresponding low S/N ratio. The N abundance in the CN molecule was treated as a free parameter and also yielded no useful N abundance given the overwhelming amount of carbon in these features.

The O abundance is difficult to measure in metal-poor stars due to the paucity of lines. The O features principally available in HE 0414–0343 are the [O I] forbidden line at 6300 \AA and the O triplet. The forbidden line is weak and is difficult to discern from molecular C in our spectrum. We measured the equivalent widths of the three lines of the O triplet near 7772 \AA in this star; however, no reliable abundance could be determined since these lines all give varying abundances.

4.2. Light elements: $Z \leq 30$

Figure 4 shows the abundances of HE 0414–0343 together with those of the Cayrel et al. (2004) and Hollek et al. (2011) studies. We now discuss individual elements and abundance results.

We do not detect the $\lambda 6707$ Li I doublet in our spectra. The Li abundance in evolved stars is expected to be low. During the first and second dredge-ups, the Li surface abundance is greatly diluted, as Li-poor material is brought to the surface. Our non-detection of Li in HE 0414–0343 is consistent with this standard scenario. We derived a 3σ upper limit of $A(\text{Li}) = \log \epsilon(\text{Li})^4 = 1.08$. We also do not derive an abundance from the Na D features near 5890 \AA , as they are heavily blended with interstellar Na. We did not calculate the Al or Si abundance because the corresponding lines are located exclusively in the blue portion of the spectrum between 3900 and 4105 \AA and are heavily blended with CH lines. Additionally, the $\lambda 4102$ Si line is located in the pseudocontinuum of the nearby $\text{H}\delta$ line. The Co I lines available are $\lambda 3502$, $\lambda 3995$, and $\lambda 4020$, all of which are well within a C-rich region and give spurious results. Thus, we do not present an abundance for Co.

With the exceptions of C, Mn, and Zn, all $Z \leq 30$ elemental abundances were derived from equivalent width measurements. The abundances derived for the light elements are all consistent with what is expected from the typical metal-poor halo star. We find enhancement in the α -elements of Mg, Ca, and Ti, with $[\alpha/\text{Fe}] = 0.49$. For the purposes of synthesis, plotting, and determining the $[\alpha/\text{Fe}]$ ratio, we adopt the Ti II abundance as the Ti abundance, as Ti I and Ti II differ by 0.16 dex. Using only those Ti I lines with newly-determined gf values from Lawler et al. (2013) and Ti II lines from Wood et al. (2013), the abundance discrepancy shrinks to 0.12 dex. This agreement supports our Fe-derived $\log g$ value. We find depletion in the Fe-peak elements of Cr, Mn, and Ni and enhancement of Sc and Zn, all of which is consistent with the Hollek et al. (2011) and Cayrel et al. (2004) studies. For Mn and Zn, we derived abundances from synthetic spectrum computations. We obtain $[\text{Mn}/\text{Fe}] = -0.48$ from the $\lambda 4754$ line and $[\text{Zn}/\text{Fe}] = 0.06$ from the $\lambda 4810$ line.

4.3. Neutron-Capture Elements

All abundances for neutron-capture elements discussed in this section were determined with spectrum synthesis due to blending with other species or hyperfine structure. We discuss each element in detail below.

⁴ $\log \epsilon(X) = \log(N_X/N_H) + 12$

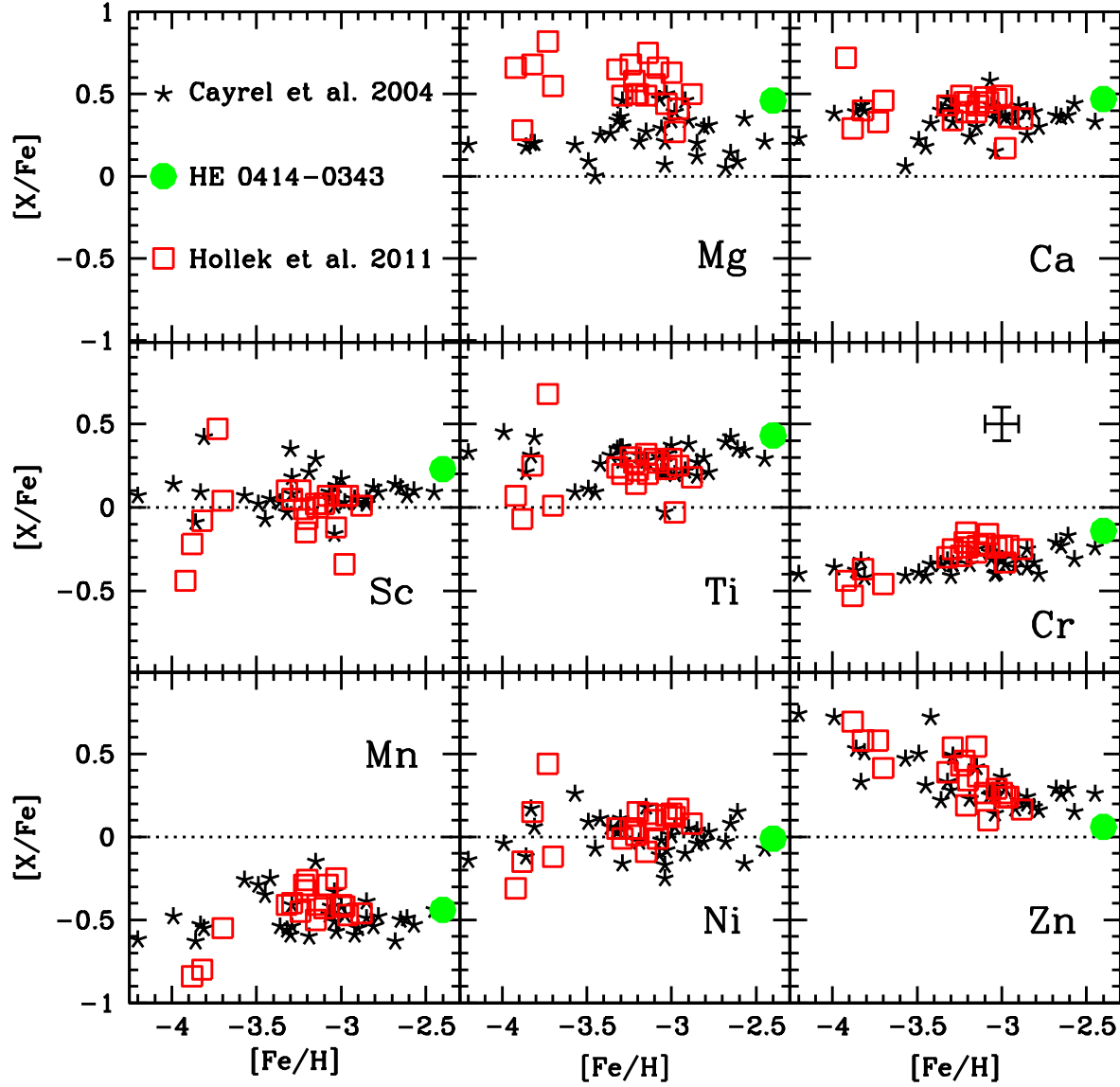


Fig. 4.— $[X/Fe]$ abundance ratios plotted against $[Fe/H]$ for elements up to Zn measured in the spectrum of HE 0414-0343 (green filled circle) compared with the Cayrel et al. (2004) (black stars) and the Hollek et al. (2011) abundances (red open squares). The black dotted line represents the solar abundance ratio. The Zn and Mn abundances were determined via spectral synthesis while the rest were determined from equivalent width measurements. In the Cr panel, we include a typical error bar.

The Sr abundance was obtained from the $\lambda 3464$ Sr II line, yielding $[\text{Sr}/\text{Fe}] = 0.48$, though it is in a region of low S/N, this line has the cleanest spectral region. The typical Sr lines used in abundance analyses of metal-poor stars, $\lambda 4215$ and $\lambda 4077$, both suffer from extensive blending with molecular C features. In fact, the $\lambda 4215$ line is blended with so much CN that we were able to use that feature to measure the $^{12}\text{C}/^{13}\text{C}$ ratio, but could not determine a Sr abundance.

The Y abundance was determined from the $\lambda 4883$ line, which is blended with CN accounted for in the linelist, and the unblended $\lambda 5087$ line. We derived $[\text{Y}/\text{Fe}] = 0.16$ and 0.24 from these lines, respectively and adopted the average abundance, $[\text{Y}/\text{Fe}] = 0.20$.

The Zr abundance is based on the $\lambda 4208$, $\lambda 4613$, and $\lambda 5112$ lines. Though the $\lambda 4208$ feature resides within the same CN bandhead as the Sr II $\lambda 4215$ line, it is strong and unblended enough to allow an abundance measurement. We adopt the mean value of these three lines, $[\text{Zr}/\text{Fe}] = 0.52$.

The Ba abundance was determined from the $\lambda 5854$, $\lambda 6142$, and $\lambda 6494$ lines shown in Figure 5. Though available, the $\lambda 4554$ line is on the damping portion of the curve of growth. The Ba lines in HE 0414–0343 are mostly free of molecular C contamination. We adopted the mean abundance ratio, $[\text{Ba}/\text{Fe}] = 1.87$.

The La abundance was derived from five clean lines: $\lambda 4740$, $\lambda 4748$, $\lambda 4824$, $\lambda 6262$, and $\lambda 6390$. We adopt the mean abundance, $[\text{La}/\text{Fe}] = 1.48$. The Ce abundance was derived from four lines: $\lambda 4739.51$, $\lambda 4739.52$, $\lambda 4747$, and $\lambda 4882$. The $\lambda 4739.51$ and $\lambda 4739.52$ lines are heavily blended; however, there is no other strong feature in the region of these lines, thus we derived their abundance simultaneously, as it is impossible to determine if either line yields a different abundance. We adopt $[\text{Ce}/\text{Fe}] = 1.42$ based on three lines, as we treat the abundances of the Ce $\lambda 4739.51$ and Ce $\lambda 4739.52$ lines as a single abundance.

The Nd abundance was obtained from three clean lines in the red portion of the spectrum, shown in Figure 5: $\lambda 5310$, $\lambda 5311$, and $\lambda 5319$. The mean abundance of these features, which are all in good agreement with each other, $[\text{Nd}/\text{Fe}] = 1.63$.

The Sm abundance was derived from $\lambda 4318$, $\lambda 4434$, and $\lambda 4519$. The $\lambda 4318$ line is in a C-rich region, while the $\lambda 4519$ line is blended with C, thus the C abundance was treated as a free parameter to best fit the observed spectrum in these syntheses. Despite the blends, we were still able to derive abundances that are in very good agreement with each other. We also evaluated $\lambda 4433$ and $\lambda 4687$, both of which are severely blended with C (and also Fe in the case of $\lambda 4687$) and determined upper limits for both features, that are very close to the final value. We obtain an average value of the abundance derived from the three measured lines: $[\text{Sm}/\text{Fe}] = 1.42$.

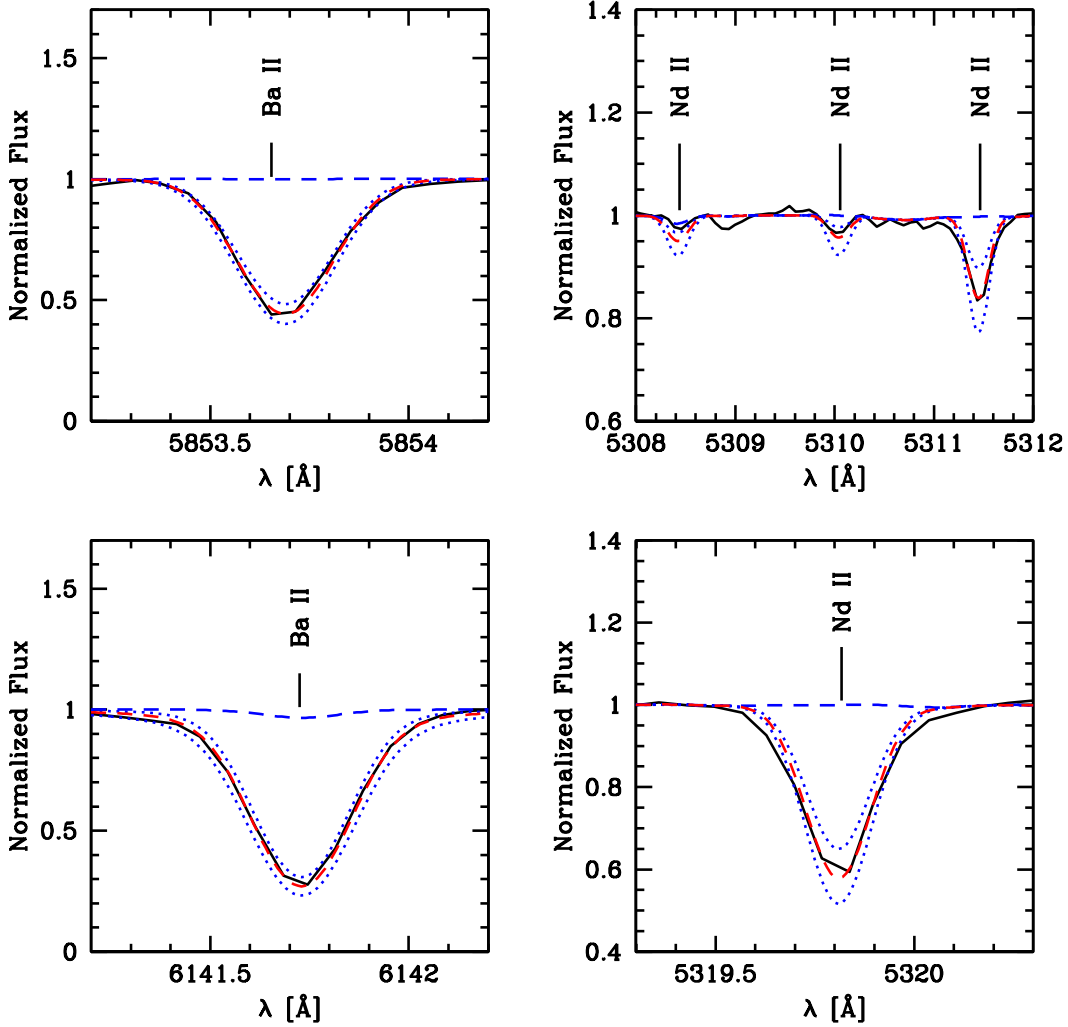


Fig. 5.— Ba features (left panels) in the HE 0414–0343 spectrum (solid black line), along with the best fit abundance (red dashed line), Ba abundances changed a factor of two above and below the best fit abundance (blue dotted line), and a synthetic spectrum for which no Ba is present (blue dashed line). The top left panel shows the $\lambda 4554$ line, the middle left panel shows the $\lambda 5853$ lines, and the bottom left panel shows the $\lambda 6141$ line. The Nd features (right panels) are plotted in the same scheme as Ba. The top right panel shows the $\lambda 5310$ and $\lambda 5311$ lines, the middle right panel shows the $\lambda 5319$ line, and the bottom right panel shows the $\lambda 5293$ line.

The Eu abundance was determined solely from the $\lambda 6645$ line, yielding $[\text{Eu}/\text{Fe}] = 1.23$.

As seen in the left panel of Figure 6, this line is blended with CN. Typically, the $\lambda 4129$ line is used; however, the region surrounding that line is heavily blended with molecular CH features, as well as other neutron-capture elements, preventing any abundance measurements.

The Dy abundance was determined from the $\lambda 4449$ feature, which is heavily blended with molecular C. We had to increase the C abundance to match the features in this region. We therefore present the Dy abundance of $[\text{Dy}/\text{Fe}] = 1.59$ with a larger uncertainty of 0.3 dex. However, we do include it in our analysis for diagnostic purposes with regard to the nature of the nucleosynthetic origins of HE 0414–0343. The magnitude of its abundance is similar to other abundances of neutron-capture elements that were easier to determine.

The Er abundance was derived from the $\lambda 3682$ line yielding $[\text{Er}/\text{Fe}] = 1.56$. Given the low S/N and CH molecular features in the region, this abundance has a large uncertainty of 0.30 dex; however, similar to Dy, the magnitude of the derived abundance for Er is consistent with other neutron-capture elements in the star.

The Yb abundance was determined from the $\lambda 3694$ line in the blue portion of the spectrum, as shown in the right panel of Figure 6. It resides on the red side of a blended feature which includes neutron-capture and Fe-peak elements, and has isotopic splitting. We derive $[\text{Yb}/\text{Fe}] = 1.43$.

Finally, we obtained the Pb abundance from the $\lambda 3683$ and $\lambda 4057$ features. We considered isotopic splitting by adopting the solar isotopic Pb ratios. We derived $[\text{Pb}/\text{Fe}] = 2.45$ from the $\lambda 3683$ line. The $\lambda 4057$ Pb feature is blended with CH. The linelist available for the CH features in that region is not complete, which leaves many lines unidentified. To reduce blending effects, we adjusted the wavelengths of some of the features in the linelist to reflect those listed in Moore’s Solar Atlas (Moore et al. 1966). We also adjusted the C abundance to match that of a nearby CH feature at 4058.2 Å and we modified the oscillator strengths of some nearby CH features to better reflect the observed spectrum, with no impact on our Pb measurement. We derived a mean value $[\text{Pb}/\text{Fe}] = 2.53$. While each of the two lines individually has a large uncertainty due to many unknown (likely CH) blends and low S/N in the case of the $\lambda 3683$ line, their agreement is encouraging. Given the strength of both lines, as seen in Figure 6, it is obvious that the Pb abundance is significant in this star. Since Pb is a neutral neutron-capture species, we use the NLTE-corrected value for our analysis and interpretation. We note here that non-LTE effects of neutral Pb in metal-poor stars are strong (Mashonkina et al. 2012) which become larger for cooler stars and lower metallicities. The Pb I correction for HE 0414–0343 is $\Delta_{\text{NLTE}} = 0.56$ dex for the $\lambda 4057$ line, which would increase our Pb abundance to $[\text{Pb}/\text{Fe}] \sim 3.09$.

5. Classification of stars with overabundances in neutron-capture elements associated with the s-process

The abundances of s- and r-process stars reflect different nucleosynthetic processes that have either occurred before the star’s formation (in the case of the r-process) or in a companion star during stellar evolution (in the case of the s-process). Hence, criteria for identifying stars with these enrichment patterns have been suggested (e.g., [Beers & Christlieb 2005](#)) and classes of objects have been established based on certain abundance ratios, i.e., CEMP-s, CEMP-r/s and CEMP-r stars. The aim is to better understand the nature of these objects and, more generally, metal-poor stars enriched in neutron-capture elements. HE 0414–0343 shows signs of an s-process enrichment so we aim to classify it, given its abundance pattern to learn about its origins.

One classification method is to compare the stellar abundance patterns with the scaled Solar System s- and r-process patterns. While this has worked extremely well for strongly r-process enhanced stars (owing to the universality of the r-process pattern, e.g., [Snedden et al. 2000](#), [Frebel et al. 2007](#)), the s-process is more complex because metallicity strongly affects the s-process abundance pattern (e.g., [Gallino et al. 1998](#)). Ba and Eu abundances have been used as a proxy for distinguishing between s- and r-process element contributions. According to the [Beers & Christlieb \(2005\)](#) definitions, s-process enhanced metal-poor stars are classified by $[\text{Ba}/\text{Fe}] > 1.0$ and $[\text{Ba}/\text{Eu}] > 0.5$, while r/s-enhanced stars fall within the range of $0.0 < [\text{Ba}/\text{Eu}] < 0.5$ and also having $[\text{Ba}/\text{Fe}] > 1.0$. Accordingly, HE 0414–0343 would be classified as a CEMP-r/s star. As described further below, we find that the $[\text{Ba}/\text{Eu}]$ ratio does not well correlate with the nature of the abundance patterns of many of these stars found in the literature, however.

5.1. Assessing neutron-capture abundances ratios

We use the CEMP-s and CEMP-r/s stars from Table 6 of [Placco et al. \(2013\)](#), along with the two new stars presented in that paper, HE 1405–0822 ([Cui et al. 2013](#)) as well as HE 0414–0343 to investigate the nature of their abundance patterns, in particular to learn about the origin of CEMP-r/s stars. In the top left panel of Figure 7, we plot their $\log\epsilon(X)$ abundances of the (un-normalized) neutron-capture elements versus atomic number, Z . We are here switching to the $\log\epsilon$ abundance notation to investigate an absolute abundance scale rather than that normalized to the Sun. Only stars with $-2.8 < [\text{Fe}/\text{H}] < -2.3$ are included in an attempt to remove gross metallicity effects expected to play a role in s-process nucleosynthesis. This reduced the sample to 11 CEMP-s and 14 CEMP-r/s stars.

CEMP-r/s stars have higher $\log \epsilon$ (heavy neutron-capture element) abundances than the CEMP-s stars. The overall ranges in the $\log \epsilon(\text{Ba})$ and $\log \epsilon(\text{Pb})$ abundances covered within this sample are very large at ~ 2.0 dex, and the range in $\log \epsilon(\text{Y})$ and $\log \epsilon(\text{Eu})$ even larger at ~ 2.5 dex. Interestingly, we find that the stars that make up our sample cover these large abundance ranges rather evenly, suggesting a continuum.

To better assess the origin and range of the observed neutron-capture patterns, we then normalize the abundances to $\log \epsilon(\text{Ba}) = 0$ (middle panel of Figure 7). We use Ba for normalization because it is considered to be produced mainly in the s-process that enriched the Solar System (Arlandini et al. 1999). The CEMP-s stars have an average $[\text{Y}/\text{Ba}] = (\log \epsilon(\text{Y})_{\star} - \log \epsilon(\text{Y})_{\odot}) - (\log \epsilon(\text{Ba})_{\star} - \log \epsilon(\text{Ba})_{\odot}) = (\log \epsilon(\text{Y})_{\star} - \log \epsilon(\text{Ba})_{\star}) - 0.03 = \log(\epsilon(\text{Y})/\epsilon(\text{Ba}))$ ratio of ~ -0.5 but with a spread of ~ 1 dex for Y abundances, when considering the Ba-normalized values. The CEMP-r/s stars have a lower average $\log(\epsilon(\text{Y})/\epsilon(\text{Ba}))$ ratio of ~ -1 , but a similar-sized spread of 1 dex for the Y abundances. By comparison, the Solar System ratio is ~ 0.0 , which falls within the CEMP-s regime. For those stars with measured Pb abundances – a difficult task in CEMP stars – the $\log(\epsilon(\text{Pb})/\epsilon(\text{Ba}))$ ratio varies greatly, > 2 dex, in the CEMP-s stars. This apparent spread in Pb is even larger in the Ba-normalized abundance patterns than in the absolute overall abundance patterns. Moreover, the $\log(\epsilon(\text{Pb})/\epsilon(\text{Ba}))$ ratio is often negative. In the CEMP-r/s stars, the $\log(\epsilon(\text{Pb})/\epsilon(\text{Ba}))$ ratio is ~ 0 for most stars, while the Pb spread is only ~ 0.75 dex. Finally, we normalize the abundance patterns to $\log \epsilon(\text{Eu}) = 0$, see bottom left panel of Figure 7. We find that the $\log(\epsilon(\text{Pb})/\epsilon(\text{Eu}))$ ratios for the CEMP-r/s stars are generally lower than those of CEMP-s stars. Also, there is a smaller spread among the $\log \epsilon(\text{Pb})$ abundances. Overall, the behavior is similar to the Ba-normalized case.

Considering the $\log(\epsilon(\text{Y})/\epsilon(\text{Ba}))$ ratio, there is a large spread but there is a fairly smooth transition between CEMP-s and CEMP-r/s stars with no sharp dividing line. This transition can also be seen in Figure 1 of Masseron et al. (2010). Together with the $\log(\epsilon(\text{Y})/\epsilon(\text{Ba}))$ ratios, the $\log(\epsilon(\text{Pb})/\epsilon(\text{Ba}))$ and $\log(\epsilon(\text{Pb})/\epsilon(\text{Eu}))$ ratios suggest that there is a transition and no clear, distinct separation into subgroups. Our star, HE 0414–0343, also demonstrates the continuum nature of the transition between CEMP-s and CEMP-r/s stars, as its abundance pattern is located between the more extreme CEMP-s and the CEMP-r/s stars, as can be seen in Figure 7 (green line in all panels).

From this exercise we conclude that considering only observed $[\text{Ba}/\text{Eu}]$ abundance ratios to classify stars into the CEMP-s and CEMP-r/s stars classes is not sufficient. Indeed, as can be seen in Figure 8, using $[\text{Ba}/\text{Eu}] = 0.5$ as the criterion to distinguish between CEMP-s ($[\text{Ba}/\text{Eu}] > 0.5$) and CEMP-r/s stars ($0 < [\text{Ba}/\text{Eu}] < 0.5$) results in less than $\sim 50\%$ of the cases being in correctly classified, compared to results based on a detailed abundances

analysis assessment. Therefore, the usefulness of the [Ba/Eu] ratio in classifying CEMP-s and CEMP-r/s into two distinct subcategories appears to be limited.

Moreover, the labeling of “CEMP-s” and “CEMP-r/s” suggests that there is a different underlying nucleosynthetic origins for these stars, and specifically, that there is an r-process component involved for r/s stars. But none has yet been found (e.g., [Jonsell et al. 2006](#)) and one has to question the existence of such an r-process component. A more comprehensive assessment and especially a physically-motivated explanation is thus needed to better understand metal-poor stars showing neutron-capture element enhancements associated with the s-process.

The s-process builds up in AGB stars over each thermal pulse after the third dredge up events begin. The timing of the mass transfer of the enriched material in relation to the number of thermal pulses experienced by the donor AGB star will help determine what the observed abundances will be. The evolutionary status of the observed CEMP stars today (e.g., dwarf, giant) also plays an important role ([Stancliffe & Glebeek 2008](#); [Placco et al. 2014](#)).

As [Figure 8](#) further shows, the [Y/Ba] ratio seems to provide a better way to group and classify these stars, although large spreads in other neutron-capture elements may be found in each class. Such classification shall be introduced in [Section 7](#). Both Y and Ba are predominantly made in the s-process. Their relative contributions might thus shed light on the s-process and the build up of the s-process peaks in AGB stars over each thermal pulse after the third dredge up events begin.

To further investigate this apparent continuum of s-process enhancements in our sample, we now compare the individual stellar abundance patterns in detail with predictions of the s-process in models of AGB stars.

6. Comparison with model AGB s-process yields

The s-process is thought to occur in thermally-pulsating AGB stars of $\simeq 0.8$ to $8 M_{\odot}$ ([Busso et al. 1999](#); [Karakas & Lattanzio 2014](#)). The neutrons that fuel the s-process are primarily produced via the $^{13}\text{C}(\alpha, n)^{16}\text{O}$ reaction that occurs as a result of partial CN cycling ([Abia et al. 2001](#); [Smith & Lambert 1990](#)). The neutron-capture occurs in the He-shell and the newly created s-process elements are brought to the surface as a result of third dredge-up mixing episodes. Detailed calculations by [Gallino et al. \(1998\)](#), [Bisterzo et al. \(2009\)](#), [Cristallo et al. \(2011\)](#) and [Lugaro et al. \(2012\)](#), among others, have been performed to better understand the s-process. To reproduce observed s-process abundances in metal-poor

companion stars, stellar models have been created that e.g., vary the mass and the metallicity of the AGB star, the size of the ^{13}C pocket, and take into account dilution effects.

We present a new version of the AGB model of a 1.3M_{\odot} star with $[\text{Fe}/\text{H}] = -2.5$ previously calculated for [Placco et al. \(2013\)](#). The new model was calculated with the the Mount Stromlo Stellar Evolutionary code ([Karakas et al. 2010](#)), using the same input physics as before, except with updated low-temperature molecular opacities. The model star was evolved from the zero age main sequence to the AGB. The model star underwent 21 thermal pulses during the AGB phase, most of which included third dredge up events, resulting in a total dredge up of 0.049M_{\odot} from the core of the star to its surface. Using the [Vassiliadis & Wood \(1993\)](#) prescription for mass loss, we determined that 0.5M_{\odot} is lost during the AGB stage. The resultant abundances at each thermal pulse were calculated in the same manner as in [Lugaro et al. \(2012\)](#). The final abundance is reached at thermal pulse number 19, thereafter the surface abundances do not change.

[Placco et al. \(2013\)](#) found two new stars showing signs of s-process nucleosynthesis and compared their abundances to the yields of an earlier version of this AGB model, along with the abundances of several stars classified as CEMP-s and CEMP-r/s stars in the literature. For a comparison, they also used a range of other AGB star models spanning $0.9\text{M}_{\odot} \leq \text{M} \leq 6\text{M}_{\odot}$ at $[\text{Fe}/\text{H}] = -2.2$, some of which include pre-enrichment from the r-process. These models are described in detail in [Karakas \(2010\)](#) and [Lugaro et al. \(2012\)](#). [Placco et al. \(2013\)](#) also considered details of the mass transfer event across a binary system, which necessarily results in dilution of the s-process material once it is mixed onto the observed star’s outer atmosphere.

To seek a physical motivation for the variety of s-process enriched stars, we set out to investigate the physics of the s-process in AGB stars and whether the resulting yields can explain the abundances of HE 0414–0343 and the sample of literature stars.

6.1. HE 0414–0343 Abundance Pattern Analysis

We first extend the Placco et al. analysis to HE 0414–0343 and then later also to their sample (see Section 6.2). To account for dilution of the s-process material in the receiver stars’ outer atmosphere, we considered two different options: 5% and 50% cases, where the latter imitates a mass transfer event when the recipient star is a red giant having 50% of its mass in the convection zone and the 5% case represents a less-evolved star. Since we do not know how long ago the mass transfer event took place, we consider both options for HE 0414–0343 and each of the sample stars.

The analysis specific to HE 0414–0343 then consisted of two steps: a) comparison of its abundance pattern to the same set of AGB models as in [Placco et al. \(2013\)](#), specifically, the $1.3 M_{\odot}$ described above and the set of $[\text{Fe}/\text{H}] = -2.2$ models from [Lugaro et al. \(2012\)](#). For the second step b) we extract an r-process pattern from the overall observed abundance pattern, and compare the “decontaminated” abundance pattern to the thermal pulse abundance distributions of all models.

Regarding step a) and following [Placco et al. \(2013\)](#), we minimized the differences between the surface abundance distribution after each thermal pulse and the observed abundances for HE 0414–0343 to find the best match. In particular, we select the best match based on the smallest overall residual (see e.g., [Figure 9](#)) over different neutron-capture element mass ranges. We distinguish five cases. Case i) the full observed neutron-capture abundance pattern (“full residual”), case ii) just abundances near the first peak of the s-process (Sr, Zr, Y; “first peak residual”), case iii) just abundances near the second peak of the s-process (Ba, Sm), case iv) just for abundances of the heaviest neutron-capture elements, e.g., Eu and above (“Eu peak residual”), and case v) only for elements with $Z > 40$, which excludes the first peak abundances. Breaking up the matching procedure into these element groups helps to disentangle the build up of s-process elements at the surface of the AGB star. Over time, heavier and heavier s-process elements are created and dredged-up in the AGB star with each thermal pulse. The relative contributions to elements in groups ii) to iv) should be reflected in the residual of the respective group.

The results of this step are best understood in the context of the entire sample that we analyzed in an analogous way, and which is described in [Section 6.2](#). Hence, in [Section 6.2](#), we discuss the analysis results of the entire sample (including HE 0414–0343), together with our conclusion regarding the nature and origin of s-enriched CEMP stars.

But we note here already that, similar to what was found in [Placco et al. \(2013\)](#), one of the thermal pulse abundance distributions of the updated low-metallicity AGB model provides the best match to the overall abundance pattern of HE 0414–0343. However, r-process elements such as Eu and Dy around the second peak are still overabundant compared to this best model match. This kind of discrepancy was also found for the CEMP-r/s stars analyzed in [Placco et al. \(2013\)](#), suggesting HE 0414–0343 to be in the same category. To first order this confirms why CEMP-r/s stars are not classified as CEMP-s – they have a curious relative overabundance of heavy neutron-capture elements compared to lighter ones. This could indicate a contribution of r-process elements.

Regarding step b), to investigate this heavy-element discrepancy as well as the nature of the CEMP-r/s abundance pattern and especially the alleged “r” component of “CEMP-r/s” stars, we “extract” an arbitrary amount of r-process material (but following the r-process

pattern) from the abundance pattern of HE 0414–0343. If the binary system formed in an r-process enriched gas cloud, extracting an r-process signature should leave a cleaner s-process signature since the s-process elements present were only later created during the AGB phase of the more massive companion.

For the extraction, we decrease the $\log \epsilon$ (Eu) abundance in HE 0414–0343 by 0.5 and 1.0 dex. We use the abundance pattern of the r-process star CS 22892–052 (Snedden et al. 2003) to calculate the ratios of the neutron-capture elements relative to Eu in order to extract the putative r-process signature from these stars. These two “decontaminated” abundance patterns of HE 0414–0343 are then compared with the models, just like in step a). Again, the best overall match still did not reproduce the two decontaminated abundance patterns well. Although the heavy neutron-capture elements above Eu are better matched than before, the first and second peaks of the s-process are now very poorly reproduced. Interestingly, using our $[\text{Fe}/\text{H}] = -2.5$ AGB model and also a model with a pre-enrichment of 0.4 dex of r-process material both yielded similar, equally badly overall matches, with deviations ranging from 0.5 to 0.9 dex.

The important conclusion here is that our analysis indicates that there is no discernible r-process component present in the star. This is in contrast to the Beers & Christlieb (2005) criteria which would classify HE 0414–0343 as a CEMP-r/s given its $[\text{Ba}/\text{Eu}]$ ratio, and implying the existence of an r-process contribution. Our results thus render the “-r/s” classification unsatisfactory for explaining the origins of this star, and potential other stars with similar abundance patterns. A different classification seems necessary, as well as additional study of these stars in order to correctly identify their origin.

6.2. Literature Sample Analysis

We extend our detailed model comparison, step a), to the sample of literature stars used by (Placco et al. 2013, their Table 6) including their two new stars as well as HE 1405–0822 (Cui et al. 2013). However, we used just our updated low-metallicity AGB star model to obtain best matches to the five cases of the different atomic mass regions. We then compare the residuals of the each of the five cases to the measured $[\text{Y}/\text{Ba}]$ ratios of every star in the sample.

Despite the fact that the best matches are not always satisfactory, there is still information in the amount and direction of any discrepancy between the thermal pulse abundances and the observed abundance patterns. In Figure 9, we show cases i)-v) for the 5% and 50% dilution scenarios. In general, the stars classified as CEMP-s stars seem to have larger

$[Y/Ba]$ ratios than the CEMP-r/s stars, though there is overlap from -1 to -1.25 . We already noted this behavior in Section 5.1. But here we additionally find that for the CEMP-s stars, there is an anticorrelation between the full residual and the $[Y/Ba]$ ratio in the 5% dilution case, and no correlation in the 50% case. In the 5% case, strong anticorrelations are apparent between the second peak and Eu peak residuals with the $[Y/Ba]$ ratio. In the 50% case, the first and second peak are relatively well matched, while there is a ~ 1 dex spread in the Eu peak residual. The CEMP-r/s stars show no correlation for the full residual across all peaks with $[Y/Ba]$ in the 5% case and a weak correlation in the 50% case. In the 5% case, there is a weak anticorrelation in the first peak residual with the $[Y/Ba]$ ratio whereas in the Eu peak residual, there is perhaps a weaker correlation with $[Y/Ba]$. The 50% case essentially indicates no correlations between the residual of any peak and the $[Y/Ba]$ ratio. Additional results of this analysis will be given in Section 7.1.

Given the complicated nature of the full abundance pattern residual, we adopt the results of case v which are presented in Figures 9 and 10. We made this choice because it is generally difficult to interpret the first-peak neutron-capture elements in the sample stars due to the many possible nucleosynthetic pathways (e.g., a poorly-understood light element primary process - Travaglio et al. 2004) that led to their creation. In the appendix, we present the abundance patterns of all sample stars together with their respective best matches from our thermal pulse abundance distribution comparisons.

7. The classification and origin of CEMP-sA,sB,sC stars

Given the smooth transition between stars traditionally distinctly defined as CEMP-s and CEMP-r/s stars, i.e., as seen in Figure 7, we explore a new classification scheme for our sample which does not assume any r-process contribution. The overall goal is to find a scheme that accounts for the different patterns as well as the smooth transition regarding the magnitude of the s-process abundance enhancement. We designate the new classes CEMP-sA, CEMP-sB, and CEMP-sC. CEMP-sA stars have the “most traditional” s-process abundance pattern and the least negative $[Y/Ba]$ ratios spanning the range $-0.9 < [Y/Ba] < -0.3$, whereas CEMP-sC stars have an abundance pattern that deviates the most from the usual s-process abundance pattern, while still maintaining an s-process enhancement and, correspondingly, have the largest negative $[Y/Ba]$ ratios, with $[Y/Ba] < -1.5$. CEMP-sB stars fall in the middle, with $-1.5 < [Y/Ba] < -0.9$. Table 5 lists our definitions and classifications for the literature sample we have employed in this study.

To facilitate future classifications of undiscovered s-process stars, we have provide a web-

based tool⁵ that automatically classifies user-input stars based on their abundance patterns. It determines the best match of a given thermal pulse abundance distribution of our low-metallicity AGB model and provides plots of other stars that have been classified the same way, such that a comparison of the entire neutron-capture element pattern is made available.

Following the new classification it is important to investigate if there is an underlying physical mechanism that could explain the origin of the continuum of s-process patterns. Three plausible evolutionary scenarios for the smooth transition from CEMP-sA to CEMP-sB to CEMP-sC are discussed below.

7.1. Thermal Pulse Number Stratification

The abundance distribution of our low-metallicity AGB model’s best matched thermal pulse is a potential predictor of the CEMP classification. The abundance patterns of the CEMP-sA stars are best matched by the corresponding nucleosynthesis yields of thermal pulse no. 5 in the 5% dilution case. Residuals are shown in Figure 9. The abundances of the first s-process peak are consistently under-predicted in the AGB model by ~ 0.2 dex. The second s-process peak is over-predicted in the model by ~ 0.3 dex and the Eu region and third s-process peak are over-predicted by ~ 0.2 dex, even when a +0.5 dex NLTE correction is applied to the Pb abundance. The CEMP-sC stars show the largest deviations between the observations and best-matched model yields. In that case, the first s-process peak is over-predicted by ~ 0.5 dex, the second peak is under-predicted by ~ 0.1 dex, and the third peak is even more under-predicted by ~ 0.4 dex. The third peak is especially under-predicted when the NLTE correction is applied to Pb. Given the large abundances of second and third peak s-process elements, later thermal pulses, which have increased heavy neutron-capture element abundances, more closely match these stars. The CEMP-sB stars, predictably, fall in between the CEMP-sA and CEMP-sC stars.

The 50% dilution case is similar in that it reveals that the CEMP-sA stars and the CEMP-sC stars form distinct groups. This is especially apparent in the first s-process peak residuals. The first peak is under-predicted by ~ 0.2 dex by best-matched model yields in the CEMP-sA stars and over-predicted by ~ 0.3 dex in the CEMP-sC stars. The second peak is well matched in the CEMP-sA stars with a slight overprediction of only ~ 0.1 dex, but under-predicted in the CEMP-sC stars by ~ 0.4 dex. The third peak is underpredicted in all stars but one, with the average underprediction for the CEMP-sA stars being ~ 0.3 dex and ~ 0.8 dex for the CEMP-sC stars. The best matched thermal pulse numbers are larger in

⁵<http://www.nd.edu/~vplacco/sprocess-classes.html>

the CEMP-sA stars in this dilution case (7-19), which is expected since each thermal pulse represents more s-process material. The CEMP-sC stars are all best matched at thermal pulse 19, i.e., the final abundance of the model. As with the 5% dilution case, the CEMP-sB stars fall in the middle of these two extremes. While it is difficult to directly map the best matched thermal pulse number to the classification, it does show some correlation.

We then compared the best matched thermal pulse number with the $[Y/Ba]$ ratio. The CEMP-s and CEMP-r/s stars form distinct groups. We further investigated the best matched thermal pulse number as a potential key to the physical origin of the $[Y/Ba]$ continuum. We accomplished this in two stages. First, we attempt to identify the relationship between the CEMP s-process sub-classifications (both traditional and new) and the best matched thermal pulse numbers. Second, we examine how well the abundance patterns are fitted by the best matched thermal pulse numbers to seek a physical explanation for the observed abundance distribution.

In the 5% dilution case, there is a large spread of ~ 1 dex in the $[Y/Ba]$ ratio after 5 thermal pulses. A large number of stars are also best matched after 19 thermal pulses. All the CEMP-s stars are best matched at 5 thermal pulses, while the CEMP-r/s stars span a larger range of best matched thermal pulse numbers from 5-19, with a majority of the stars being best matched at thermal pulse number 19. Before thermal pulse 5, the AGB star is not (yet) a suitable donor star. The first third dredge up event happens at that thermal pulse number in the model and then the increasing pulses allow for the AGB star to build up s-process material on its surface which later gets transferred onto the surface of the observed metal-poor star.

In the 50% dilution case, we see this same degeneracy of best matched thermal pulse numbers, again at 19 thermal pulses, but not at the low number end. The abundances of CEMP-r/s stars are best matched over a tight range of thermal pulse numbers (18-19), while the CEMP-s stars' abundances span a range from 5-19 thermal pulses. The degeneracy at 19 thermal pulses is likely due to the fact that the model's surface abundances do not change after the model star has undergone 19 thermal pulses and further thermal pulses do not alter the AGB star surface abundances anymore.

Given the apparent connection between the traditional classifications and the best matched thermal pulse number, we investigate how the new designations corresponded to the best matched thermal pulse number. Indeed, the thermal pulse number and the classification of CEMP-sA, -sB, and -sC are correlated such that low numbers (~ 5) tend to correspond with CEMP-sA stars and high numbers of thermal pulses (~ 19) correspond with CEMP-sC stars, while the CEMP-sB star abundances lead to thermal pulse numbers between 5 and 19. We note, however, that many of the best matches have residuals of more than ± 0.5 dex

for some elements. In some of these cases, it is apparent that the residual analysis breaks down since the model element abundances are not large enough, even at the highest thermal pulse numbers, to reproduce the observations.

Given these results, we consider the thermal pulse number as a proxy for the processes of the mass transfer event. Specifically, it could represent the timing of the mass transfer. Lower thermal pulse number indicate an earlier transfer from the thermally pulsing AGB companion star, soon after the onset of its s-process nucleosynthesis. Thus, the s-process pattern would not have built up nearly as much of the heavier neutron-capture elements as a mass transfer that occurred at a later time, i.e. one with a higher thermal pulse number.

It could also represent the physical distance between the stars in the binary system. Two stars with close physical separation will undergo an earlier mass transfer, corresponding to a lower thermal pulse number. If the thermal pulse number alone is what causes the observed spread in the [Y/Ba] ratios, then only a small dispersion in the [Y/Ba] ratio would be expected for a given thermal pulse number. Nevertheless, the degeneracy at both low and high thermal pulse numbers suggests these to be only a partial explanation of the CEMP-sA to CEMP-sC transition.

7.2. Neutron sources in early AGB stars

While the thermal pulse number seemed to be a promising explanation for the traditional classification scheme, it falls short with the [Y/Ba] ratio diagnostic. That is not to say that the thermal pulse number holds no information. The model we are using describes a $1.3 M_{\odot}$ AGB star which we can compare to more massive AGB star models at $[\text{Fe}/\text{H}] = -2.2$ using the predictions from [Lugaro et al. \(2012\)](#). [Abate et al. \(2015\)](#) recently performed a similar analysis using binary population synthesis models and a range of AGB masses from models of $[\text{Fe}/\text{H}] = -2.2$.

Models of higher-mass than $1.3 M_{\odot}$ but less than $3 M_{\odot}$ result in an s-process pattern characterized by higher second and third peak s-process element abundances. This occurs because models of less than $\approx 3 M_{\odot}$ experience more thermal pulses and deeper third dredge-up than the $1.3 M_{\odot}$ case. For models above $3 M_{\odot}$, the $^{22}\text{Ne}(\alpha, n)^{25}\text{Mg}$ reaction starts to dominate and the s-process distribution changes such that there is more first s-process peak elements than second or third peak (that is, $[\text{Y}/\text{Ba}] > 0$) ([Lugaro et al. 2012](#); [Fishlock et al. 2014](#)). We also note that variations in the size of the ^{13}C pocket can change the ratio of the s-process elements from light “ls” to heavy “hs”. The ratio [ls/Fe] is an average of elements at the first s-peak, e.g., Sr, Y, Zr, whereas [hs/Fe] is an average of elements at the second

peak, e.g., Ba, La and Ce (see e.g., [Masseron et al. 2010](#); [Lugaro et al. 2012](#)). The ratios of [hs/ls] and [Pb/hs] increase with increasing ^{13}C pocket size, indicating that a larger number of neutrons relative to Fe-seed nuclei produces more Ba, La, Ce and Pb, relative to elements at the first peak ([Bisterzo et al. 2011](#); [Lugaro et al. 2012](#); [Fishlock et al. 2014](#)).

The CEMP-sA stars present better residuals when using our low-metallicity, low-mass AGB model, especially with regard to the first peak elements. However, there are systematic discrepancies between the abundance patterns of the CEMP-sC stars (and to a lesser degree, of the CEMP-sB stars) and the low-mass model. While some variations in the AGB companion mass may provide a better fit for some of the CEMP stars, it is not the only solution to the transition from CEMP-sA to CEMP-sC. This is because the [Y/Ba] ratio varies from ≈ -0.7 to positive values as the stellar mass is increased. [Lugaro et al. \(2012\)](#) discuss this point in more detail, noting that AGB models can only produce $[\text{ls/hs}] > -1$ as a consequence of the way in which the s-process operates (see also [Busso et al. 2001](#)). The increase of the [Y/Ba] (or [ls/hs]) ratio with increasing stellar mass is a direct consequence of the activation of the $^{22}\text{Ne}(\alpha, n)^{25}\text{Mg}$ neutron source. Other suggestions for the origin of the CEMP-sC stars may be found in physics not currently included in 1-D AGB models such as proton-ingestion episodes near the tip of the AGB phase that result in high neutron densities for short times (such as in post-AGB stars, [Herwig et al. 2011](#)).

At the lowest metallicities the efficiency of the s-process is strongly dependent on the number of available Fe seed nuclei. One way to confirm this observationally is to examine the [Ba/C] ratio as a function of metallicity. The right panel of Figure 5 in [Masseron et al. \(2010\)](#) explores this and they find a tight correlation between [Ba/C] and [Fe/H] in their CEMP-s stars. In Figure 11, we plot the same axes, along with the empirical trend from Figure 5 of [Masseron et al. \(2010\)](#) in the black solid line, with the black dotted lines representing the area in which most of the CEMP-s stars are plotted. We find that our CEMP-sA stars mostly fall within this same region even over the narrow range of metallicity that was chosen.

That the CEMP-sA stars fall within the same region of Figure 11 is an indicator that the source of carbon and s-process elements is similar. It also indicates that the neutron source operating in the AGB companion star was similar. In Figure 7 of [Masseron et al. \(2010\)](#), they do not find a correlation between [Ba/C] and [Fe/H] for their CEMP-rs stars. Similarly, the CEMP-sC stars in our Figure 11 do not show the tight correlation between [Ba/C] and [Fe/H] that the CEMP-sA stars of our sample and the CEMP-s stars from [Masseron et al. \(2010\)](#) do. This is an indicator that a different neutron source operates in the AGB companions of the CEMP-sC stars. AGB models cannot explain the alleged high r-process contribution in the CEMP-sC stars nor the very low [Y/Ba] < -1 (e.g., [Lugaro et al. 2012](#)). This indicates that AGB stars (covering a range of masses) are not responsible

for the CEMP-sC abundance patterns (see detailed discussion by [Cohen et al. 2003](#)).

We can rule out the $^{22}\text{Ne}(\alpha, n)^{25}\text{Mg}$ reaction operating in high-mass AGB star models but what about this neutron source in rotating massive stars? Yields of s-process elements from rotating massive stars indicate that elements at the first s-process peak are predominantly overproduced, with little barium or lead synthesized ([Pignatari et al. 2008](#); [Frischknecht et al. 2012](#)). This suggests that the s-process in massive stars also cannot be responsible for the abundance distribution of CEMP-sC stars, unless the AGB companions also (somehow) experience considerable r-process nucleosynthesis much beyond what is currently predicted.

7.3. Initial neutron-capture element abundances of CEMP-sA,sB,sC stars

In plots of $[\text{Ba}/\text{Fe}]$ or $[\text{Sr}/\text{Fe}]$ versus $[\text{Fe}/\text{H}]$ of halo field stars (e.g., bottom panels of Figure 18 in [Frebel & Norris 2013](#)), there is a huge spread of nearly 3 dex in regular halo stars with $[\text{Fe}/\text{H}] < -2.0$ (and no strong overabundance in carbon) that do not show any particular enhancement in neutron-capture elements, i.e., stars with $[\text{Ba}/\text{Fe}]$ or $[\text{Sr}/\text{Fe}] < 1$. Similarly, in stars with enhanced s-process abundances, i.e., stars with $[\text{Ba}/\text{Fe}]$ or $[\text{Sr}/\text{Fe}] > 1$, we also observe a > 2 dex spread (e.g., top panels of Figure 18 in [Frebel & Norris 2013](#)). Given that the spread in neutron-capture element abundances are roughly of the same magnitude in both regular metal-poor stars and s-process stars, one proposal is that the differences between CEMP-sA, CEMP-sB, and CEMP-sC stars are caused by variations in the level of pre-enrichment in neutron-capture elements in the birth gas clouds by progenitor generations (due to the chemical evolution and analogous to the alleged r-process contribution discussed earlier) in addition to the s-process material received from the AGB companion at later times.

S-process rich stars have only been found at metallicities of $[\text{Fe}/\text{H}] > -3$ (albeit with one exception, i.e., [Sivarani et al. 2006](#)) and the rise of s-process enrichment through stellar winds from AGB stars has been placed at $[\text{Fe}/\text{H}] \sim -2.6$ ([Simmerer et al. 2004](#)). This suggests that various chemical enrichment processes were already operating at $[\text{Fe}/\text{H}] \sim -2.5$, including different kinds of neutron-capture processes occurring in supernovae and the more massive AGB stars. Altogether, in a yet to be understood way, chemical evolution produced stars with huge spreads in neutron-capture abundances whereas their light element ($Z \leq 30$) abundance ratios (e.g., $[\text{Ca}/\text{Fe}]$) are nearly identical (e.g., [Cayrel et al. 2004](#); [Frebel & Norris 2013](#)).

We examine the $[\text{Sr}/\text{Fe}]$ and $[\text{Ba}/\text{Fe}]$ abundance ratios of our sample stars to test if they could have partially originated from large variations of the neutron-capture elemental

abundances in the stars’ birth clouds. Specifically, we attempt to map them to the $[Y/Ba]$ ratio to determine if there is a connection between the initial birth abundances of the CEMP-sA, CEMP-sB, and CEMP-sC stars and the values that are now observed after the mass transfer event. As in the case of our r-process pattern extraction, we now attempt the reverse. We adjusted the $[Sr/Fe]$ and $[Ba/Fe]$ abundance ratios by subtracting an amount to represent the mass transfer s-process material. The adjusted abundances should then reflect the initial amount of neutron-capture elements of the receiver stars prior to the mass transfer of neutron-capture- and carbon-rich matter.

However, the adjusted abundance patterns of the receiver stars do not map well from the CEMP-sA, -sB, and -sC stars to the neutron-capture/carbon-normal metal-poor stars. Given this mismatch between the CEMP-sA, CEMP-sB, and CEMP-sC stars and the neutron-capture- and C-normal metal-poor stars, the idea that an initial spread in the abundances in the gas cloud would cause the observed continuum between CEMP-sA to CEMP-sC will likely take a more sophisticated approach. This is in part due to uncertainties in which s-process pattern to subtract, as it is likely different for each star. More high-resolution spectra of CEMP stars need to be obtained and analyzed to better investigate this scenario with a much larger sample.

8. Caveats and Considerations

In this work we have primarily used one low-metallicity AGB model to match to all stellar abundance patterns. The main reason we used the $1.3 M_{\odot}$ model so extensively is because it has a metallicity closest to the observed star, at $[Fe/H] = -2.5$. Nevertheless, we have used the $[Fe/H] = -2.2$ models to guide us in our interpretations regarding the behavior of general stellar and nucleosynthesis properties. These models, while at slightly higher metallicity, cover an extensive range of mass 0.9 to $6 M_{\odot}$ (Lugaro et al. 2012; Karakas et al. 2010).

We have made the assumption that the s-process pattern is built up in the same way for all stellar masses for a given metallicity although as a function of thermal pulses. Out of necessity, the biggest assumption is perhaps that the companion mass is the same for all our stars, but we discuss this further below. Despite this limitation, these assumptions are justified because we made a reasonable metallicity cut to select sample stars have similar metallicities from -2.7 to -2.3 . This ensures that our stars span over the stellar model metallicity of $[Fe/H] = -2.5$. Thermal pulse abundances in this model do give the best match to a CEMP-sA star compared to those of other models.

A more general issue that all AGB modelling faces is the formation and size of the ^{13}C pocket, from which the neutrons necessary for the s-process originate. The size of the pocket can be somewhat constrained by comparisons to observations of AGB stars and their progeny: post-AGB stars and planetary nebulae (see discussion in [Karakas & Lattanzio 2014](#)). In metal-poor post-AGB stars, spreads in the size of the pocket in the models of a factor of 3-6 are needed to account for the observation data ([Bonačić Marinović et al. 2007](#); [De Smedt et al. 2012](#)). Furthermore, in CEMP stars the spread needed to match the observational data can be upwards of a factor of 10 or higher ([Bisterzo et al. 2011](#); [Lugaro et al. 2012](#)). Central to the issue of how large the ^{13}C pocket is that we do not understand their formation process in AGB stars. Of particular interest to this work is that increasing the size of the ^{13}C pocket will decrease the $[\text{Y}/\text{Ba}]$ ratio. For example, from the models in [Lugaro et al. \(2012\)](#) we see that a $2M_{\odot}$ model of $[\text{Fe}/\text{H}] = -2.2$ will move from a positive $[\text{Y}/\text{Ba}]$ of 0.39 with no pocket to $[\text{Y}/\text{Ba}] = -0.57$ with the model with the largest ^{13}C pocket. As more low-metallicity AGB models with $[\text{Fe}/\text{H}] \approx -3$ become available we will further analyze how different ^{13}C pocket assumptions would affect the $[\text{Y}/\text{Ba}]$ ratio.

For future studies it would be helpful to have a better understanding about the details of the mass transfer so that the dilution of the transferred s-process material can be more accurately described (e.g., [Abate et al. 2015](#)).

To summarize, in order to further investigate CEMP s-process star abundances, more AGB star models are needed that cover a larger range of both initial mass and metallicity, especially for metallicities below $[\text{Fe}/\text{H}] = -2.5$. More observations of newly discovered s-process stars are also needed in order to create a larger statistical sample. These models and observed abundances can then be used to better probe AGB star mass and metallicity effects on the abundance patterns for a full physical explanation of the observations.

9. Summary and Conclusions

We have presented the red giant HE 0414–0343, a CEMP star with $[\text{Fe}/\text{H}] = -2.24$. Following a detailed abundance analysis, we find the star to possess a strong enhancement in the s-process elements. Based on its $[\text{Ba}/\text{Eu}]$ and $[\text{Ba}/\text{Fe}]$ ratios, this star falls under the traditional category of “CEMP-r/s” stars. We find HE 0414–0343 to most likely be in a binary system since its radial velocity has been varying over the course of our observations from 2004 to 2011.

To better understand HE 0414–0343 and the nature of “CEMP-r/s” stars, we also analyzed the abundance patterns of a sample of literature “CEMP-s” and “CEMP-r/s”

stars. The CEMP-s and CEMP-r/s categories as defined by [Beers & Christlieb \(2005\)](#) based on the $[\text{Ba}/\text{Eu}]$ ratio have been fundamental in recognizing the diverse nature of CEMP star abundances. We find, however, that this traditional way of using a cutoff in the $[\text{Ba}/\text{Eu}]$ ratio to classify these stars corresponds only poorly to “CEMP-s” and “CEMP-r/s” stars once the availability of their detailed abundances allows a more encompassing assessment of their abundances signatures. By instead utilizing the $[\text{Y}/\text{Ba}]$ ratio to characterize CEMP stars with neutron-capture element enhancements associated with the s-process, we can gain a better understanding of the origin of the s-process diversity. Investigation of the $[\text{Y}/\text{Ba}]$ abundance ratio in our sample shows that there is a continuum between the “CEMP-s” and “CEMP-r/s” stars, rather than a distinct cut off separating the two groups of objects with different origins.

We suggested a new classification scheme for s-process stars, CEMP-sA, CEMP-sB, and CEMP-sC, based on the different levels of $[\text{Y}/\text{Ba}]$ ratio values, rather than a different physical mechanism for their origin. We assign each sample star to one of the three new groups. The traditional “CEMP-s” would loosely correspond to CEMP-sA class, “CEMP-r/s” to CEMP-sC, and those stars who fill in the continuum between are CEMP-sB. The advantage of using the elements Y and Ba is that they are both easily measurable in CEMP stars. Moreover, using $[\text{Y}/\text{Ba}]$ provides an observable to confirm or refute our hypothesis that there is only one underlying physical mechanism that causes the large range of s-process abundance variations in these stars.

We compared the abundance patterns to AGB nucleosynthesis models and found that certain thermal pulse abundance distributions of the new low-metallicity $1.3 M_{\odot}$ model produced the best match to all stellar abundance patterns in our sample. The CEMP-sA stars were best matched this way. The CEMP-sB and CEMP-sC stars were however increasingly difficult to match. Their abundance patterns have an excess in the heavy neutron-capture abundances around Eu and above compared to lighter elements, such as Sr, and the AGB models. Upon investigation, we find that this excess cannot be explained by assuming these stars to have formed from gas already enriched with r-process elements.

We considered two cases for diluting the material in the stellar atmosphere of observed stars after the mass transfer of s-enriched material from the AGB star. This takes into account the unknown timing of the mass transfer event during the receiver star’s evolution. We also explored the build up of the s-process elements in the low-metallicity AGB star model as a function of its thermal pulses and compared the abundance yields of each thermal pulse with the abundance patterns of the sample stars to find the best match.

Considering elements Ba and heavier, the CEMP-sA stars’ patterns can be reproduced by only few thermal pulses of their AGB star companion, whereas CEMP-sB and CEMP-sC

stars require progressively more thermal pulses. This can be understood since the relative production of heavier to lighter neutron-capture elements takes longer, and CEMP-sC stars require larger amounts of the heaviest elements. This is consistent with the fact that lower thermal pulse numbers correspond to an earlier mass transfer event in the evolution of the AGB star compared to later ones.

In conclusion, the CEMP-sA stars are well-explained by the $1.3 M_{\odot}$, $[\text{Fe}/\text{H}] = -2.5$ model. Following some tests with higher mass models with a metallicity of $[\text{Fe}/\text{H}] = -2.2$, we speculate that the abundance patterns of some of the CEMP-sB and CEMP-sC stars could better be reproduced by models with masses larger than $1.3 M_{\odot}$ because we suspect these models to produce larger amounts of the heaviest elements. We find the abundance signature of HE 0414–0343 to have arisen from a $> 1.3 M_{\odot}$ mass AGB star in combination with a late-time mass transfer. Correspondingly, HE 0414–0343 is a CEMP-sC star. We speculate on the origin of the three classes of CEMP-s stars and suggest that the range of abundances are caused by a number of factors from variations in AGB mass, the timing of the mass transfer event, or from physics not currently included in the 1D calculations such as proton-ingestion at the tip of the AGB. Pre-enrichment due to chemical evolution could also play a role.

The Hobby-Eberly Telescope (HET) is a joint project of the University of Texas at Austin, the Pennsylvania State University, Stanford University, Ludwig-Maximilians-Universität München, and Georg-August-Universität Göttingen. The HET is named in honor of its principal benefactors, William P. Hobby and Robert E. Eberly. We are grateful to the Hobby-Eberly staff for their assistance in obtaining the data collected for this paper. We appreciate useful conversations with Christopher Waters and Harriet Dinerstein. J.K.H. acknowledges support for this work from NSF grants AST-0708245 and AST-0908978. A.F. acknowledges support from NSF grant AST-1255160 and the Silverman (1968) Family Career Development Professorship. J.K.H., A.F. and V.M.P. acknowledge partial support for this work from PHY 08-22648; Physics Frontier Center/Joint Institute for Nuclear Astrophysics (JINA) and PHY 14-30152; Physics Frontier Center/JINA Center for the Evolution of the Elements (JINA-CEE), awarded by the US National Science Foundation. This work was supported in part by NSF grant AST-1211585 to C.S. A.I.K. was supported through an Australian Research Council Future Fellowship (FT110100475).

REFERENCES

Abate, C., Pols, O. R., Karakas, A. I., & Izzard, R. 2015, A&A, in press

- Abia, C., Busso, M., Gallino, R., et al. 2001, *ApJ*, 559, 1117
- Aoki, W., Beers, T. C., Christlieb, N., Norris, J. E., Ryan, S. G., & Tsangarides, S. 2007, *ApJ*, 655, 492
- Arlandini, C., Käppeler, F., Wisshak, K., et al. 1999, *ApJ*, 525, 886
- Asplund, M., Grevesse, N., Sauval, A. J., & Scott, P. 2009, *ARA&A*, 47, 481
- Beers, T. C. & Christlieb, N. 2005, *ARA&A*, 43, 531
- Bernstein, R., Shectman, S. A., Gunnels, S. M., Mochnacki, S., & Athey, A. E. 2003, in *Society of Photo-Optical Instrumentation Engineers (SPIE) Conference Series*, ed. M. Iye & A. F. M. Moorwood, 1694
- Bisterzo, S., Gallino, R., Straniero, O., & Aoki, W. 2009, *Publications of the Astronomical Society of Australia*, 26, 314
- Bisterzo, S., Gallino, R., Straniero, O., Cristallo, S., Käppeler, F. 2011, *MNRAS*, 418, 284
- Bisterzo, S., Gallino, R., Straniero, O., Cristallo, S., Käppeler, F. 2012, *MNRAS*, 422, 849
- Bonačić Marinović, A., Lugaro, M., Reyniers, M., & van Winckel, H. 2007, *A&A*, 472, L1
- Brooke, J. S. A., Bernath, P. F., Schmidt, T. W., & Backsay, G. B. 2013, *J. Quant. Spec. Radiat. Transf.*, 124, 11
- Busso, M., Gallino, R., & Wasserburg, G. J. 1999, *ARA&A*, 37, 239
- Busso, M., Gallino R., Lambert, D. L., Travaglio, C., & Smith, V. V. 2001, *ApJ*, 557, 802
- Cassisi, S., Castellani, M., Caputo, F., & Castellani, V. 2004, *A&A*, 426, 641
- Castelli, F. & Kurucz, R. L. 2004, [arXiv:astro-ph/0405087](https://arxiv.org/abs/astro-ph/0405087)
- Cayrel, R., Depagne, E., Spite, M., Hill, V., Spite, F., François, P., Plez, B., Beers, T., Primas, F., Andersen, J., Barbuy, B., Bonifacio, P., Molaro, P., & Nordström, B. 2004, *A&A*, 416, 1117
- Christlieb, N., Bessell, M. S., Beers, T. C., Gustafsson, B., Korn, A., Barklem, P. S., Karlsson, T., Mizuno-Wiedner, M., & Rossi, S. 2002, *Nature*, 419, 904
- Cohen, J. G., Christlieb, N., Qian, Y.-Z., & Wasserburg, G. J. 2003, *ApJ*, 588, 1082

- Cristallo, S., Piersanti, L., Straniero, O., Gallino, R., Domínguez, I., Abia, C., Di Rico, G., Quintini, M., & Bisterzo, S. 2011, *ApJS*, 197, 17
- Cui, W. Y., Sivarani, T., & Christlieb, N. 2013, *A&A*, 558, A36
- De Smedt, K., Van Winckel, H., Karakas, A. I., et al. 2012, *A&A*, 541, A67
- Fishlock, C. K., Karakas, A. I., Lugaro, M. & Yong, D. 2014, *ApJ*, 797, 44
- Frebel, A. 2010, *Astronomische Nachrichten*, 331, 474
- Frebel, A., Aoki, W., Christlieb, N., Ando, H., Asplund, M., Barklem, P. S., Beers, T. C., Eriksson, K., Fechner, C., Fujimoto, M. Y., Honda, S., Kajino, T., Minezaki, T., Nomoto, K., Norris, J. E., Ryan, S. G., Takada-Hidai, M., Tsangarides, S., & Yoshii, Y. 2005, *Nature*, 434, 871
- Frebel, A., Christlieb, N., Norris, J. E., Beers, T. C., Bessell, M. S., Rhee, J., Fechner, C., Marsteller, B., Rossi, S., Thom, C., Wisotzki, L., & Reimers, D. 2006, *ApJ*, 652, 1585
- Frebel, A., Christlieb, N., Norris, J. E., Thom, C., Beers, T. C., & Rhee, J. 2007, *ApJ*, 660, L117
- Frebel, A. & Norris, J. E. 2013, *Metal-Poor Stars and the Chemical Enrichment of the Universe*, 55
- Frebel, A., Casey, A. R., Jacobson, H. R., & Yu, Q. 2013, *ApJ*, 769, 57
- Frischknecht, U., Hirschi, R., & Thielemann, F.-K. 2012, *A&A*, 538, L2
- Gallino, R., Arlandini, C., Busso, M., Lugaro, M., Travaglio, C., Straniero, O., Chieffi, A., & Limongi, M. 1998, *ApJ*, 497, 388
- Goriely, S., & Siess, L. 2005, *From Lithium to Uranium: Elemental Tracers of Early Cosmic Evolution*, 228, 451
- Green, E. M., Demarque, P., & King, C. R. 1984, *BAAS*, 16, 997
- Hansen, C. J., Bergemann, M., Cescutti, G., et al. 2013, *A&A*, 551, A57
- Herwig, F., Pignatari, M., Woodward, P. R., Porter, D. H., Rockefeller, G., Fryer, C. L., Bennett, M., & Hirschi, R. 2011, *ApJ*, 727, 89
- Hill, V., Plez, B., Cayrel, R., Nordström, T. B. B., Andersen, J., Spite, M., Spite, F., Barbuy, B., Bonifacio, P., Depagne, E., François, P., & Primas, F. 2002, *A&A*, 387, 560

- Hollek, J. K., Frebel, A., Roederer, I. U., Sneden, C., Shetrone, M., Beers, T. C., Kang, S.-j., & Thom, C. 2011, *ApJ*, 742, 54
- Jonsell, K., Barklem, P. S., Gustafsson, B., Christlieb, N., Hill, V., Beers, T. C., & Holmberg, J. 2006, *A&A*, 451, 651
- Karakas, A. I. 2010, *MNRAS*, 403, 1413
- Karakas, A. I., & Lattanzio, J. C. 2014, *PASA*, 31, 30
- Karakas, A. I., Campbell, S. W., & Stancliffe, R. J. 2010, *ApJ*, 713, 374
- Keller, S. C., Bessell, M. S., Frebel, A., et al. 2014, *Nature*, 506, 463
- Kelson, D. D. 2003, *PASP*, 115, 688
- Kim, Y.-C., Demarque, P., Yi, S. K., & Alexander, D. R. 2002, *ApJS*, 143, 499
- Kurucz, R. L. 1998, in *IAU Symposium*, Vol. 189, *Fundamental Stellar Properties*, ed. T. R. Bedding, A. J. Booth, & J. Davis, 217
- Lawler, J. E., Guzman, A., Wood, M. P., Sneden, C., & Cowan, J. J. 2013, *ApJS*, 205, 11
- Lucatello, S., Tsangarides, S., Beers, T. C., Carretta, E., Gratton, R. G., & Ryan, S. G. 2005, *ApJ*, 625, 825
- Lugaro, M., Karakas, A. I., Stancliffe, R. J., & Rijs, C. 2012, *ApJ*, 747, 2
- Mashonkina, L., Ryabtsev, A., & Frebel, A. 2012, *A&A*, 540, A98
- Masseron, T., Johnson, J. A., Plez, B., van Eck, S., Primas, F., Goriely, S., & Jorissen, A. 2010, *A&A*, 509, 93
- Moore, C. E., Minnaert, M. G. J., & Houtgast, J. 1966, *The solar spectrum 2935 Å to 8770 Å*
- Pignatari, M., Gallino, R., Meynet, G., Hirschi, R., Herwig, F., & Wiescher, M. 2008, *ApJ*, 687, L95
- Placco, V. M., Frebel, A., Beers, T. C., Karakas, A. I., Kennedy, C. R., Rossi, S., Christlieb, N., & Stancliffe, R. J. 2013, *ApJ*, 770, 104
- Placco, V. M., Frebel, A., Beers, T. C., & Stancliffe, R. J. 2014, *ApJ*, 797, 21

- Ram, R. S., Brooke, J. S. A., Bernath, P. F., Sneden, C., & Lucatello, S. 2013, ApJS, Submitted
- Roederer, I. U., Frebel, A., Shetrone, M. D., Allende Prieto, C., Rhee, J., Gallino, R., Bisterzo, S., Sneden, C., Beers, T. C., & Cowan, J. J. 2008, ApJ, 679, 1549
- Simmerer, J., Sneden, C., Cowan, J. J., Collier, J., Woolf, V. M., & Lawler, J. E. 2004, ApJ, 617, 1091
- Sivarani, T., Beers, T. C., Bonifacio, P., et al. 2006, A&A, 459, 125
- Smith, V. V., & Lambert, D. L. 1990, ApJS, 72, 387
- Sneden, C., Cowan, J. J., Ivans, I. I., Fuller, G. M., Burles, S., Beers, T. C., & Lawler, J. E. 2000, ApJ, 533, L139
- Sneden, C., Cowan, J. J., Lawler, J. E., Ivans, I. I., Burles, S., Beers, T. C., Primas, F., Hill, V., Truran, J. W., Fuller, G. M., Pfeiffer, B., & Kratz, K.-L. 2003, ApJ, 591, 936
- Sneden, C. A. 1973, PhD thesis, The University of Texas at Austin
- Sobeck, J. S., Kraft, R. P., Sneden, C., Preston, G. W., Cowan, J. J., Smith, G. H., Thompson, I. B., Shectman, S. A., & Burley, G. S. 2011, AJ, 141, 175
- Stancliffe, R. J. & Glebeek, E. 2008, MNRAS, 389, 1828
- Starkenburg, E., Shetrone, M. D., McConnachie, A. W., & Venn, K. A. 2014, MNRAS, 441, 1217
- Travaglio, C., Gallino, R., Arnone, E., Cowan, J., Jordan, F., & Sneden, C. 2004, ApJ, 601, 864
- Tull, R. G. 1998, in Society of Photo-Optical Instrumentation Engineers (SPIE) Conference, Vol. 3355, Optical Astronomical Instrumentation, ed. S. D’Odorico, 387
- Vassiliadis, E. & Wood, P. R. 1993, ApJ, 413, 641
- Waters, C. Z. & Hollek, J. K. 2013, PASP, 125, 1164
- Wood, M. P., Lawler, J. E., Sneden, C., & Cowan, J. J. 2013, ApJS, 208, 27

Table 2—Continued

Species	λ [Å]	χ [eV]	log gf	W mÅ	log $\epsilon(X)$
Nd II	5319.81	0.55	−0.14	Synth	0.73
Sm II	4318.93	0.28	−0.25	Synth	0.04
Sm II	4434.32	0.38	−0.07	Synth	0.17
Sm II	4519.63	0.54	−0.35	Synth	0.21
Eu II	6645.06	1.38	0.20	Synth	−0.49
Dy II	4449.70	0.00	−1.03	Synth	0.45
Er I	3682.70	0.89	−0.38	Synth	0.24
Yb II	3694.19	0.00	−0.82	Synth	0.03
Pb I	3683.46	0.97	−0.46	Synth	1.97
Pb I	4057.81	1.32	−0.22	Synth	2.11

^aThe C^{12}/C^{13} value is a ratio and not a log $\epsilon(X)$ value.

Table 3. Elemental Abundances of HE 0414–0343

Element	$\log \epsilon(X)$	σ	[X/Fe]	n	$\log \epsilon(X)_{\odot}$	Method
C (C ₂)	7.63	0.30	1.44	1	8.43	Synth
Mg I	5.82	0.12	0.46	5	7.60	EW
Ca I	4.57	0.13	0.47	14	6.34	EW
Sc II	1.14	0.12	0.23	10	3.15	EW
Ti I	2.99	0.17	0.28	30	4.95	EW
Ti II	3.14	0.18	0.43	24	4.95	EW
Cr I	3.26	0.12	−0.14	10	5.64	EW
Mn I	2.75	0.12	−0.44	2	5.43	Synth
Fe I	5.26	0.12	...	88	7.50	EW
Fe II	5.26	0.13	...	18	7.50	EW
Ni I	3.97	0.20	−0.01	15	6.22	EW
Zn I	2.38	0.20	0.06	1	4.56	Synth
Sr II	1.11	0.30	0.48	1	2.87	Synth
Y II	0.17	0.12	0.20	2	2.21	Synth
Zr II	0.85	0.12	0.51	3	2.58	Synth
Ba II	1.81	0.12	1.87	3	2.18	Synth
La II	0.46	0.12	1.60	5	1.10	Synth
Ce II	0.74	0.12	1.40	3	1.58	Synth
Pr II	−0.17	0.30	1.35	1	0.72	Synth
Nd II	0.81	0.12	1.63	3	1.42	Synth
Sm II	0.14	0.12	1.42	3	0.96	Synth
Eu II	−0.49	0.30	1.23	1	0.52	Synth
Dy II	0.45	0.30	1.59	1	1.10	Synth
Er I	0.24	0.30	1.56	1	0.92	Synth
Yb II	0.03	0.30	1.43	1	0.84	Synth
Pb I	2.04	0.12	2.53	2	1.75	Synth

Table 4. Abundance Uncertainties

Element	Random Unc.	ΔT_{eff} +150 K	$\Delta \log g$ +0.5 dex	Δv_{micr} +0.3 km s ^{−1}	Total ^a Unc.
C (C ₂)	0.30	0.25	−0.10	0.00	0.40
Mg I	0.12	0.12	−0.12	−0.09	0.23
Ca I	0.13	0.12	−0.05	−0.07	0.20
Sc II	0.12	0.06	0.16	−0.05	0.21
Ti I	0.17	0.21	−0.07	−0.05	0.28
Ti II	0.18	0.05	0.15	−0.09	0.26
Cr I	0.12	0.19	−0.07	−0.05	0.24
Mn I	0.12	0.16	−0.06	−0.04	0.21
Fe I	0.12	0.17	−0.06	−0.08	0.23
Fe II	0.13	0.00	0.17	−0.04	0.22
Ni I	0.20	0.14	−0.04	−0.02	0.25
Ba II	0.12	0.10	0.10	−0.25	0.31

^aObtained by adding all uncertainties in quadrature.

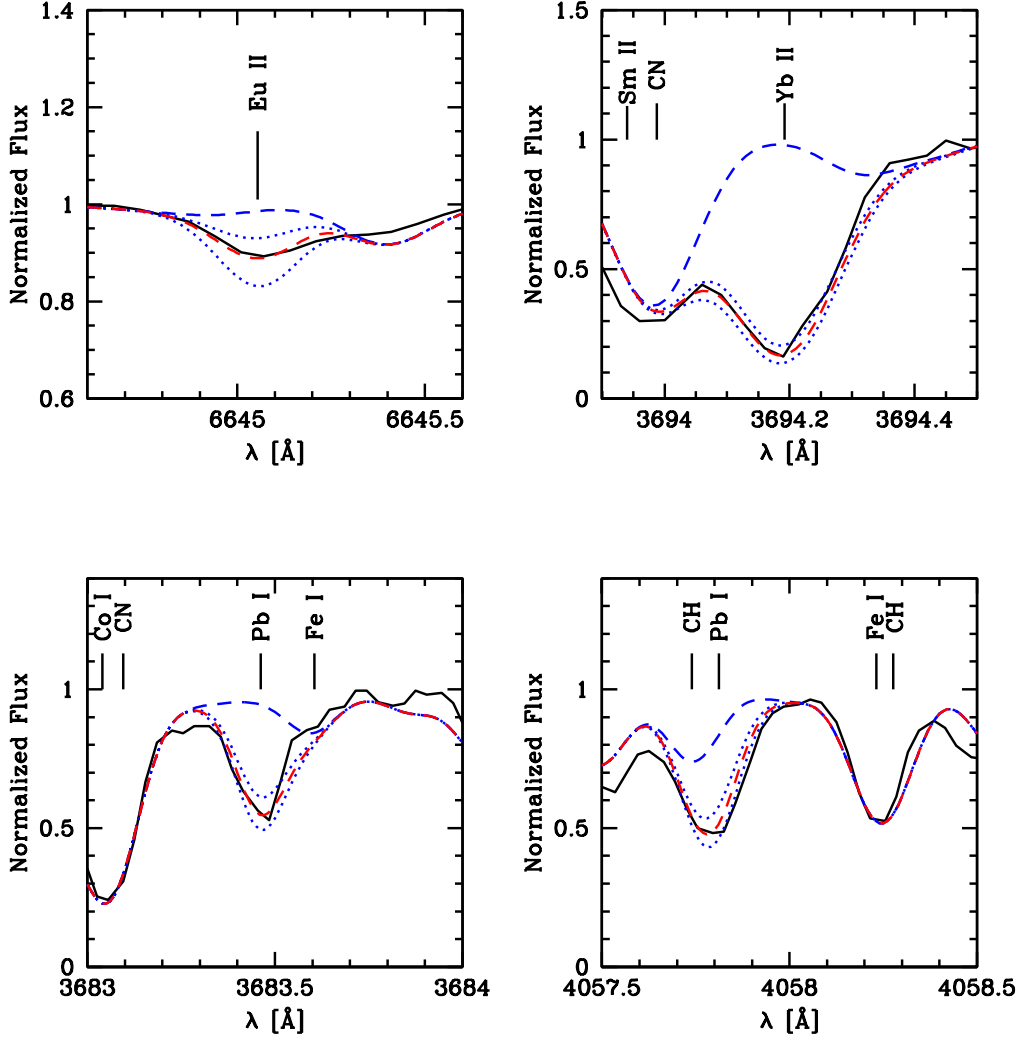


Fig. 6.— Top: Eu feature at $\lambda 6645$ Å (left panel) in the HE 0414–0343 spectrum (solid black line), along with the best-fit abundance (red dashed line), Eu abundances changed a factor of two above and below the best fit synthetic abundance (blue dotted line) of $[\text{Eu}/\text{Fe}] = 1.23$, and a synthetic spectrum for which no Eu is present (blue dashed line). The Yb feature located at 3694 Å (right panel) is plotted in the same way as Eu and yields a $[\text{Yb}/\text{Fe}]$ ratio of 1.43. Bottom: Pb features at 3683 Å (left panel) and 4057 Å (right panel) in the HE 0414–0343 spectrum (solid black line), along with the best fit abundance (red dashed line), Pb abundances changed a factor of two above and below the best fit synthetic abundance (blue dotted line), and a synthetic spectrum for which no Pb is present (blue dashed line). The $\lambda 3683$ and $\lambda 4057$ lines yield $[\text{Pb}/\text{Fe}]$ abundance ratios of 2.53 and 2.60, respectively.

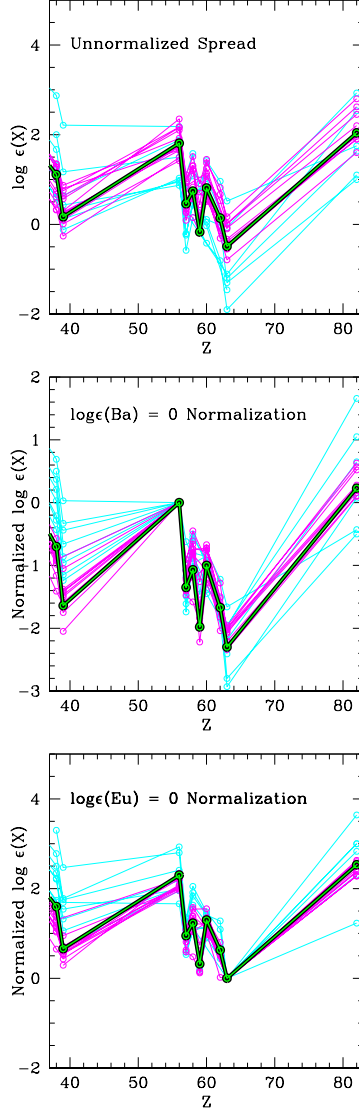


Fig. 7.— $\log \epsilon(X)$ abundances plotted against atomic number, Z , (top), $\log \epsilon(X)$ values that have been normalized to $\log \epsilon(\text{Ba}) = 0.0$ (middle), and $\log \epsilon(\text{Eu}) = 0.0$ (bottom) of selected neutron-capture elements. These normalization values were chosen because a majority of the Ba and Eu abundances, respectively, were close to those values (but the values are arbitrary). Color coding according to the traditional “s” and “r/s” classification. Cyan corresponds to CEMP-s stars, magenta to CEMP-r/s stars, and green to HE 0414–0343.

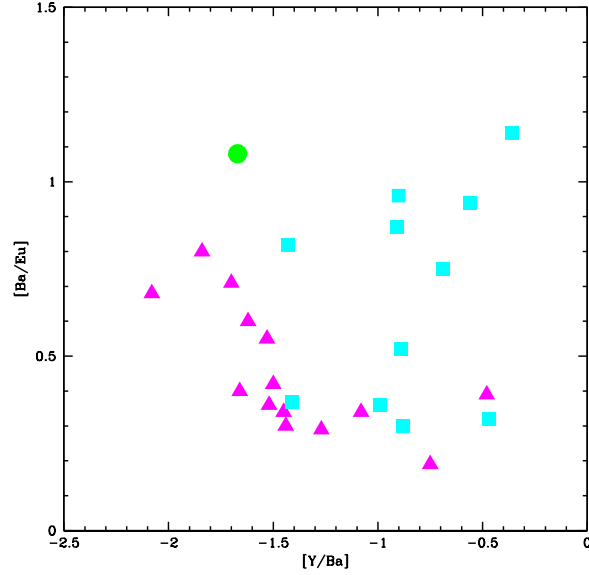


Fig. 8.— $[Ba/Eu]$ abundance ratio for the entire sample plotted against $[Y/Ba]$. It depicts the traditional ($[Ba/Eu]$) against our proposed ($[Y/Ba]$) classification of CEMP-s and CEMP-r/s stars. The distinction between CEMP-s and CEMP-r/s stars has so far been made at $[Ba/Eu] = 0.5$. As can be seen, it does not well separate the stars according to the corresponding CEMP-s and CEMP-r/s classes. $[Y/Ba]$ provides a better way to group and classify the stars. Cyan squares correspond to stars traditionally defined as CEMP-s, magenta triangles to stars defined as CEMP-r/s

. The green filled circle corresponds to HE 0414–0343.

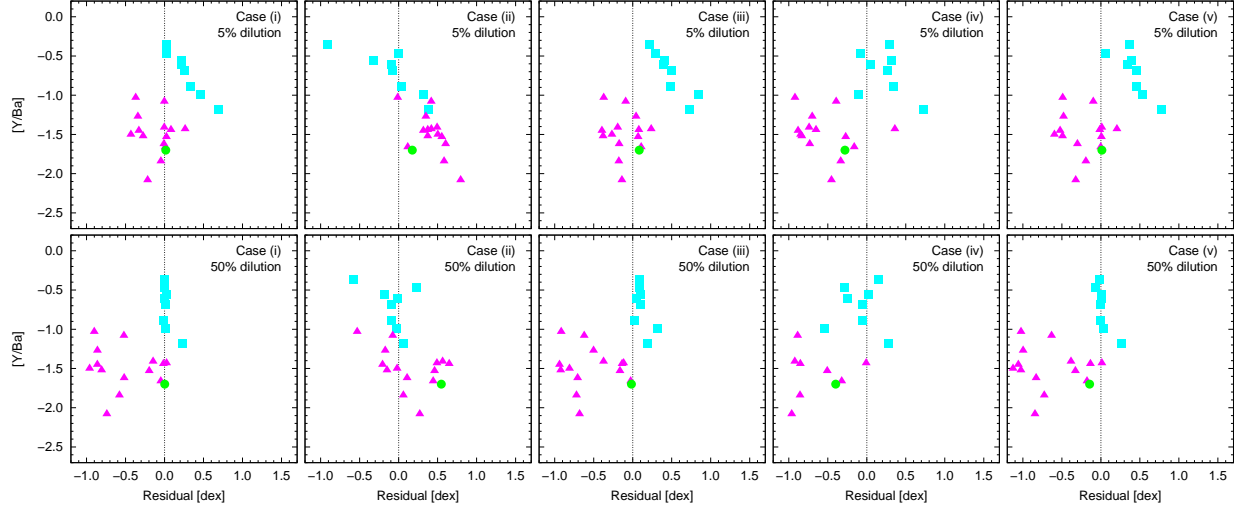


Fig. 9.— $[Y/Ba]$ ratio plotted against the five cases of residuals obtained from comparing the s-process nucleosynthesis results of a $[Fe/H] = -2.5$ AGB star with the abundances of star traditionally defined as CEMP-s stars (cyan squares), CEMP-r/s stars (magenta triangles), and HE 0414–0343 (green circle). The top row of panels depicts the 5% dilution case, the bottom panels the 50% dilution case. See text for discussion.

Table 5. CEMP-sA,-sB,-sC classification scheme

Definition		Abbreviation
$[\text{Ba}/\text{Fe}] > 1.0$ and $-0.9 < [\text{Y}/\text{Ba}] < -0.3$		CEMP-sA
$[\text{Ba}/\text{Fe}] > 1.0$ and $-1.5 < [\text{Y}/\text{Ba}] < -0.9$		CEMP-sB
$[\text{Ba}/\text{Fe}] > 1.0$ and $[\text{Y}/\text{Ba}] < -1.5$		CEMP-sC
$[\text{Ba}/\text{Fe}] < 0.0$		CEMP-no ^a

Star	$[\text{Y}/\text{Ba}]$	Classification
CS 22898–027	–1.52	CEMP-sC
CS 22942–019	–0.36	CEMP-sA
CS 22947–187	–0.99	CEMP-sB
CS 22948–027	–1.08	CEMP-sB
CS 22964–161	–0.89	CEMP-sA
CS 29497–030	–1.27	CEMP-sB
CS 29497–034	–0.75	CEMP-sA
CS 29526–110	–0.48	CEMP-sA
CS 31062–012	–1.41	CEMP-sB
CS 31062–050	–2.08	CEMP-sC
HD 196944	–0.56	CEMP-sA
HE 0024–2523	–0.47	CEMP-sA
HE 0058–0244	–1.44	CEMP-sB
HE 0202–2204	–0.91	CEMP-sB
HE 0338–3945	–1.50	CEMP-sB
HE 0414–0343	–1.70	CEMP-sC
HE 1031–0020	–0.88	CEMP-sA
HE 1105+0027	–1.62	CEMP-sC
HE 1135+0139	–0.69	CEMP-sA
HE 1405–0822	–1.66	CEMP-sC
HE 1509–0806	–0.90	CEMP-sA
HE 2138–3336	–1.43	CEMP-sB
HE 2148–1247	–1.45	CEMP-sB
HE 2258–6358	–1.53	CEMP-sC
LP 62–544	–1.84	CEMP-sC

Note. — All stars have $[\text{C}/\text{Fe}] > 0.7$.

^aCarbon-enhanced metal-poor stars with normal neutron-capture element abundances (CEMP-no; [Beers & Christlieb 2005](#)) stars are not part of the classification CEMP-sA-C scheme. We include it here for completeness.

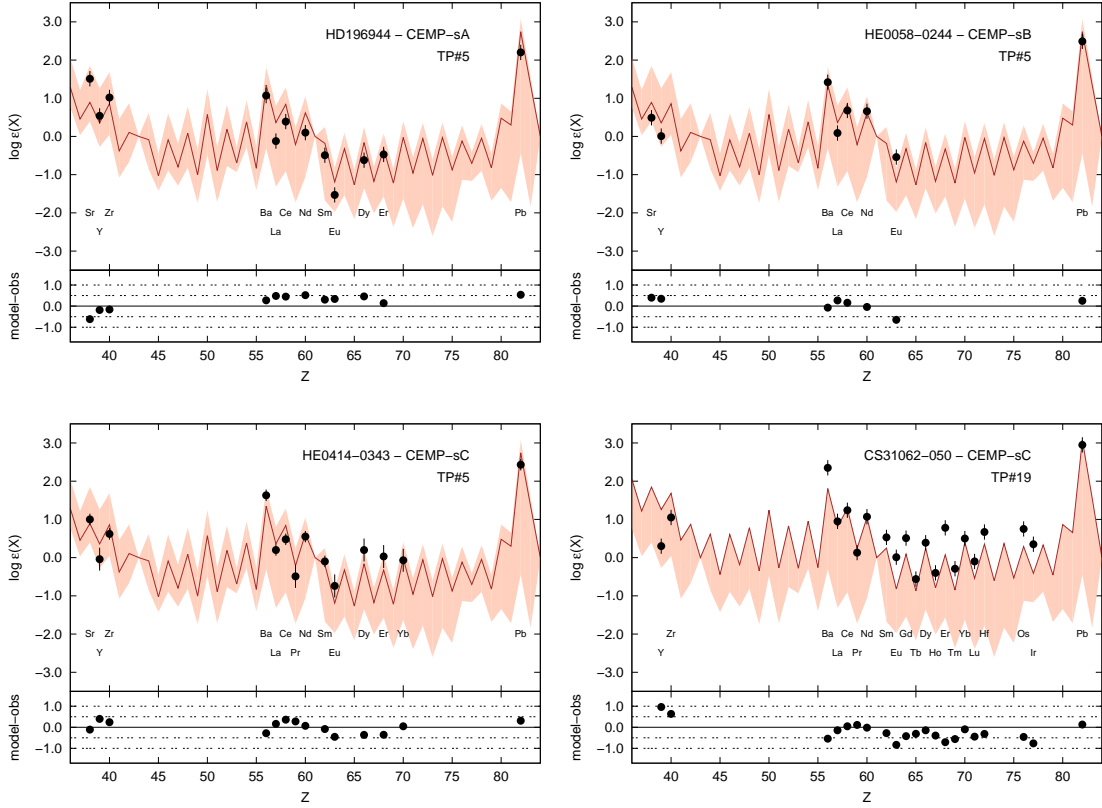


Fig. 10.— $\log \epsilon(X)$ values plotted against atomic number for four stars, including our program star, HE 0414–0343. In the upper panels, the black dots represent the stellar abundances, with bars showing uncertainties. The red line belongs to the best thermal pulse abundance distribution of our low-metallicity AGB model (for case v), and the peach shaded region corresponds to the range of abundance yields accumulating over each thermal pulse until thermal pulse 19. The bottom-most part of the peach section corresponds to the initial abundances at the start of the AGB phase in the model and the top-most part corresponds to the final abundance yields. In the bottom panels, the black dots represent the difference between the best thermal pulse distribution and the observed abundances. In the upper right corner of each plot, we show the star name, its classification, and which thermal pulse number corresponds to the best match. We have included a star from each classification as well as HE 0414–0343. The error bars included are the standard errors (see Table 3).

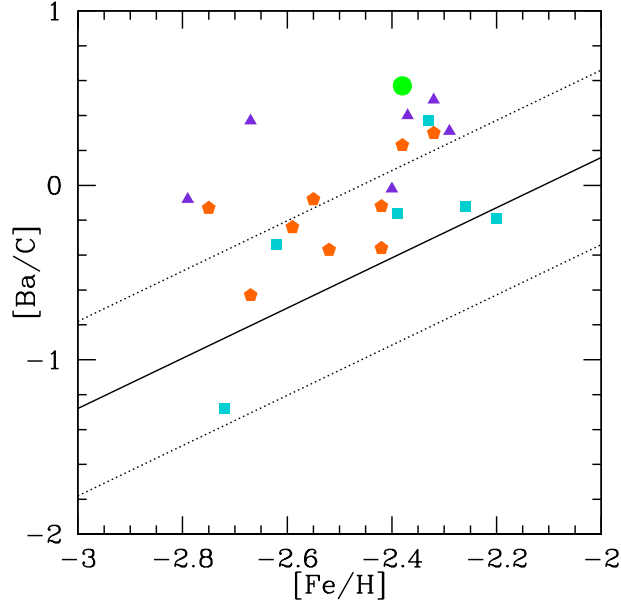


Fig. 11.— $[\text{Ba}/\text{C}]$ abundance ratio plotted as a function of $[\text{Fe}/\text{H}]$ of HE 0414–0343 and the entire literature sample. The green circle corresponds to HE 0414–0343, the turquoise squares represent the CEMP-sA stars, the orange pentagons correspond to the CEMP-sB stars, and the purple triangles correspond to the CEMP-sC stars. The solid black line corresponds to the relation that would be expected between $[\text{Ba}/\text{C}]$ and $[\text{Fe}/\text{H}]$ if the main neutron source for the s-process is C, empirically adopted from Figure 5 of [Masseron et al. \(2010\)](#). The black dotted lines represent the area on the plot where the majority of the CEMP-s stars resided in Figure 5 of [Masseron et al. \(2010\)](#) and correspond to the shaded region in the upper panel of their Figure 7.

- A. Results of the comparison of Abundance Patterns of CEMP-sA Sample Stars with the best matched thermal pulse abundance distributions.

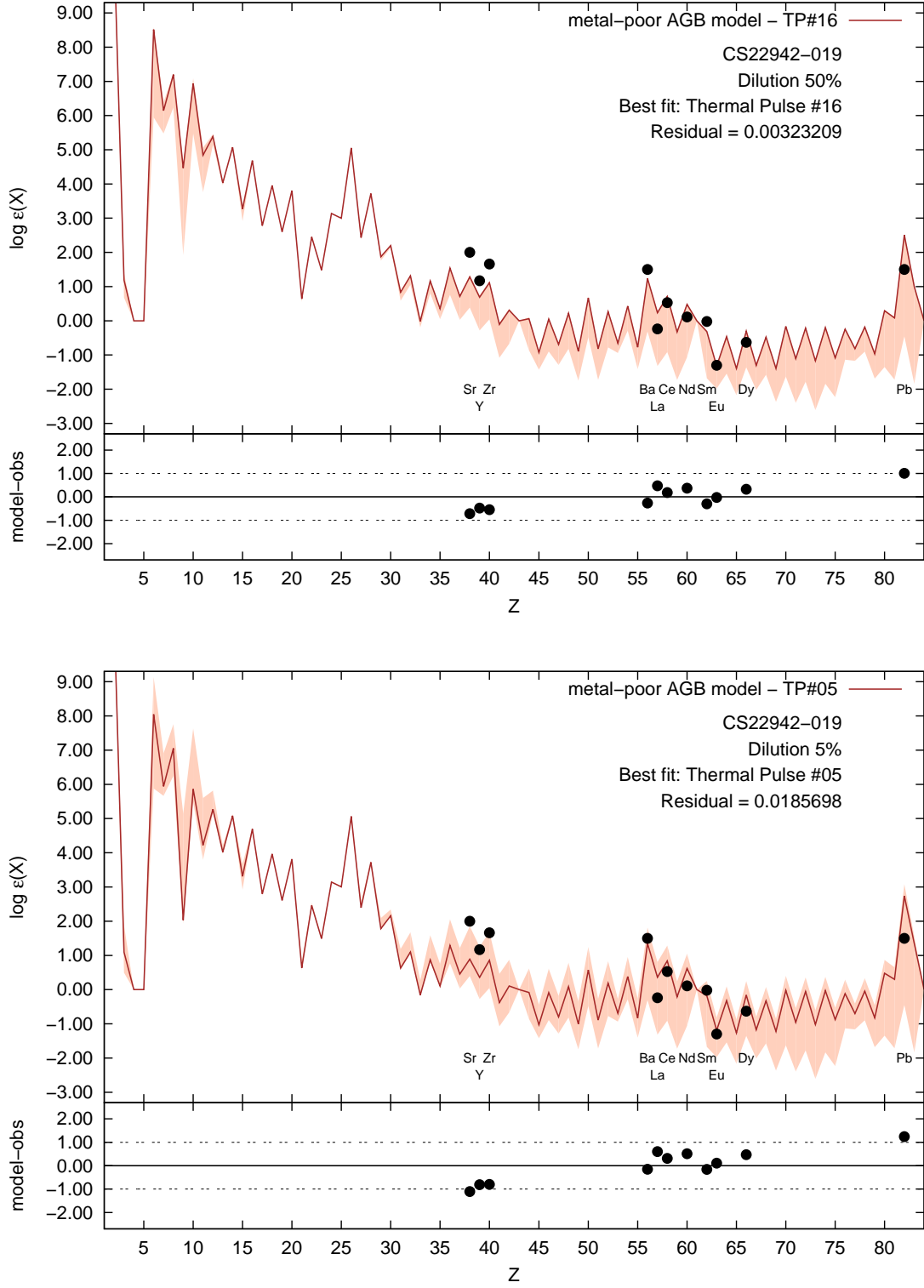


Fig. 12.— Best Fit Model Abundance Comparison of CS 22942–019, 50 Percent Dilution (upper panel), and 5 Percent Dilution (lower panel).

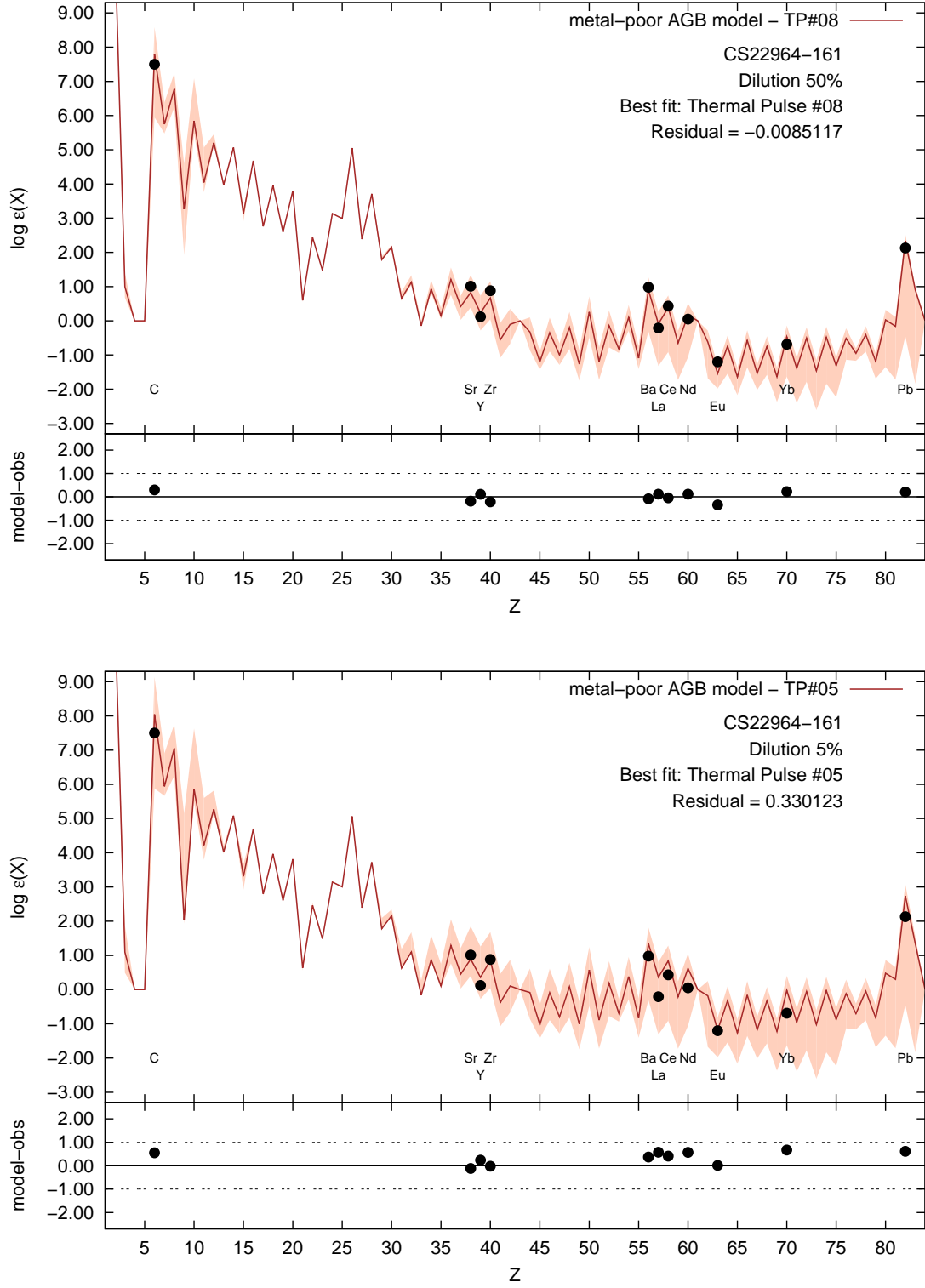


Fig. 13.— Best Fit Model Abundance Comparison of CS 22964-161, 50 Percent Dilution (upper panel), and 5 Percent Dilution (lower panel).

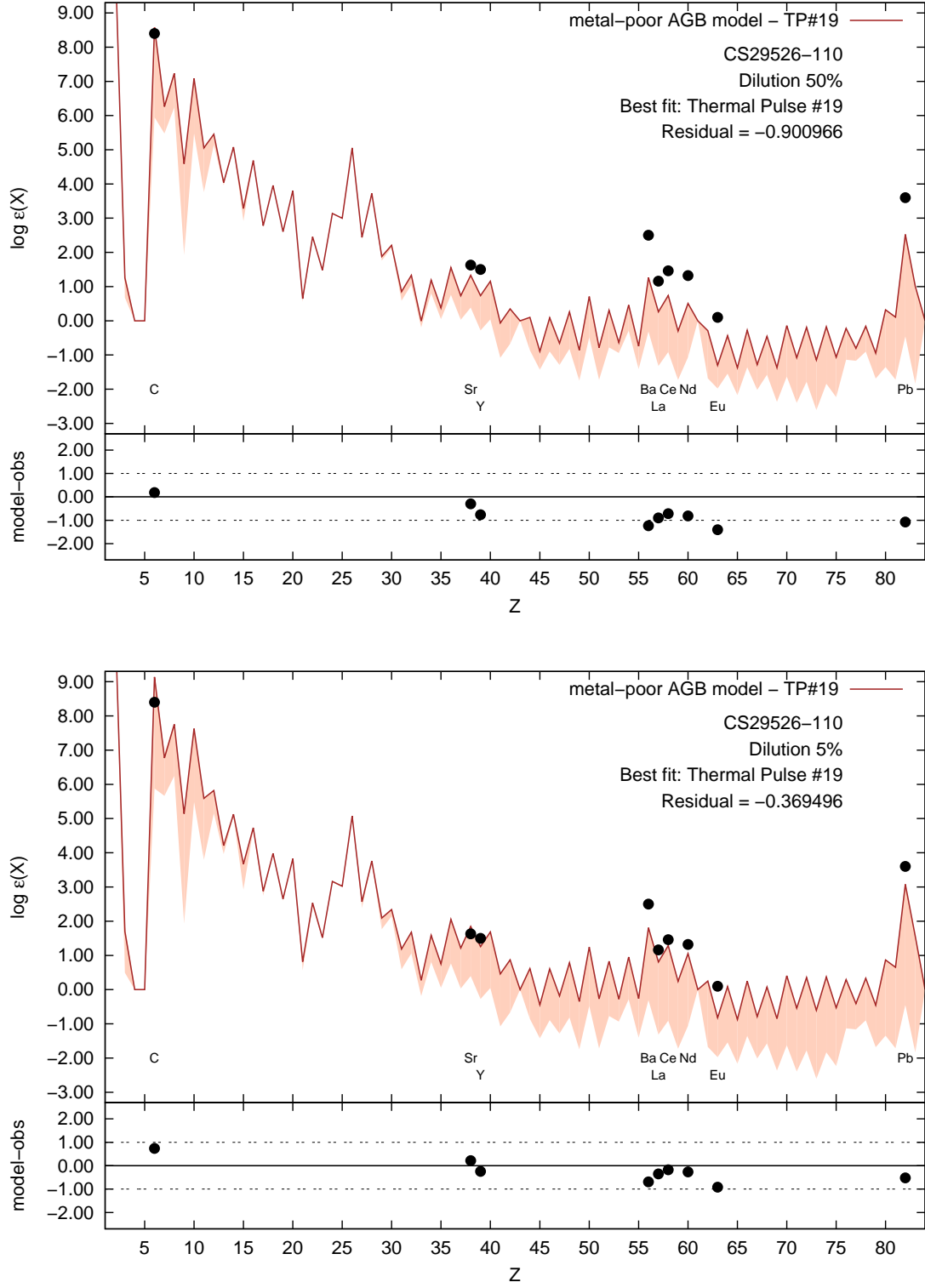


Fig. 14.— Best Fit Model Abundance Comparison of CS 29526–110, 50 Percent Dilution (upper panel), and 5 Percent Dilution (lower panel).

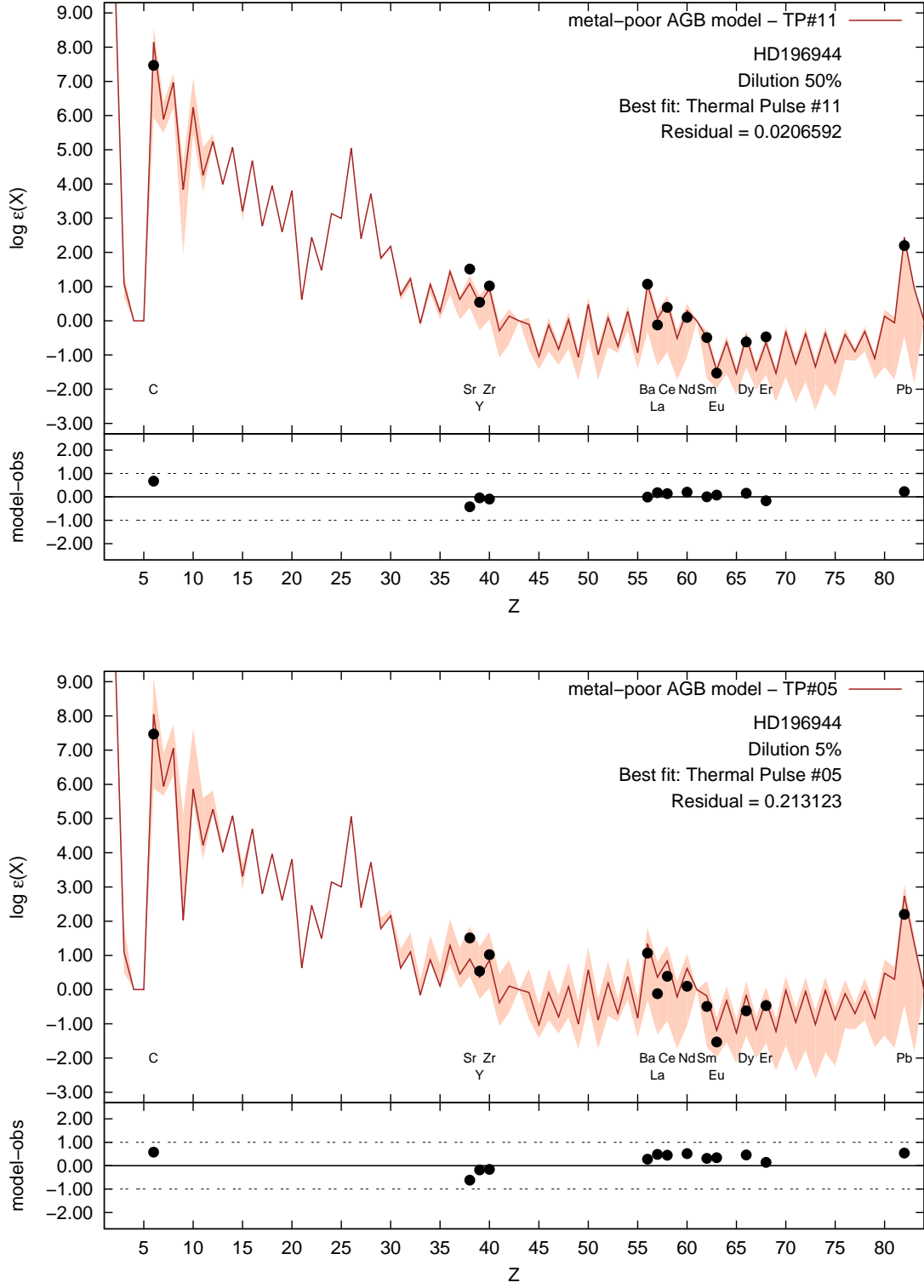


Fig. 15.— Best Fit Model Abundance Comparison of HD 196944, 50 Percent Dilution (upper panel), and 5 Percent Dilution (lower panel).

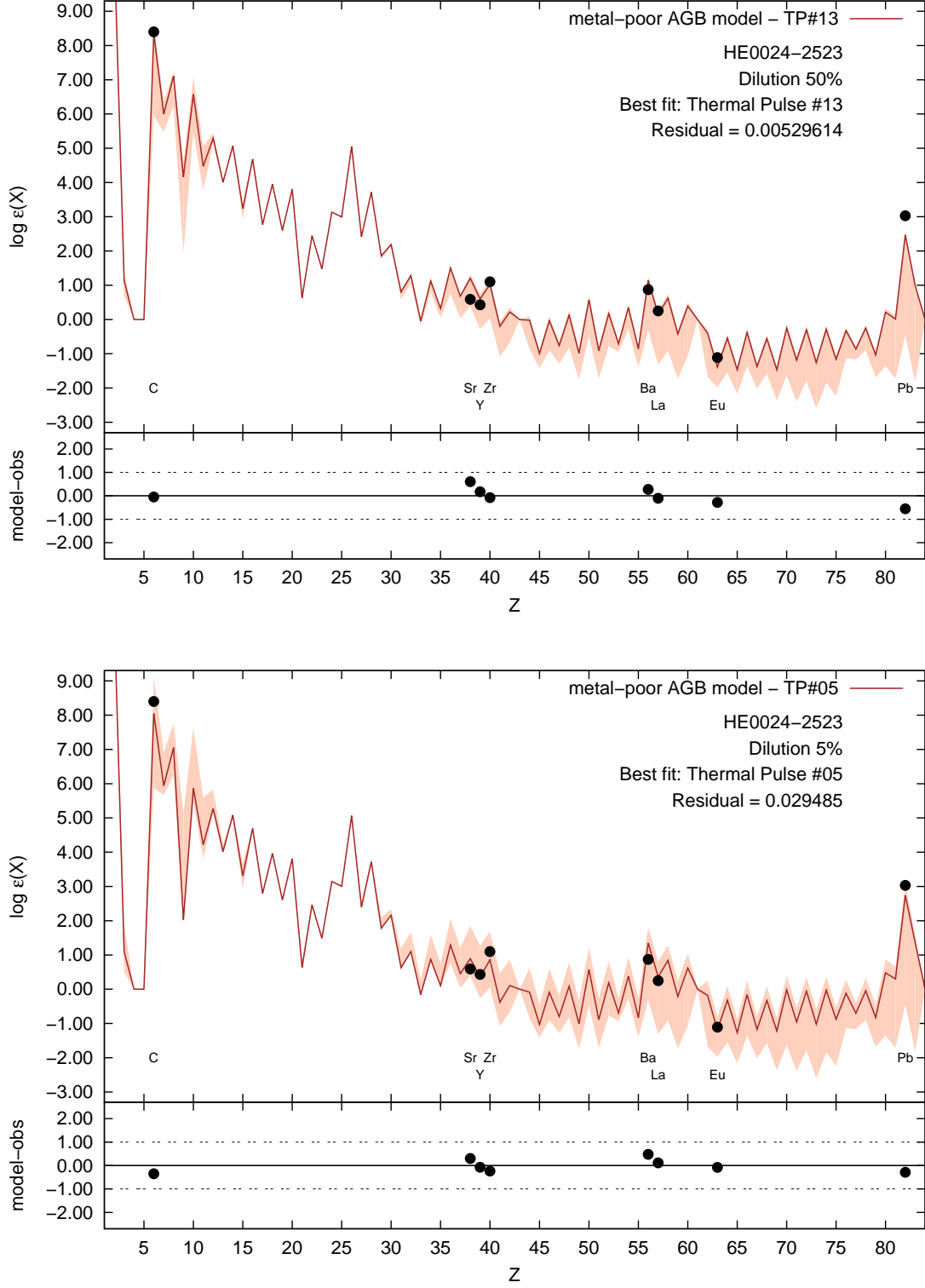


Fig. 16.— Best Fit Model Abundance Comparison of HE 0024-2523, 50 Percent Dilution (upper panel), and 5 Percent Dilution (lower panel).

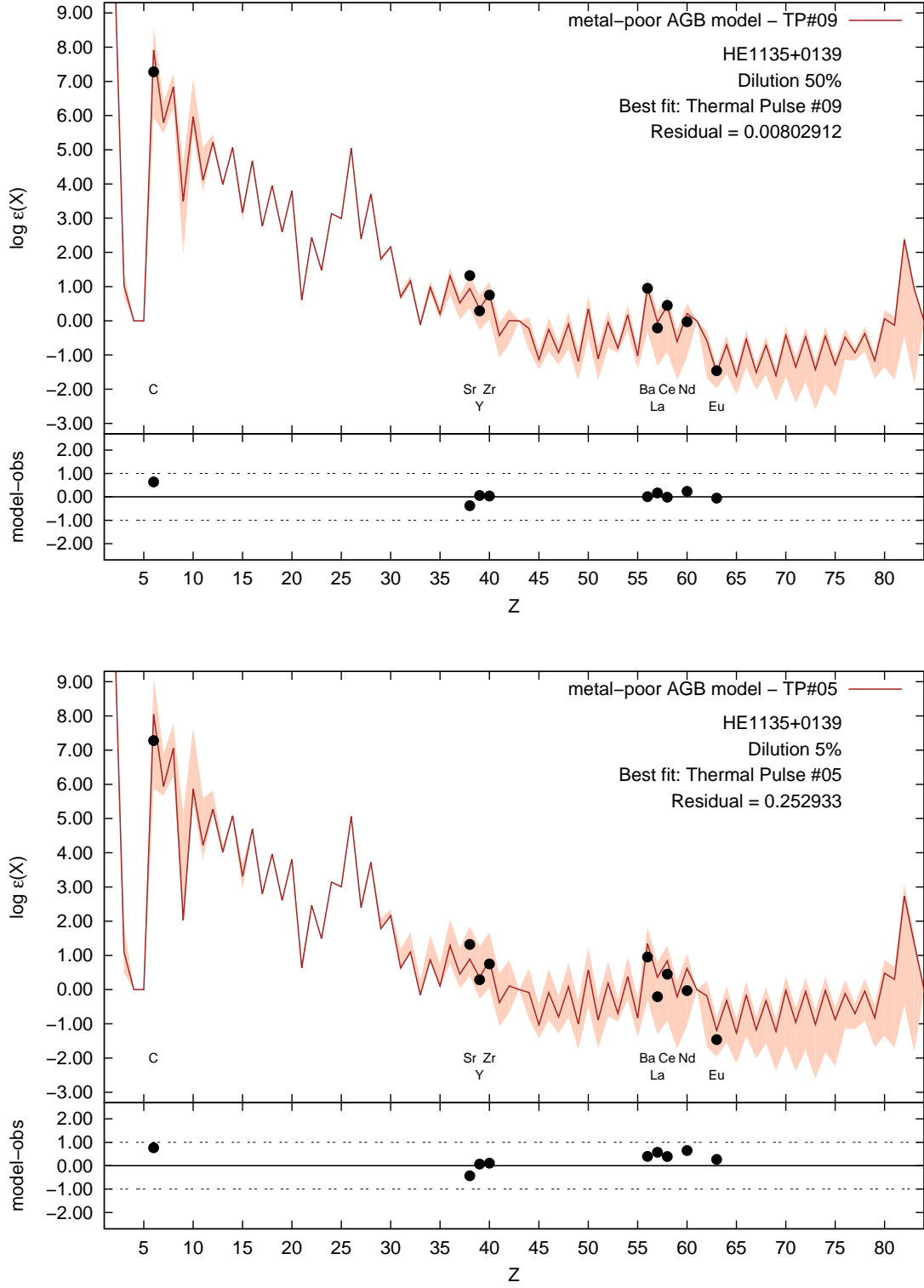


Fig. 17.— Best Fit Model Abundance Comparison of HE 1135+0139, 50 Percent Dilution (upper panel), and 5 Percent Dilution (lower panel).

B. Results of the comparison of Abundance Patterns of CEMP-sB Sample Stars with the best matched thermal pulse abundance distributions.

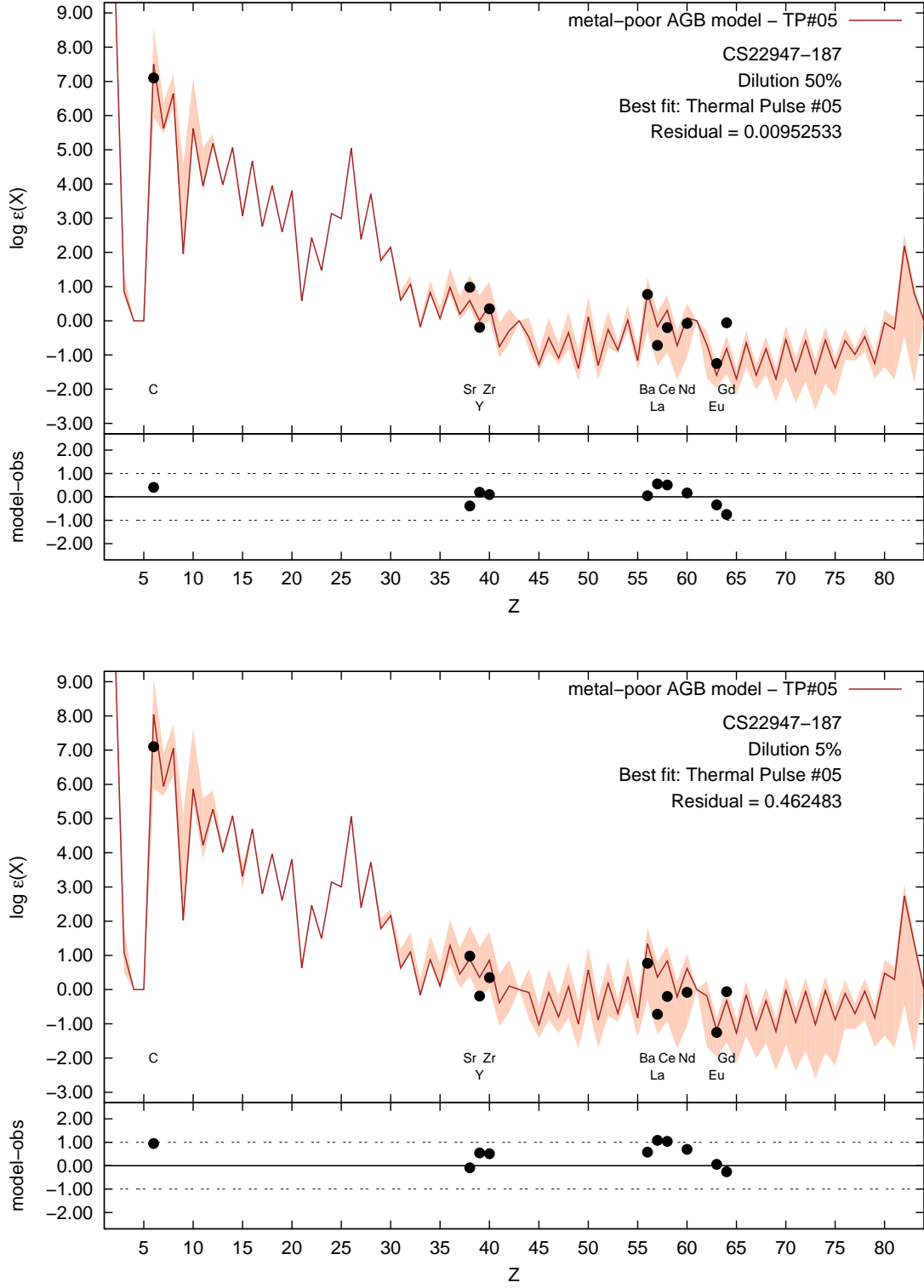


Fig. 18.— Best Fit Model Abundance Comparison of CS 22947–187, 50 Percent Dilution (upper panel), and 5 Percent Dilution (lower panel).

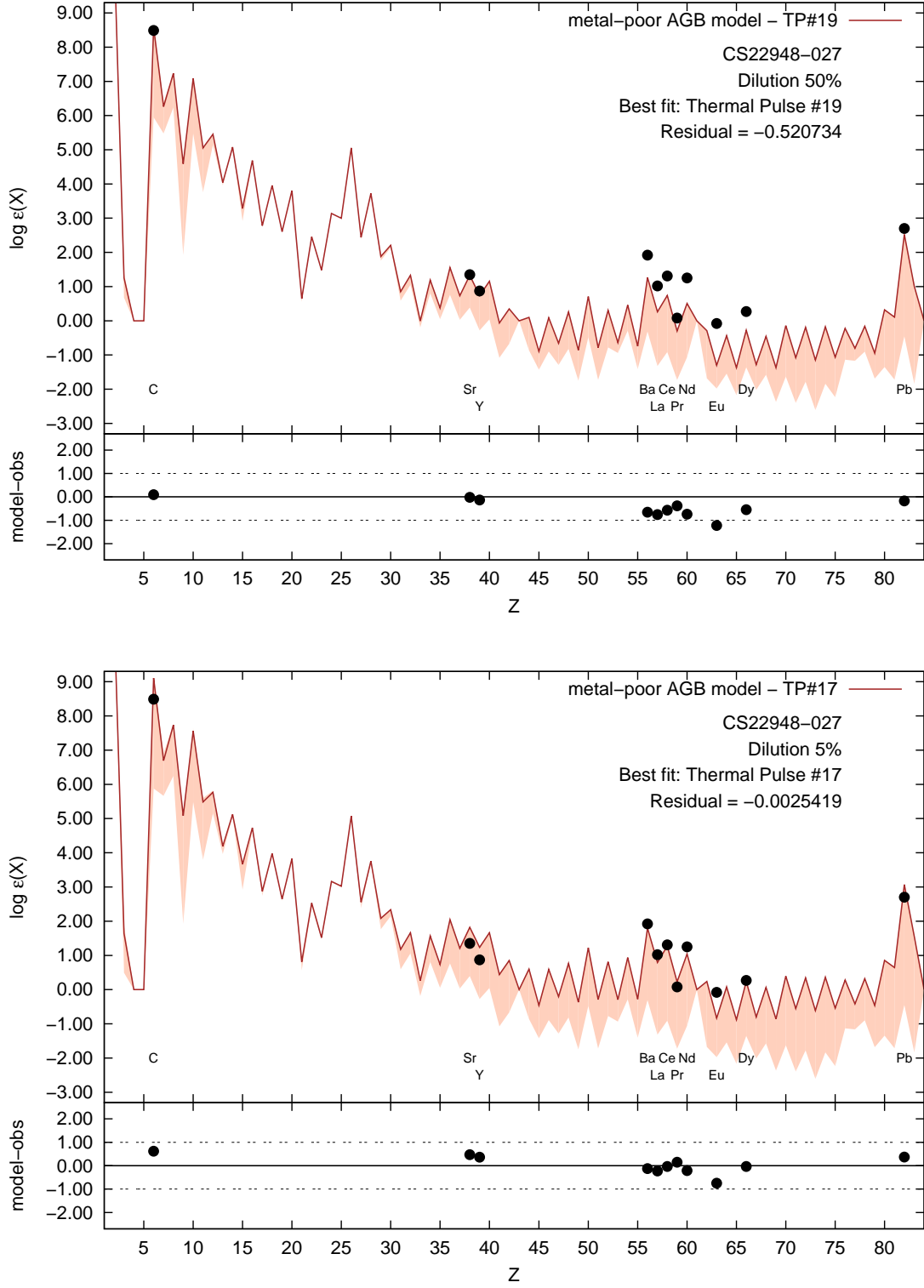


Fig. 19.— Best Fit Model Abundance Comparison of CS 22948–027, 50 Percent Dilution (upper panel), and 5 Percent Dilution (lower panel).

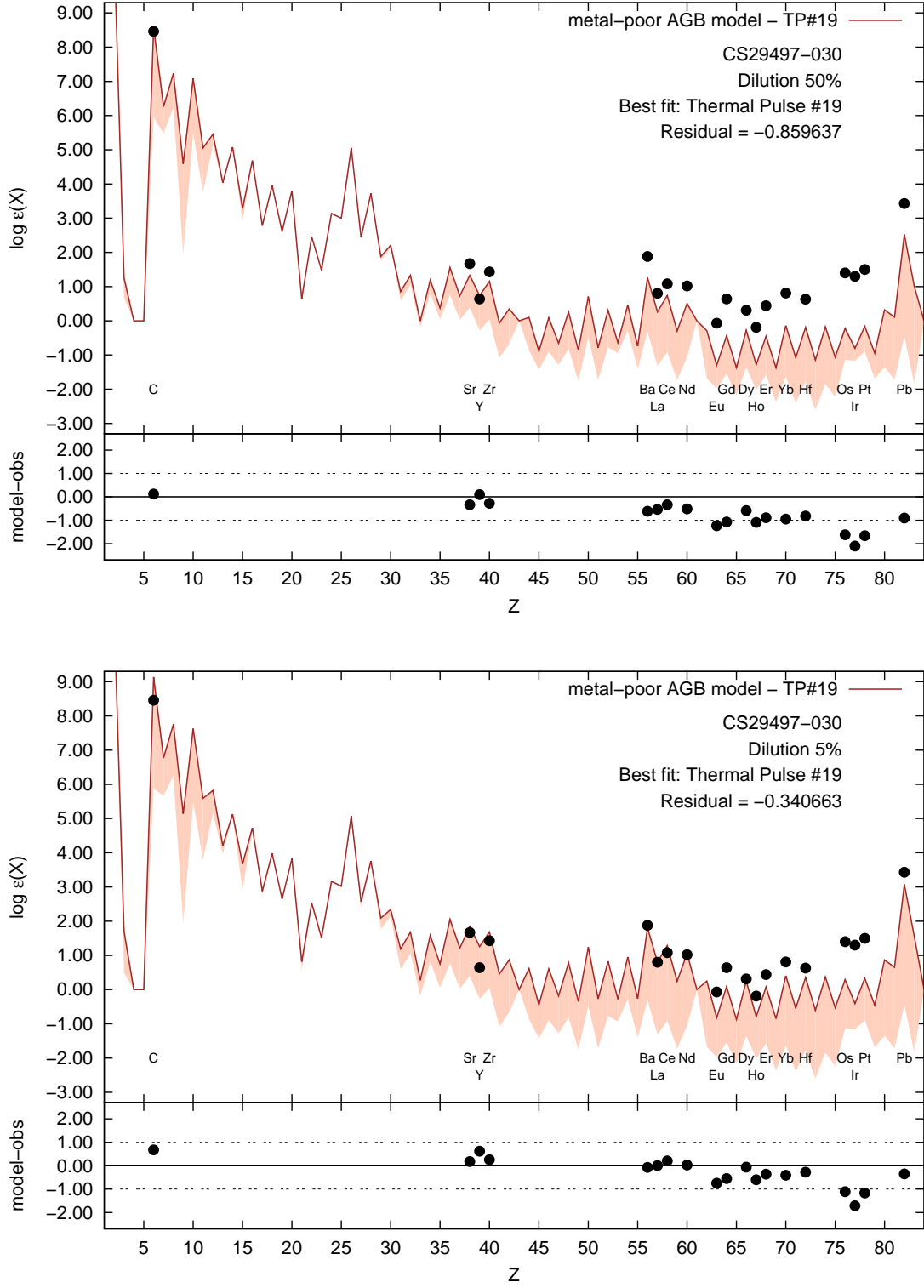


Fig. 20.— Best Fit Model Abundance Comparison of CS 29497-030, 50 Percent Dilution (upper panel), and 5 Percent Dilution (lower panel).

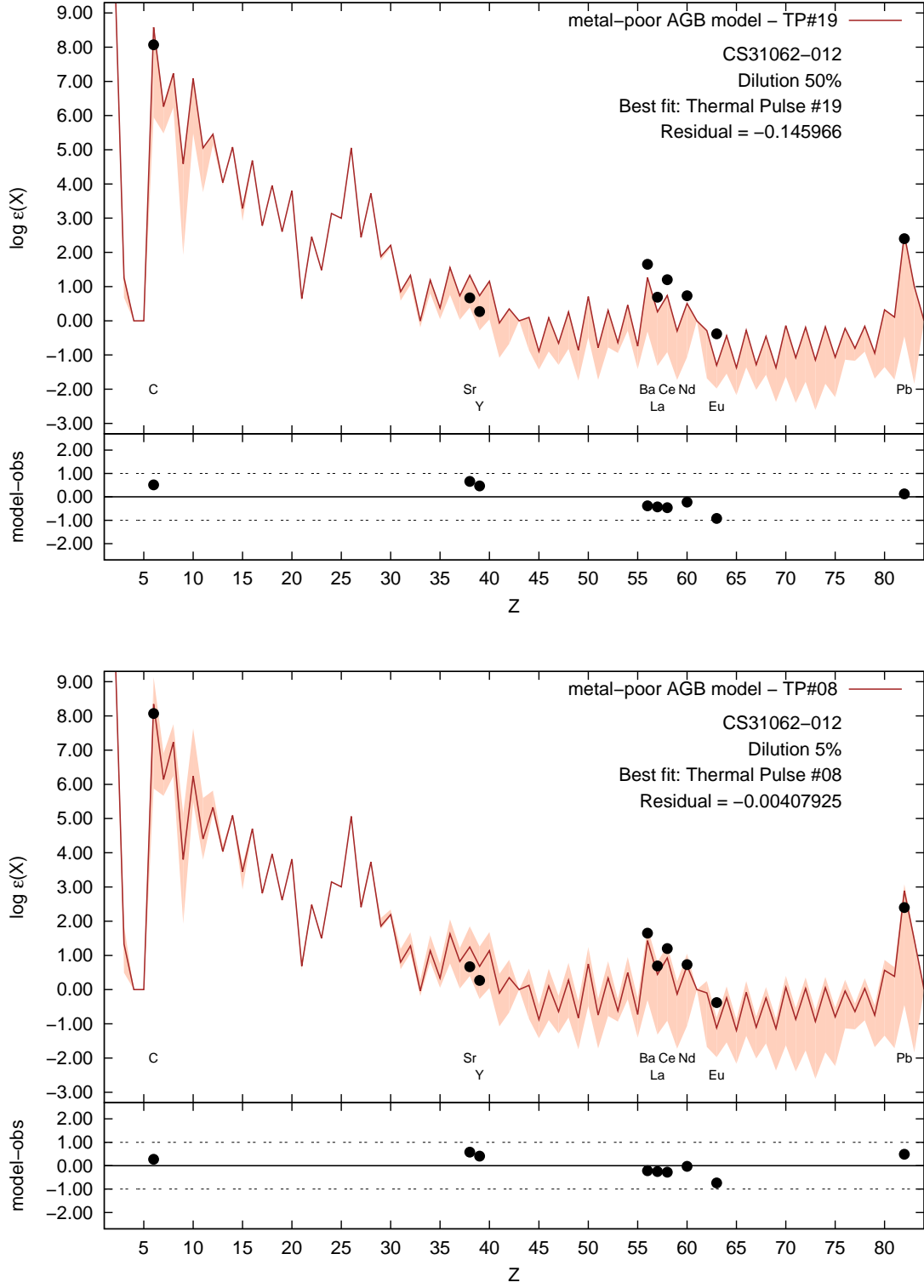


Fig. 21.— Best Fit Model Abundance Comparison of CS 31062–012, 50 Percent Dilution (upper panel), and 5 Percent Dilution (lower panel).

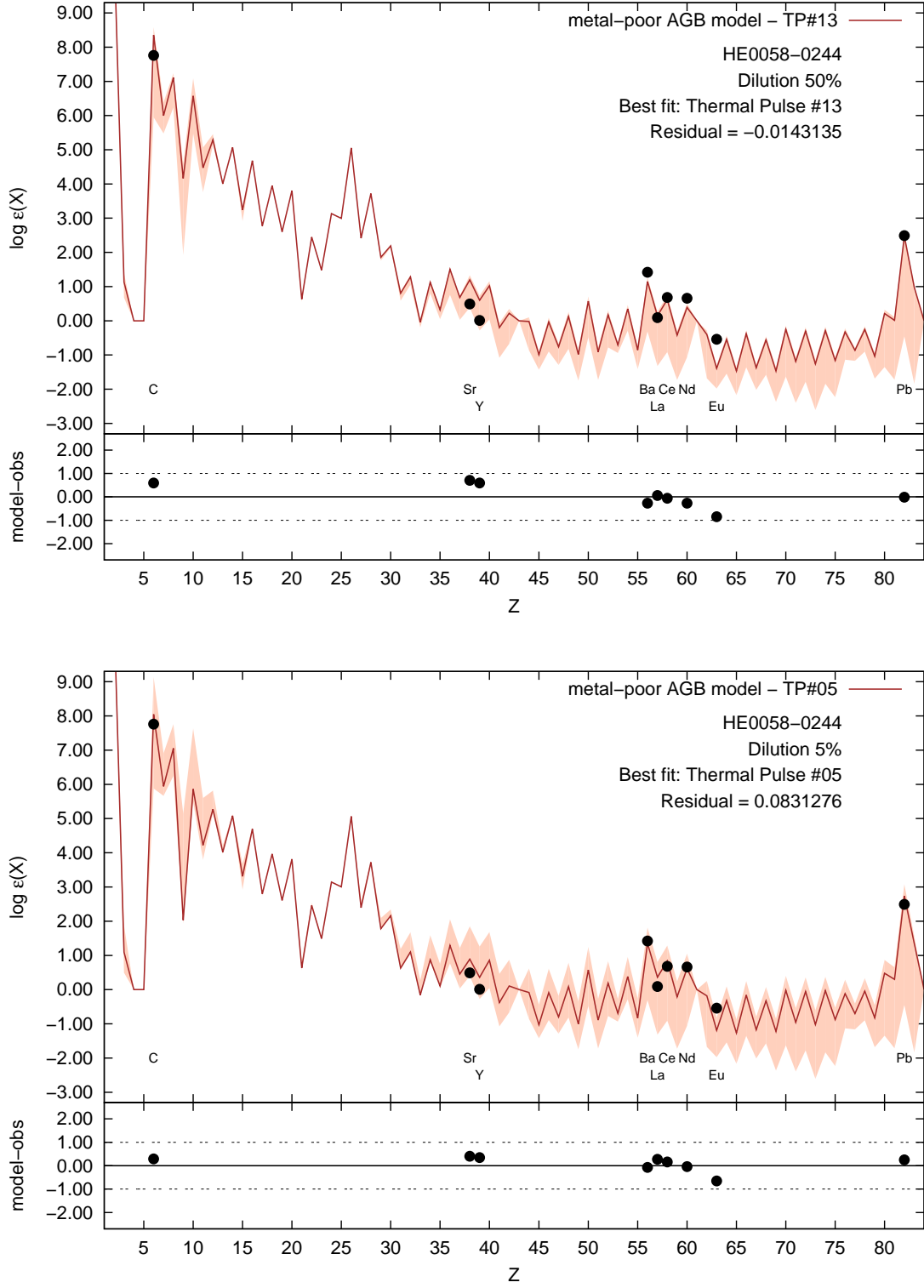


Fig. 22.— Best Fit Model Abundance Comparison of HE 0058-0244, 50 Percent Dilution (upper panel), and 5 Percent Dilution (lower panel).

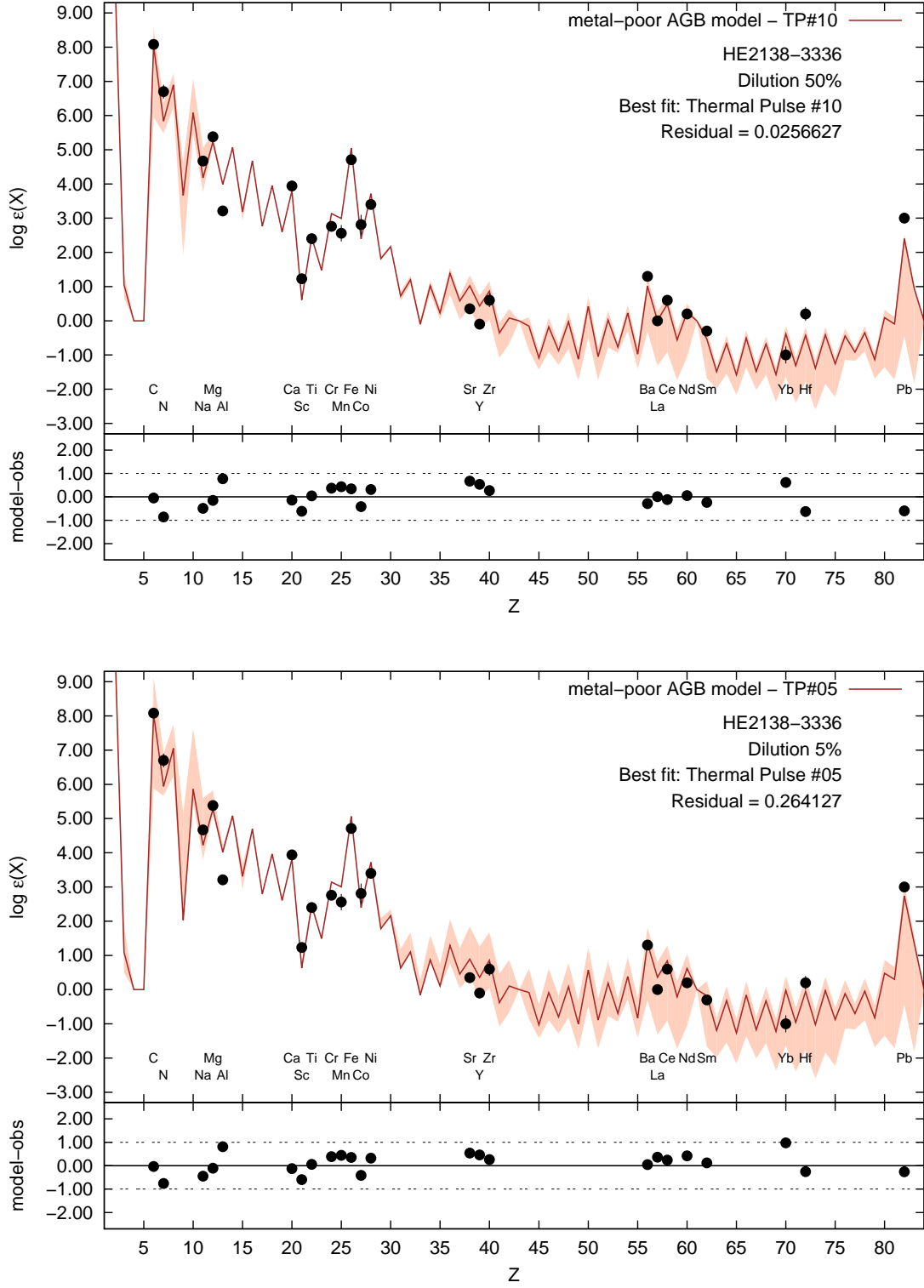


Fig. 23.— Best Fit Model Abundance Comparison of HE 2138–3336, 50 Percent Dilution (upper panel), and 5 Percent Dilution (lower panel).

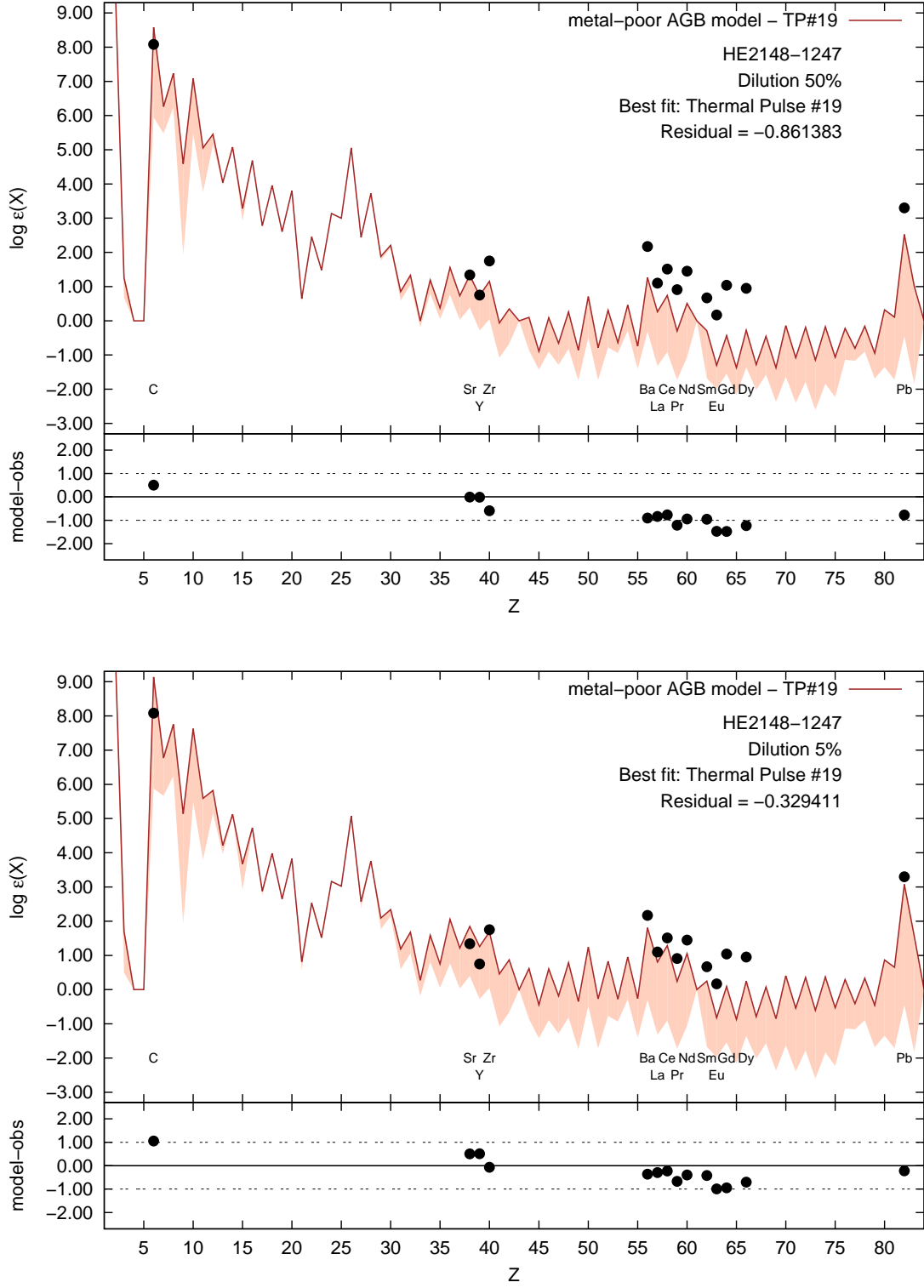


Fig. 24.— Best Fit Model Abundance Comparison of HE 2148–1247, 50 Percent Dilution (upper panel), and 5 Percent Dilution (lower panel).

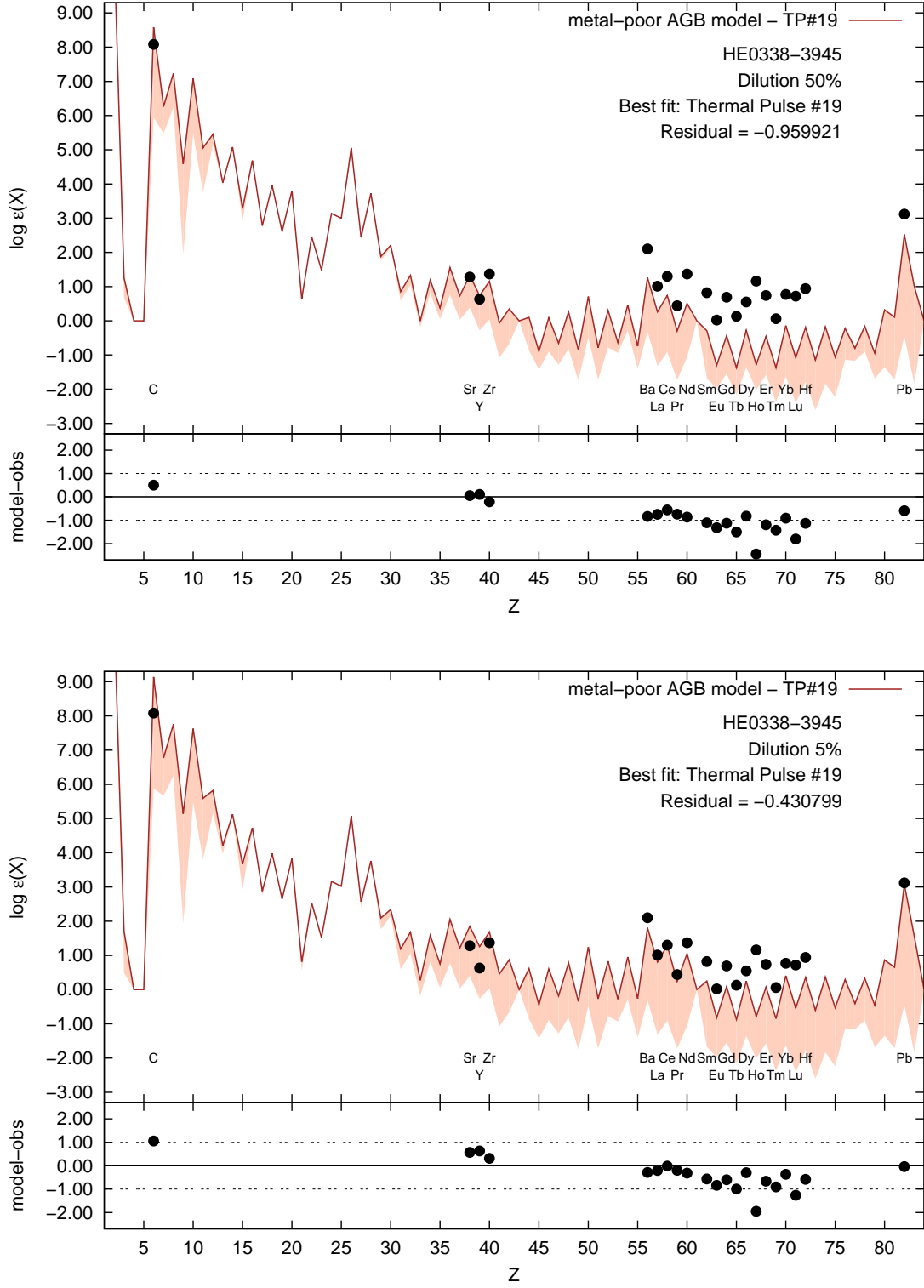


Fig. 25.— Best Fit Model Abundance Comparison of HE 0338–3945, 50 Percent Dilution (upper panel), and 5 Percent Dilution (lower panel).

C. Results of the comparison of Abundance Patterns of CEMP-sC Sample Stars with the best matched thermal pulse abundance distributions.

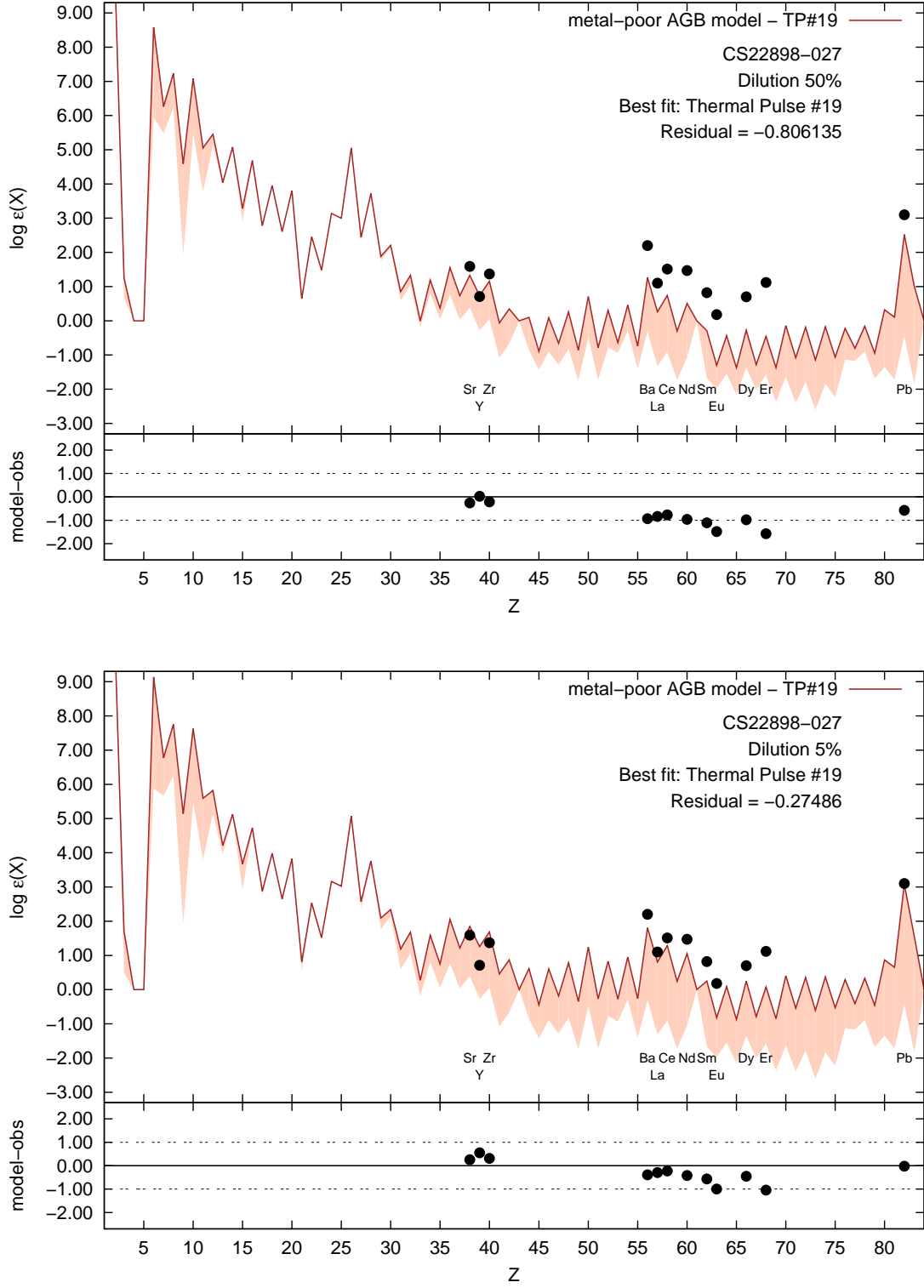


Fig. 26.— Best Fit Model Abundance Comparison of CS 22898-027, 50 Percent Dilution (upper panel), and 5 Percent Dilution (lower panel).

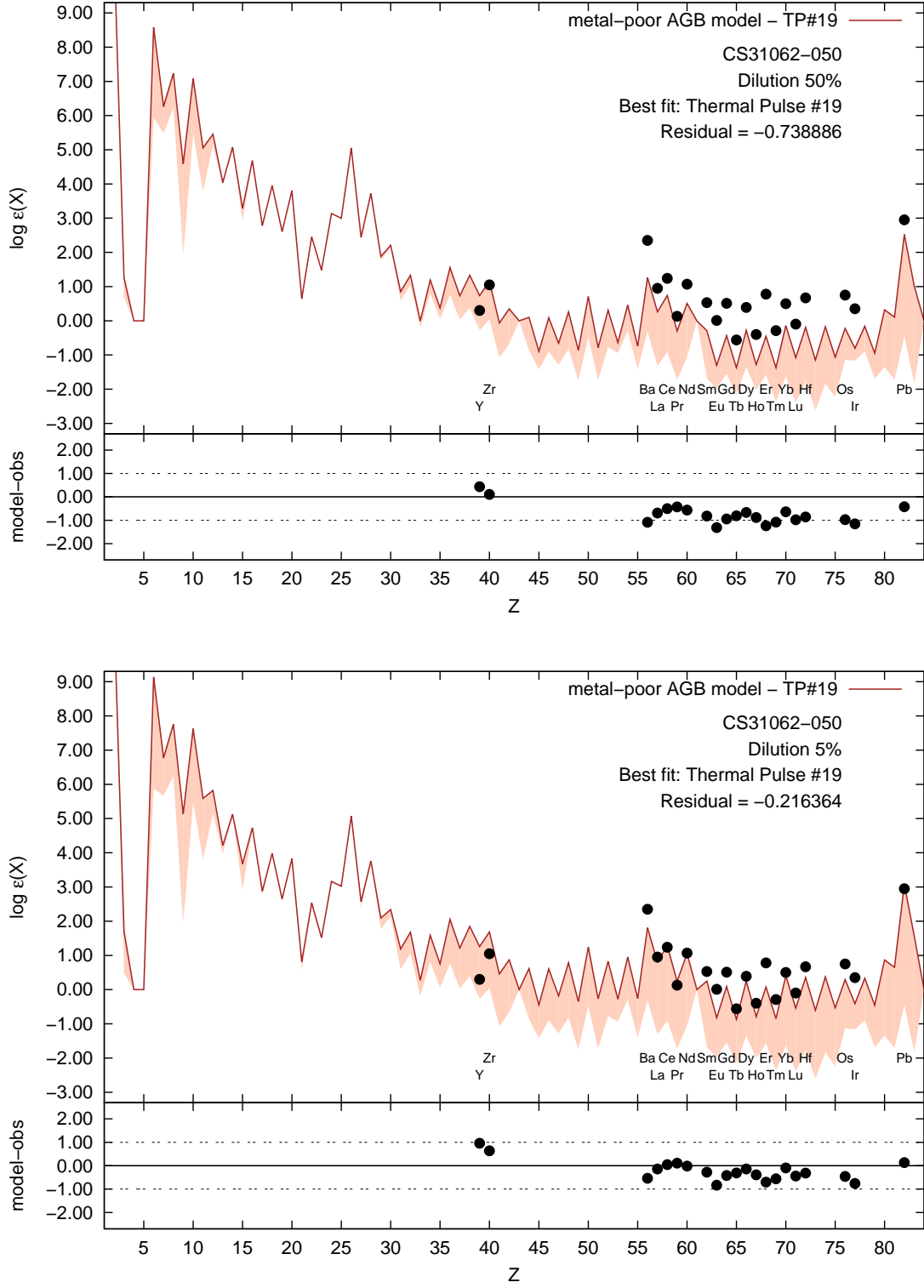


Fig. 27.— Best Fit Model Abundance Comparison of CS 31062–050, 50 Percent Dilution (upper panel), and 5 Percent Dilution (lower panel).

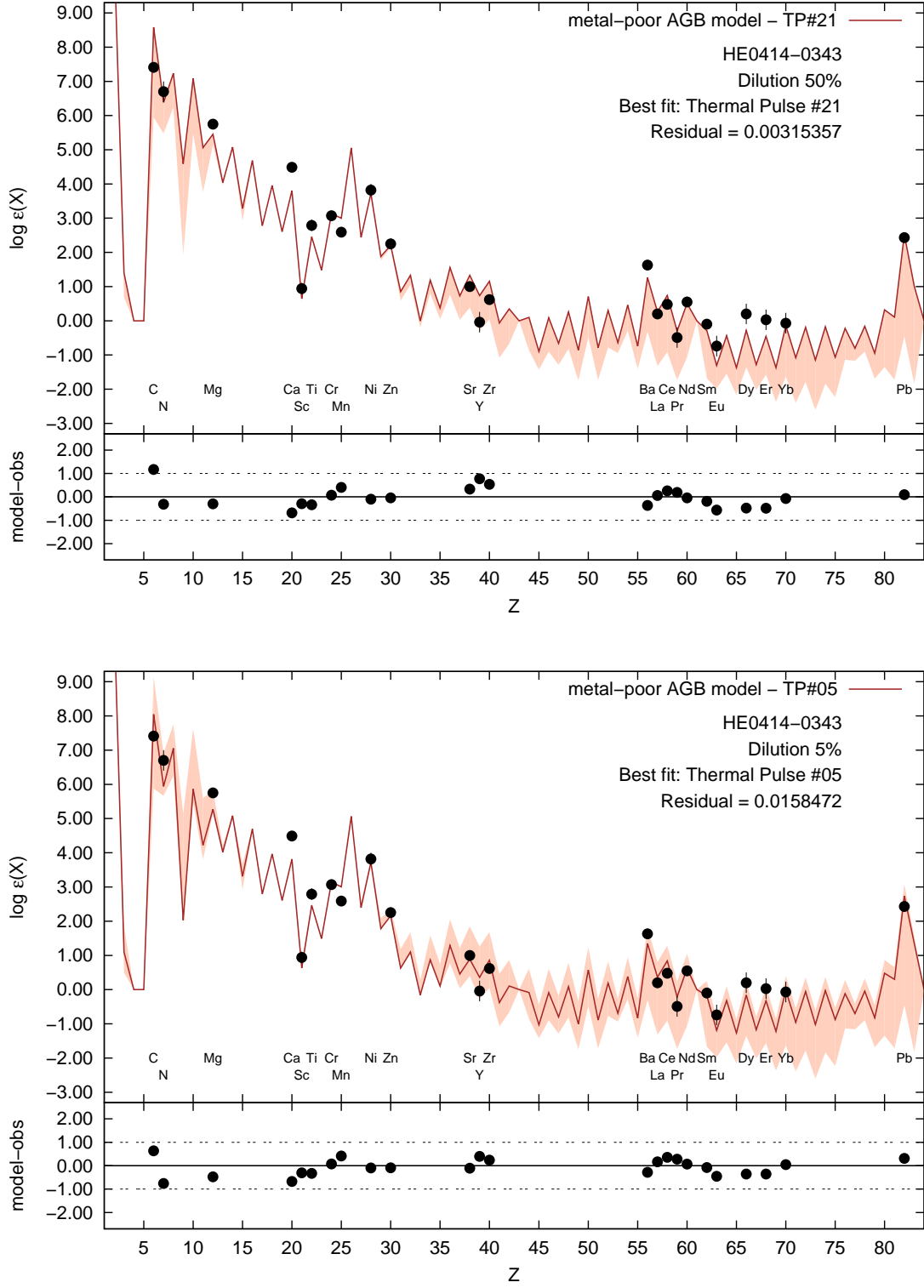


Fig. 28.— Best Fit Model Abundance Comparison of HE 0414–0343, 50 Percent Dilution (upper panel), and 5 Percent Dilution (lower panel).

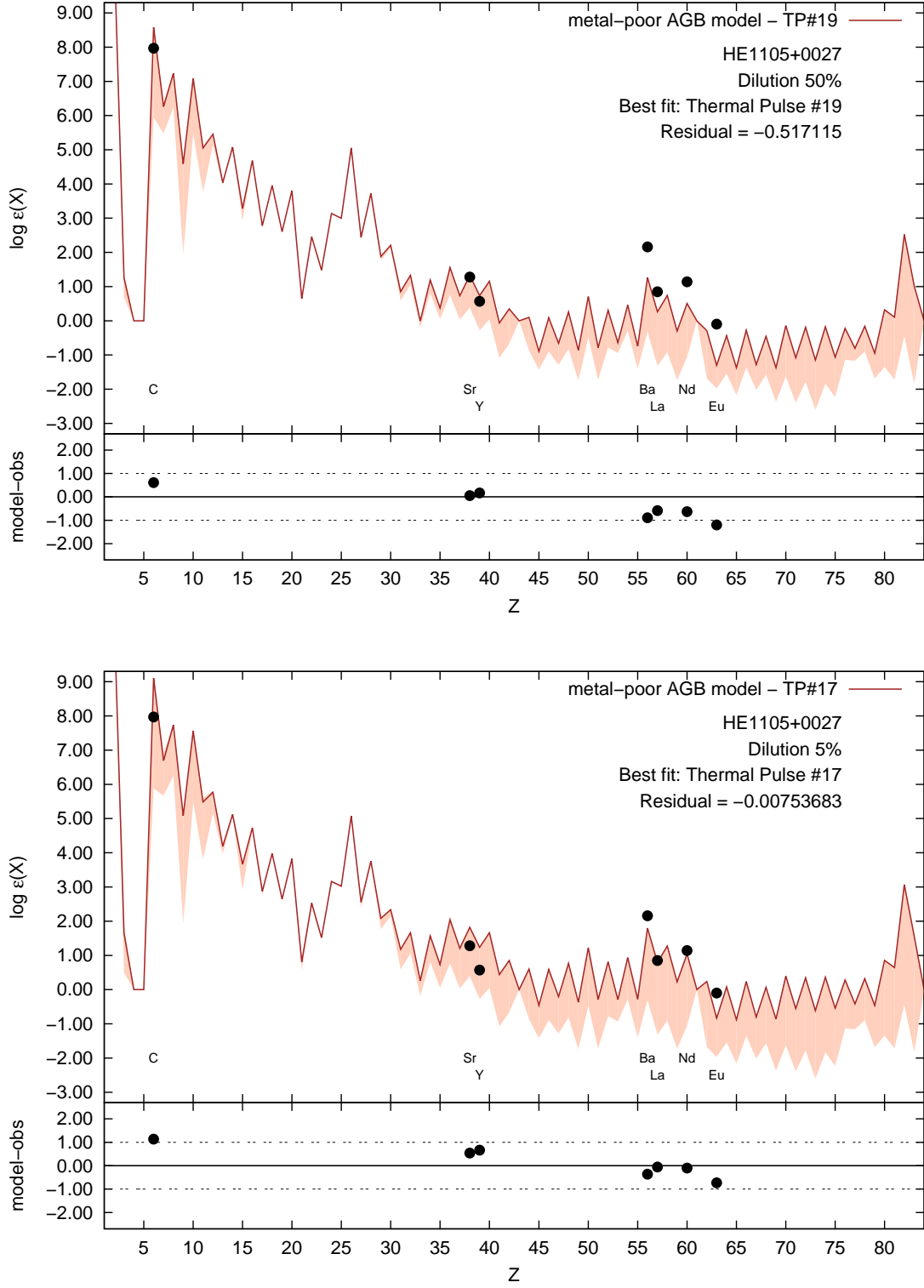


Fig. 29.— Best Fit Model Abundance Comparison of HE 1105+0027, 50 Percent Dilution (upper panel), and 5 Percent Dilution (lower panel).

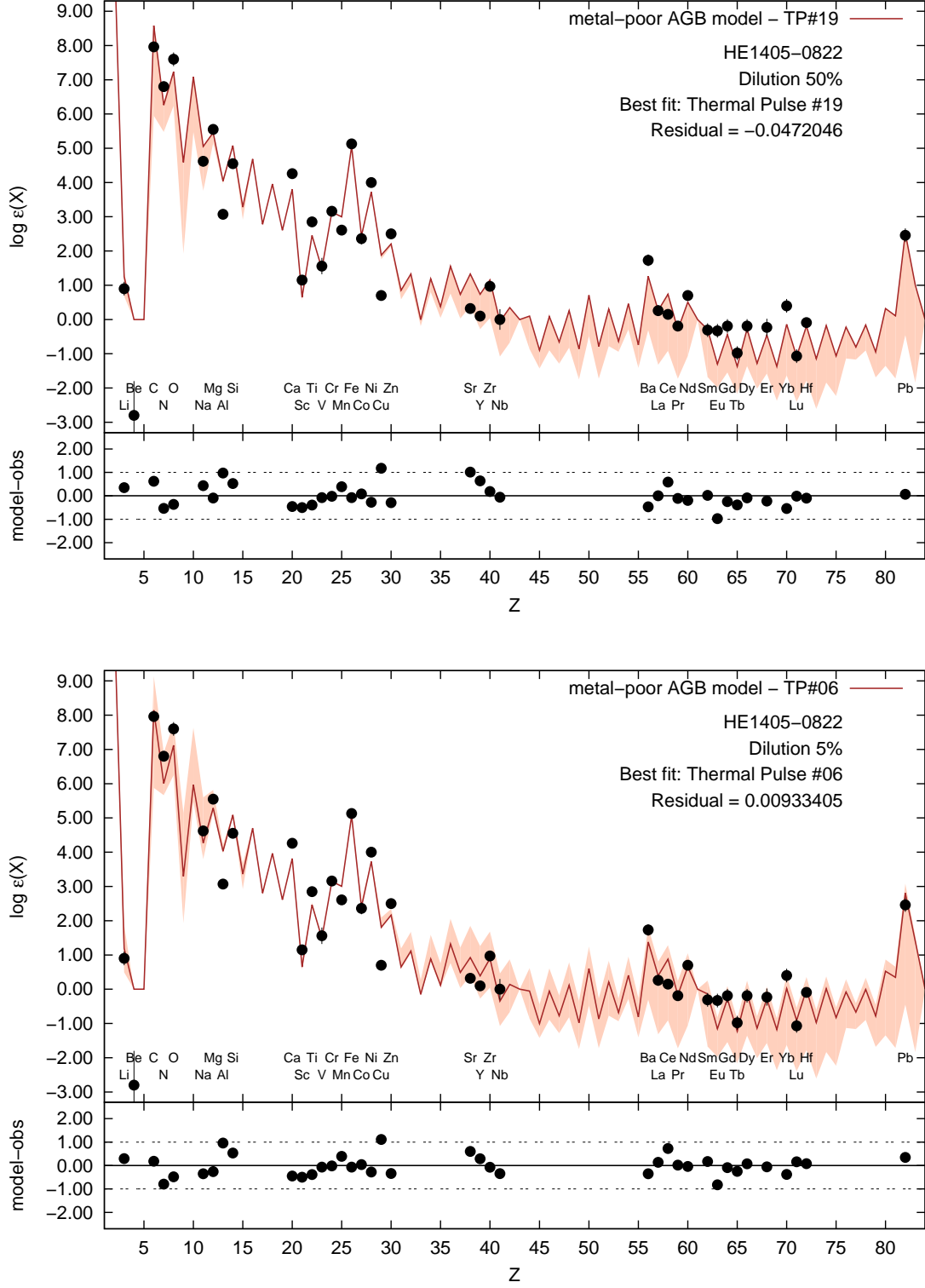


Fig. 30.— Best Fit Model Abundance Comparison of HE 1405–0822, 50 Percent Dilution (upper panel), and 5 Percent Dilution (lower panel).

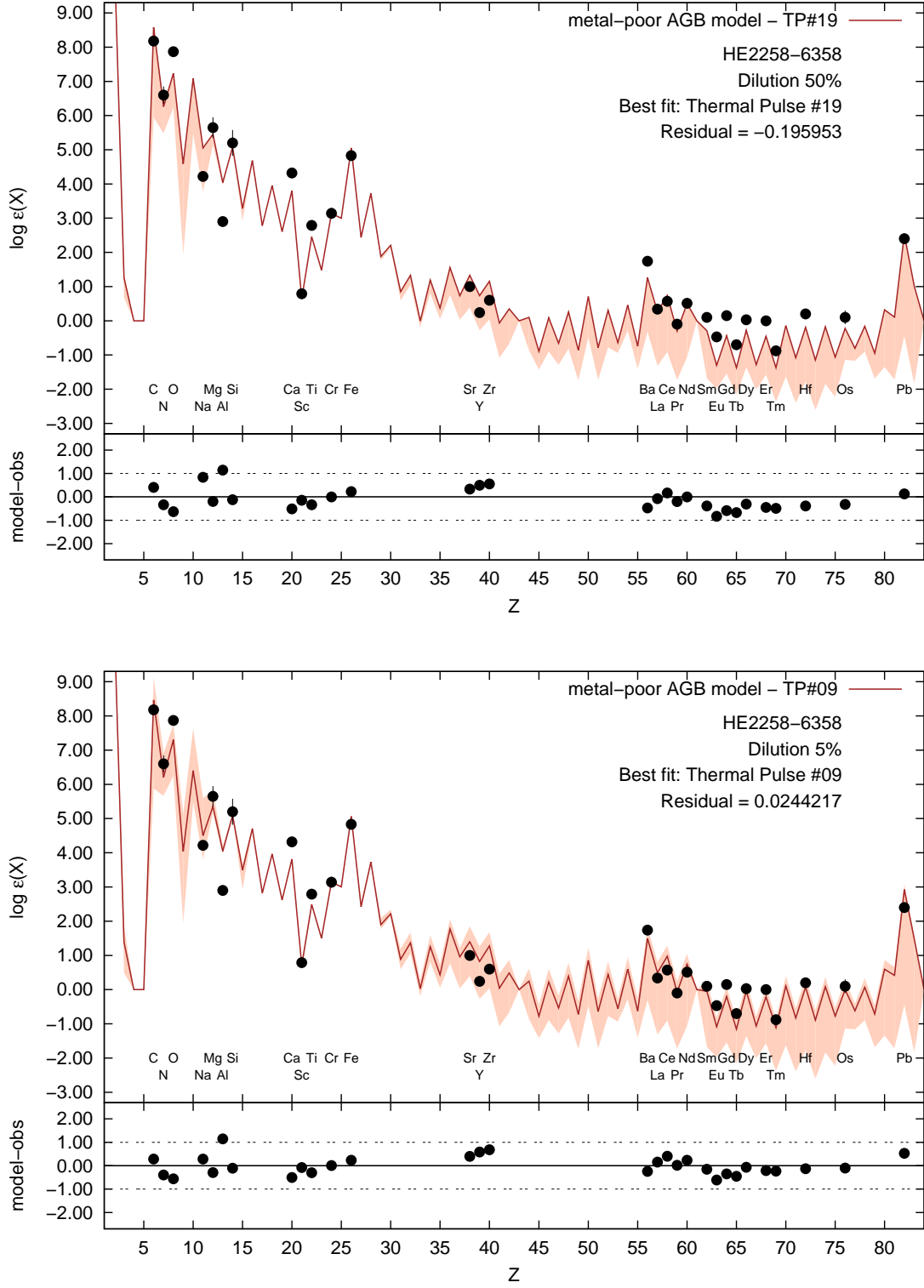


Fig. 31.— Best Fit Model Abundance Comparison of HE 2258–6358, 50 Percent Dilution (upper panel), and 5 Percent Dilution (lower panel).

